2020-01-01

Thermal Atomization Due to Boiling During Droplet Impingement on Superhydrophobic Surfaces

Preston Todd Emerson
Brigham Young University

Thermal Atomization Due to Boiling During Droplet Impingement on Superhydrophobic Surfaces

Preston Todd Emerson

A thesis submitted to the faculty of
Brigham Young University
in partial fulfillment of the requirements for the degree of

Master of Science

Julie Crockett, Chair
Daniel Maynes
Brian Iverson

Department of Mechanical Engineering

Brigham Young University

ABSTRACT

Thermal Atomization Due to Boiling During Droplet Impingement
on Superhydrophobic Surfaces

Preston Todd Emerson
Department of Mechanical Engineering, BYU
Master of Science

Superhydrophobic (SH) surfaces are characterized by their extraordinary water repellent qualities. When water comes in contact with these surfaces, it beads up and rolls around. This phenomenon is due partially to surface chemistry which promotes weak adhesive forces between liquid and solid. However, micro- and nanoscale surface roughness also plays a crucial role by trapping air beneath the liquid, reducing liquid-solid contact. Many advantages of these surfaces have been identified, including drag reduction and self-cleaning properties, and the body of research regarding them has grown rapidly over the past few decades.

This thesis is concerned with water droplets impinging superheated, superhydrophobic surfaces. In these scenarios, boiling is common in the droplet, producing vapor bubbles which burst through the droplet lamella and cause a spray of miniscule water particles known as thermal atomization. The work contained in this thesis uses an image processing technique to quantify trends in thermal atomization intensity during droplet impingement scenarios for a range of surface microstructure configurations, superheat temperatures, and Weber numbers.

In one study, droplet impingement on a smooth hydrophobic and three post-patterned SH surfaces of similar solid fraction is considered. In general, as pitch (center-to-center distance between posts) increases, atomization intensity decreases. This is attributed to the enhanced ability for vapor escape beneath the droplet that is present for wider pitch surfaces. Atomization intensity increases with increasing Weber number for each of the surfaces considered. Additionally, the Leidenfrost point is found to increase with increasing Weber number and decreasing pitch.

Next, thermal atomization on SH surfaces with two distinct microstructure configurations is considered: square posts (which allow vapor escape between structures) and square holes (which block vapor escape). Tests are done for each configuration with varying microstructure height, and structure spacing and solid fraction are held constant. Comparing the two configurations at each structure height and Weber number, the post-patterned surfaces suppress atomization for a large number of scenarios compared to the hole surfaces, supporting the theory that vapor escape through microstructures suppresses atomization. Microstructure height significantly affects trends in atomization intensity with surface temperature and Weber number. The LFP is seen to decrease with increasing height.

Keywords: superhydrophobic, droplets, impingement, boiling, atomization, heat transfer

ACKNOWLEDGMENTS

I would like to acknowledge, first and foremost, my graduate advisor, Dr. Julie Crockett. It was from Dr. Crockett that I first gained an interest in fluid dynamics, which led to my subsequent passion and pursuit of the subject in my graduate studies. She was also the one who gave me my first experience in research. Thank you, Dr. Crockett, for your support and your faith in me. I would also thank the other members of my graduate committee: Dr. Iverson, who has taught me almost everything I know on the topic of heat transfer, and Dr. Maynes, who has been integral in making my research robust. Thanks to my entire committee for the time and meticulous attention they have spent reviewing my papers.

I next acknowledge the many lab mates I've worked with in the fluids lab over the past few years. Matthew Searle, Kim Stevens, Adam Cowley, David Miller, and Chad Stucki were the wiser, more experienced graduate students when I began working in the lab. In addition, I've had the privilege of working along side Jacob, Jonathan, Chungfang, and many others along the way. Each has greatly impacted my learning and most have given invaluable advice regarding my research. I acknowledge Austin Fieldsted, who spent hours improving our experimental setup, running experiments, and processing data, and who deserves my sincerest gratitude for his contributions.

And finally, I express my deepest gratitude to God and my family. My wife, Miranda, not only tolerated many late nights and stressful weekends of work, but encouraged me every step of the way. I could not have accomplished this work without the encouragement and support of my wife, parents, siblings, and many other friends.

This work has been supported by the Utah NASA Space Grant Consortium and by the National Science Foundation grant number CBET-1707123.

TABLE OF CONTENTS

LIST OF TABLES

LIST OF FIGURES

NOMENCLATURE

A	Atomization intensity
A_{max}	Maximum atomization intensity found on the SmH surface for a Weber number of 85
A_c	Liquid-solid contact area
A_p	Pixel area
A^*	Normalized atomization intensity (exact definition is chapter specific)
$A^*_{max,t}$	Maximum normalized atomization intensity over the entire time span at a given surface temperature
$c_{p,s}$	Specific heat of a test surface
D_0	Initial droplet diameter
D_{max}	Maximum droplet spreading diameter
d	SH microstructure characteristic length (diameter or length)
f_s	Solid fraction
g	Acceleration due to gravity
h	SH microstructure height
h_{fg}	Latent heat of vaporization
k_s	Thermal conductivity of a test surface
L_c	Capillary length
N	Number of unit cells in a stretch of radius in a spreading droplet
n	Number of samples in a statistical group
ΔP	Pressure drop
Q	Volume flow rate of water vapor per height of microposts
q''	Heat flux
R_s	Spacial resolution
r	Roughness factor
S	Sample standard deviation
s	Spacing between SH microstructures
T_s	Surface temperature
T_{sat}	Saturation temperature
ΔT_e	Surface excess temperature
t	Time
Δt	Time step
$t_{\nu,95}$	Two-tailed Student's t-distribution for 95% confidence
u	Uncertainty
V_0	Droplet impact velocity
We	Weber number
w	SH microstructure pitch
$\overline{X}$	Sample mean

Greek letters

θ	Sessile contact angle
θ_a	Advancing contact angle
μ	Dynamic viscosity of water at room temperature
ν	Degrees of freedom
ρ	Density of water at room temperature

ρ_s	Density of a test surface
ρ_{vap}	Density of water vapor
σ	Surface tension of water at room temperature

CHAPTER 1. INTRODUCTION

Superhydrophobic (SH) surfaces are known for their phenomenal water-repelling ability, which leads to many unique properties including drag reduction and self-cleaning. For this purpose, they hold potential in a myriad of applications spanning from the automotive industry to energy systems and have been a focus of research for decades. Fluid dynamics and heat transfer on these surfaces in superheated environments are of particular interest since many applications involve high temperatures. This thesis is concerned with morphology and heat transfer dynamics of water droplets impinging SH surfaces heated above the saturation temperature of the liquid. Boiling is the driving mechanism behind the morphology and thermal regimes in these scenarios.

This chapter contains background information concerning SH surfaces, boiling, and droplet impingement dynamics, which is necessary in understanding the work contained in the following chapters. Previous research is reviewed and the objectives of the current work are established, along with a general overview of the thesis.

1.1 Background

1.1.1 Superhydrophobic Surfaces

Research pertaining to SH surfaces provides invaluable fundamental knowledge and experience to the fields of fluid dynamics and heat transfer. SH surfaces, while currently virtually non-existent in common man-made artifacts, are abundant in nature and have long been a human fascination. Scientists began describing the phenomenon of superhydrophobicity in the mid-twentieth century, and the unique properties associated with SH surfaces became known as the ”lotus effect,” named for the beautiful, aquatic, lotus flower.

It is observed that water, when deposited on a leaf of the lotus flower, pictured in Figure 1.1a, beads up and seems to glide effortlessly over the leaf’s edge. One advantage to this behavior

Figure 1.1: Images of the (a) Lotus flower, (b) Morpho butterfly, and (c) Alkali fly under water. The inset in (a) is an SEM image of the lotus leaf where the scale bar represents 10 μm. Note: image of the lotus flower obtained from pxhere.com, image of the morpho butterfly obtained from peakpx.com, images of alkali fly and lotus leaf microstructure obtained from Wikimedia.

is evident given the wet climate in which the lotus resides, namely that it impedes the buildup of water on top of the leaf. Upon closer inspection, it is found that the superhydrophobicity of the plant also facilitates self-cleaning. Smaller water droplets that appear to glide are in reality rolling, and particulates on a leaf's surface are collected and carried away with the droplets. This self-cleaning property alone has sparked extensive research into SH surfaces [4].

Superhydrophobicity as an evolutionary trait is found not only in plants like the lotus, but is also ubiquitous in the animal kingdom. The brilliantly blue morpho butterfly (Figure 1.1b) instantly repels otherwise deadly rainfall as it flutters through the Amazon. The alkali fly of Mono Lake, California uses its superhydrophobic power to scurry atop the water's surface and then dive beneath for food while perfectly retaining an air pocket around it to breath (seen in Figure 1.1c). Mark Twain encountered these curious creatures and said of them, "You can hold them under water as long as you please—they do not mind it—they are only proud of it. When you let them go, they pop up to the surface as dry as a patent office report, and walk off... unconcernedly" [5].

What gives these, and numerous other plants and animals, their superhydrophobic powers? Superhydrophobicity depends on the combination of two separate phenomena. The first is hydrophobic surface chemistry, which has to do with surface energy between solid, liquid, and gas. Surface energy is caused by cohesive and adhesive molecular forces. Consider a droplet sitting on a smooth hydrophobic (SmH) surface such as the one represented in Figure 1.2a. Where the solid, liquid, and gas are all in contact is called the triple contact line, and the contact angle, θ, is determined by a balance of forces caused by the liquid-solid surface energy, the solid-gas surface energy, and the liquid-gas surface energy. The liquid-gas surface energy is a commonly used property in fluid dynamics known as surface tension, σ. It is measured to be about $\sigma = 0.0728$ N/m for water in air. Wettability of a surface (degree to which it is hydrophilic or hydrophobic) is defined by the contact angle, where a high contact angle indicates hydrophobic, and a low contact angle indicates hydrophilic.

Contact angles measured for static droplets, as shown in Figure 1.2, are known as sessile contact angles. Dynamic contact angles can be measured for scenarios where liquid is impacting on the surface: the advancing angle, measured as a droplet impacts, and the receding angle, which is measured as it rebounds. The difference between these two dynamic angles is known as contact angle hysteresis; SmH and SH surfaces are characterized by very low hysteresis. Hydrophobic surfaces are classified as those with sessile contact angles above 90 $^\circ$, while surfaces with contact angles above 150 $^\circ$ are considered superhydrophobic. Hydrophilic surfaces have contact angles below 90 $^\circ$, and when the contact angle approaches zero, the surface is considered superhydrophilic. Unsurprisingly, most oils and other greasy substances are classified as hydrophobic, hence the popular saying that water and oil do not mix. Polytetrafluoroethylene, commonly known as Teflon, is another hydrophobe used in a myriad of everyday applications such as waterproofing sprays and non-stick cookware.

Note that gravitational forces may also play a role in determining the shape of a droplet sitting on a solid surface. By considering a balance between surface tension and gravitational forces, a parameter called the capillary length is defined as $L_c = \sqrt{\frac{\sigma}{\rho g}}$, where ρ is density of the liquid and g is acceleration due to gravity. For water in air, the capillary length is calculated to be $L_c = 2.71$ mm. For water droplets of diameter less than the capillary length, gravitational forces can be neglected. Droplets used to measure contact angles on a surface should meet this criterion.

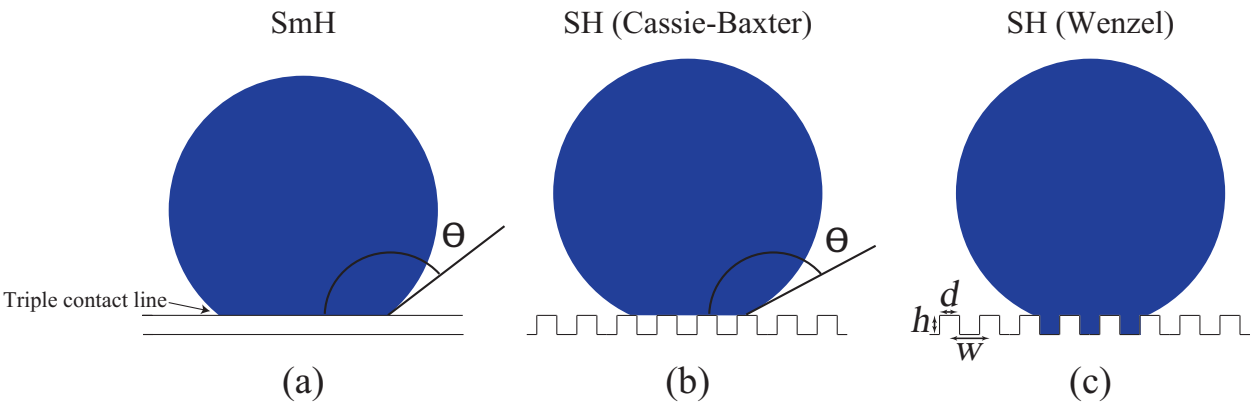

Figure 1.2: Water droplet sitting atop (a) a SmH surface, (b) a SH surface in the Cassie-Baxter state and (c) a SH surface in the Wenzel state. The triple contact line, sessile contact angle, θ, and surface microstructure dimensions are also depicted, where h is structure height, d is structure width, and w is structure pitch.

A second prerequisite for superhydrophobicity is surface roughness on the micro- or nanoscale. When water encounters a hydrophobic surface covered in microscopic bumps, air can be trapped beneath the droplet, creating a sort of composite solid-gas surface (seen in Figure 1.2b and 1.2c). A droplet sitting atop the surface in this way without wetting (or penetrating) the air cavities is said to be in the Cassie-Baxter state, as shown in Figure 1.2b. This state reduces the liquid-solid contact area, thus reducing the overall attraction, leading to a higher contact angle than is otherwise possible. Air cavities also allow a semi-slip condition for water moving against the surface, which reduces drag and contributes to the gliding-type motion of water commonly seen on SH surfaces. Figure 1.2c shows another possible configuration, called the Wenzel state, where the liquid wets the cavities. This state can be caused by many different factors including high pressure at the stagnation point caused by large droplet impact velocity, cooling of the surface, and deteriorating hydrophobic surface chemistry. In the Wenzel state, previously described advantages are lost.

Each of the living organisms discussed above exhibits a waxy, hydrophobic exterior with micro- or nanoscale texture, causing their superhydrophobicity. For example, the alkali fly has minuscule hairs all over its body, and the surfaces of lotus leaf and the morpho butterfly are simply naturally bumpy (this is demonstrated in Figure 1.1a for the lotus leaf). Synthetic superhydrophobic surfaces used for research are fabricated in many different ways, and the process used for the present research is outlined in Chapter 2. In the present work, the microscopic texture is made up of deliberate microstructures (such as posts or ribs). Important microstructure parameters will

be studied in this work such as microstructure height, h, characteristic length, d, and pitch, w, or center-to-center spacing of the structures; these are defined in Figure 1.2c. Microstructure shape is also important and will be explored as well. The solid fraction, f_s, is the total area on top of the structures divided by the total projected area of the surface. For liquid in the Cassie-Baxter state, contact angle has been shown to increase with decreasing solid fraction according to the relationship: $\cos\theta = -1 + f_s(1+\cos\theta_{Sm})$ [6], where θ_{Sm} is the contact angle on a smooth surface of the same material.

1.1.2 Boiling

Boiling is the process by which a liquid is vaporized at a solid surface. Vapor bubbles form at the liquid-solid interface when the temperature climbs above the saturation temperature of the liquid for the given pressure. Boiling water is ubiquitous, not only in everyday life, but in industrial applications including energy production, steel quenching, and both macro- and micro-scale heat exchangers.

Boiling is a particularly effective method of heat transfer because it involves phase change, specifically vaporization. Phase change is an isothermal (constant temperature) process which takes more energy than simply raising or lowering the temperature of a material. The energy involved in converting a liquid to gas is called the latent heat of vaporization, and is typically measured in units of energy per mass. Figure 1.3 shows the classical pool boiling curve, a relationship between heat flux to the liquid, q", and excess temperature, ΔT_e, (temperature of the solid minus the saturation temperature of the liquid). This curve demonstrates the boiling regimes which are well established in pool boiling scenarios [7, 8] and will be discussed here.

Natural convection, the first regime, occurs at low excess temperatures. A flow develops in the liquid, due to the density gradient caused by ΔT_e, which facilitates convection heat transfer. As the excess temperature increases, vapor bubbles begin to form at nucleation sites on the solid surface. These sites usually correspond to defects in the surface, anywhere that air can be trapped such as scratches or dents. This bubbly regime is called nucleate boiling. The rate of heat transfer in this regime increases rapidly due to the latent heat added to the system through phase change and the increase in convection heat transfer caused by fast-rising vapor bubbles. As excess temperature increases, the bubbles grow in size and more and more nucleation sites develop. When bubbles

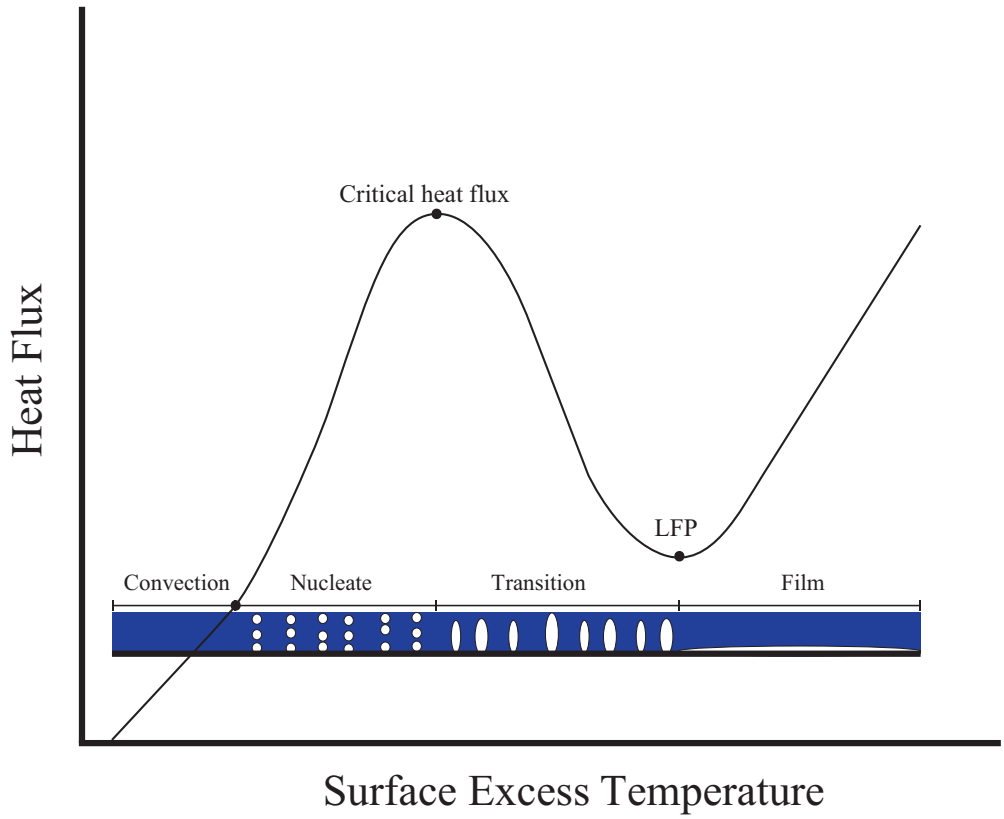

Figure 1.3: Classical pool boiling regimes: convection, nucleate, transition, and film. Surface excess temperature is the temperature of the surface minus the saturation temperature of the liquid. The onset of film boiling is termed the Leidenfrost point, or LFP.

grow so large that they begin to coalesce with one another, transition boiling is in effect. Heat flux begins to decrease because large bubbles at the solid surface insulate the liquid from the surface. Finally, as the vapor bubbles merge at the solid surface creating a stable vapor film between the liquid and solid, film boiling is reached. The onset temperature of film boiling is labeled the Leidenfrost point (LFP) and marks a minimum heat flux due to the insulating vapor layer. As excess temperature increases beyond this point, heat flux begins to rise once more.

Boiling regimes and boiling principles are fundamental to the work outlined in this thesis. They will be discussed further in the context of droplet impingement boiling and superhydrophobic surfaces.

1.1.3 Droplet Impingement

Research involving single droplet impingement is almost always performed with a broader goal in mind, namely, to begin to understand the vastly more complicated dynamics of impacting liquid sprays, which involves interactions between many impinging droplets. Liquid sprays are common in industrial applications including inkjet printing, spray coating, spray cooling of materials, and fuel injection systems, and while single droplet impact does not fully capture the nuanced dynamics present in these scenarios, it remains an important step towards that goal.

Figure 1.4 displays the temporal progression of droplets impinging smooth hydrophilic, SmH, and post-patterned SH surfaces for no heat and heat transfer scenarios. The micropost array of the SH surface has structure height of 4 μm, pitch of 12 μm, and solid fraction of nominally 0.1. Note that the temporal range considered differs for the two scenarios. It is seen from this figure that when a droplet impacts a solid surface, it begins to spread. The lamella grows thinner and a rim develops at the periphery. The morphology of the impinging droplet is affected by many factors, including properties of the test surface and properties of the droplet. Weber number, defined as $We = \rho V_0^2 D_0/\sigma$, is a nondimensional parameter commonly used in these scenarios to describe the balance between inertial forces (i.e. droplet impact) and surface tension. Here, V_0 and D_0 are droplet impact velocity and initial diameter. Note that for the work in this thesis, droplet density and surface tension used to calculate Weber number are taken at room temperature. Thus, in high heat transfer scenarios, *We* represents the initial Weber number, not the value associated with the heated droplet. Weber number, surface temperature, and wettability all prove to be important parameters affecting the present research. When considering SH surfaces, the microstructure configuration (shape, height, pitch, and solid fraction) also plays an important role. Given the various influencing factors, many different morphological results are possible, and these have been studied and documented by researchers for decades [3, 9–16]. A summary of these results for droplet impingement on both hydrophilic and hydrophobic surfaces is included below.

1.1.3.1 Hydrophilic Morphology

On hydrophilic surfaces at temperatures below the liquid saturation point, impinging droplets will spread and come to rest on the surface (as seen in Figure 1.4a), a behavior called deposition. As

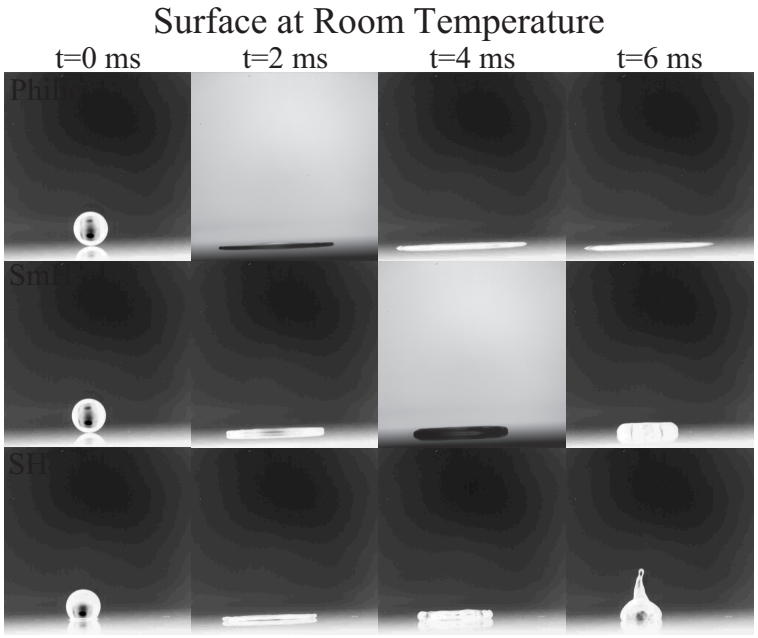

(a)

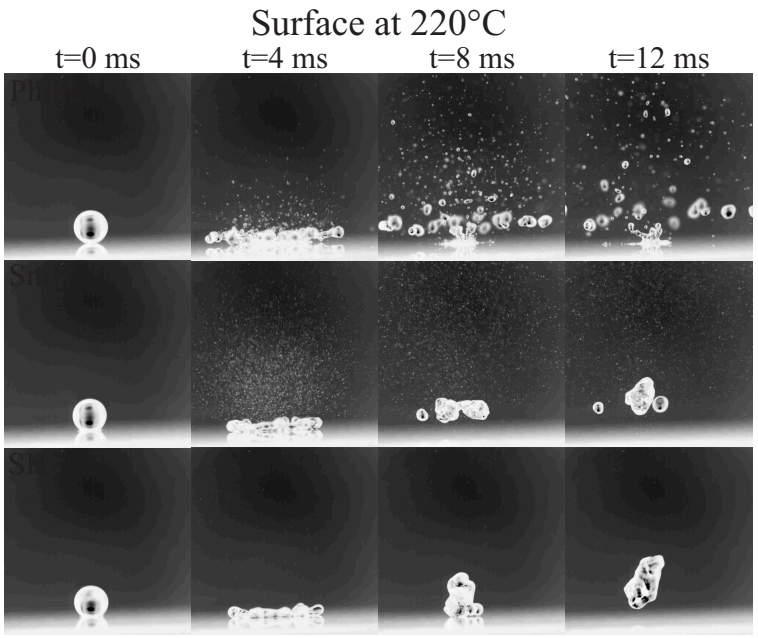

(b)

Figure 1.4: Temporal progression of droplets impinging a smooth hydrophilic (Philic), SmH, and post-patterned SH surface at $We = 85$ and for (a) a room temperature surface and (b) a surface at 220 °C. The micropost array of the SH surface has structure height of 4 μm, pitch of 12 μm, and solid fraction of nominally 0.1. Note that time after impact ranges from 0 to 6 ms for the room temperature scenario and from 0 to 12 ms for the superheated scenario to account for the change in dynamics due to heat transfer.

Weber number increases, the maximum spread diameter, D_{max}, increases, and the lamella thickness decreases. The droplet may experience splashing (also known as droplet breakup) for high initial Weber numbers and/or high surface temperatures. Droplet breakup is characterized by secondary droplets ejecting from the periphery of the primary droplet, and it occurs when inertial forces overcome surface tension. Increasing initial Weber number leads to increased inertial forces, while increasing surface temperature leads to decreased surface tension. In Figure 1.4, breakup is not seen on any of the surfaces in the room temperature scenario, but can be seen on the hydrophilic and SmH surfaces in the heated scenario. Note that as surface temperature increases in the subcooled region, no significant change to droplet morphology occurs [16], and the presence of the deposition and breakup states are affected only by Weber number. Droplet morphology and splashing can take different forms depending on liquid properties, Weber number, and surface wettability, as explained by Rioboo et. al. [11].

For surface temperatures above the liquid saturation point (as seen in Figure 1.4b), droplet boiling occurs [1,3,13–15,17–20], and morphology is significantly affected by the boiling regime. During nucleate boiling, vapor bubbles formed in the droplet may burst upwards through the lamella of the spreading droplet, causing a spray of tiny secondary droplets called thermal atomization. Thermal atomization occurs simultaneously with the deposition and breakup states. The intensity of thermal atomization in a given scenario is a function of surface temperature and follows a similar pattern as heat flux in the pool boiling curve shown in Figure 1.3 [20]: as surface temperature rises during nucleate boiling and a greater number of vapor bubbles are formed, atomization intensity increases. In the transition regime, when bubbles begin to coalesce, atomization intensity begins to decrease due to the insulating effect of the bubbles at the liquid-solid interface. When the LFP is reached, atomization is suppressed due to the stable vapor film, which insulates the droplet and allows vapor to flow laterally beneath the droplet. Figure 1.5 illustrates this trend for the same surfaces as in Figure 1.4. Note that the LFP is not reached for the hydrophilic surface due to limitations in the heater, but droplets impinging the SmH and SH surfaces at 330 °C are clearly in film boiling. In droplet impingement scenarios, the LFP is often defined as the lowest temperature for which thermal atomization is no longer observed. It should be noted that atomization intensity is also a function of Weber number, as increasing relative inertial increases

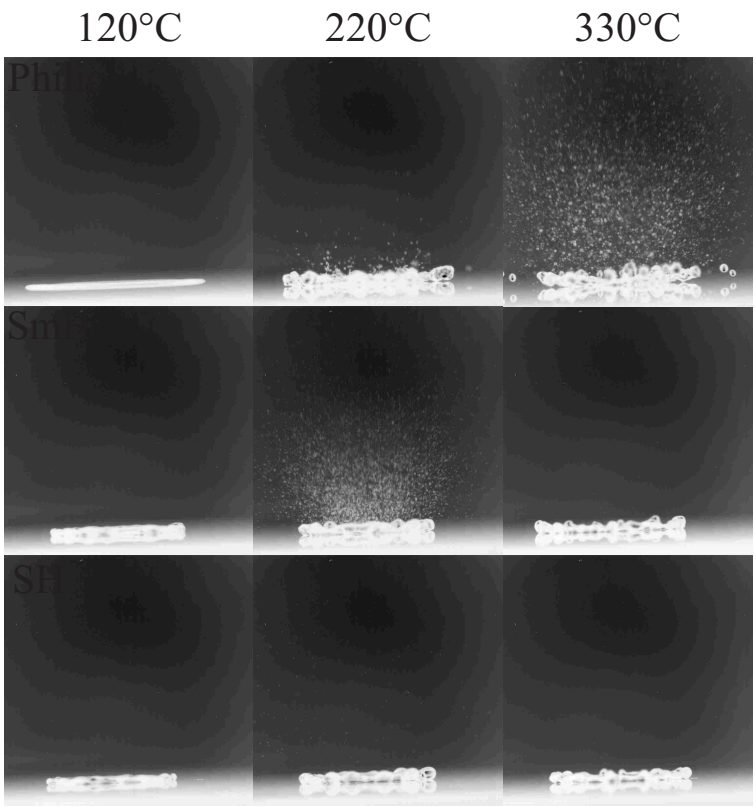

Figure 1.5: Droplets impinging smooth hydrophilic, SmH, and post-patterned SH surfaces at $We = 85$, $t = 3$ ms, and surface temperatures of 120 °C, 220 °C, and 330 °C. The micropost array of the SH surface has structure height of 4 μm, pitch of 12 μm, and solid fraction of nominally 0.1.

spreading, which in turn decreases droplet lamella thickness and the resistance to vapor bubbles bursting through.

Abundant research has been performed for droplets impinging hydrophilic surfaces in the film boiling regime [18, 21–25]. Where deposition would otherwise be present, these droplets, often called Leidenfrost droplets, retract and rebound off the surface. This bouncing effect is due to the vapor film upon which the droplet sits during the entire duration of impact. As in the other scenarios discussed, Leidenfrost droplets are subject to breakup at high Weber numbers.

1.1.3.2 Hydrophobic Morphology

Deposition never occurs on SmH and SH surfaces. Instead, the these surfaces' aversion to water causes droplets to retract and rebound, as shown in Figure 1.4a. Often, rebounding droplets

separate, and a satellite droplet is seen hovering above the primary. As with hydrophilic surfaces, D_{max} increases with Weber number in these scenarios, and droplet breakup at the periphery occurs for high Weber numbers and surface temperatures. For temperatures above the saturation point, thermal atomization is generated during droplet spreading, as seen in Figures 1.4b and 1.5. Rebound or breakup is also observed at these temperatures. As the droplet retracts and lamella thickness increases, atomization generation in the droplet ceases. During film boiling, atomization is suppressed.

Note from Figures 1.4b and 1.5 that the SH surface exhibits a significantly lower intensity of atomization than the SmH. Microstructure configuration is seen to play a significant role in atomization intensity. The range of temperatures that constitute each boiling regime is also greatly dependent on microstructure configuration, and these distinctions make up the bulk of the research in this thesis.

1.1.4 Relevant Work

In this section, droplet impingement results are presented from previous studies that relate to the work in this thesis. A wide range of surface wettability is considered and the vast majority of results involve heat transfer scenarios. Five categories of results will be discussed: droplet morphology, droplet dynamics, wetting/dewetting, thermal atomization, and the LFP.

1.1.4.1 Droplet Morphology and Regime Maps

For impingement scenarios where boiling is present, droplet morphology is strongly influenced by both Weber number and surface temperature. Morphological results can be divided into two main categories: primary droplet morphology (deposition, rebound, and breakup) and secondary droplet morphology (the presence of thermal atomization). In a 2015 study, Bertola [1] examined droplet impact behavior on a smooth aluminum (hydrophilic) surface for temperatures ranging from 50 °C to 400 °C and Weber numbers from 5 to 160. The deposition, rebound, and breakup states (with and without thermal atomization) were mapped with surface temperature and Weber number. Figure 1.6a shows their results. It was found that at a given surface temperature, increasing Weber number increases the likelihood of thermal atomization. Droplet breakup

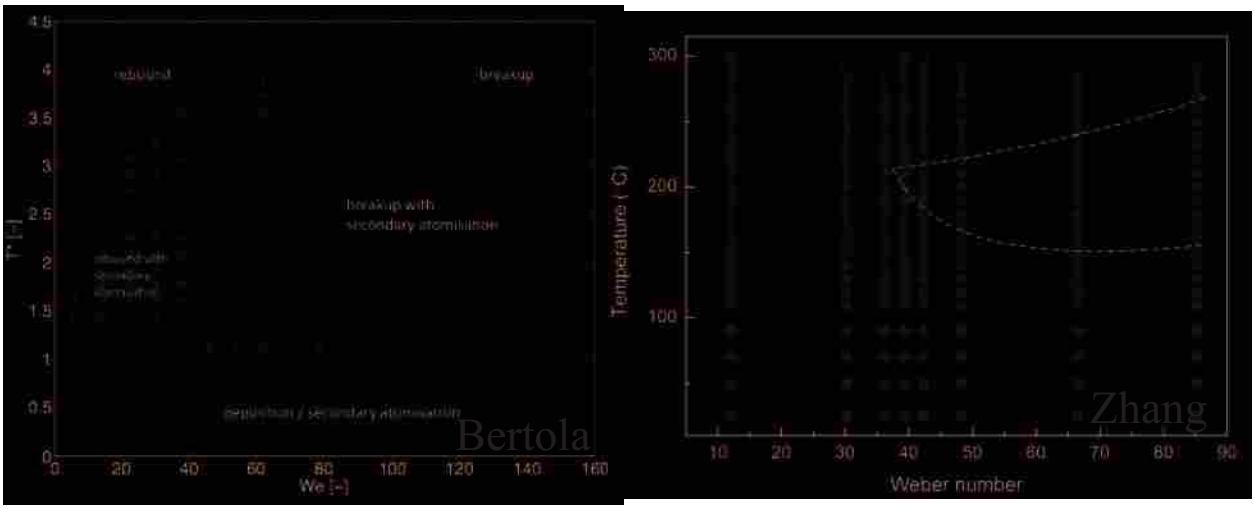

(a) (b)

Figure 1.6: Droplet morphology regime maps presented by (a) Bertola [1] and (b) Zhang et al. [2]. In Bertola's work, temperature was normalized as: $T^* = \frac{\Delta T_e}{T_L - T_{sat}}$, where T_L is the Leidenfrost temperature and T_{sat} is the saturation temperature of water; the regimes are marked on the the map. In Zhang's work, the markers are as follows. Red circles: Deposition with no atomization, pink squares: deposition with atomization, green triangles: transition with atomization, purple stars: splashing (may include atomization), blue diamonds: rebound with no atomization, dark blue pentagons: rebounding with satellite droplet and no atomization.

was also found to occur at high Weber numbers. For a given Weber number, as surface temperature increases in the nucleate and transition boiling regimes, thermal atomization becomes more prevalent. In the film boiling regime, atomization is suppressed and droplet rebound (or breakup) occurs. However, it has been found that at surface temperatures significantly greater than the LFP, atomization can occur in the film boiling regime [26]. Additionally, increasing surface temperature leads to more likely droplet breakup.

Zhang et al. created a similar droplet impact regime map for surfaces of varying wettability [2] which is shown in Figure 1.6b. Silicon substrates with and without a graphene coating were used. Surfaces were etched with circular microposts of 5 μm diameter and pitches of 10 μm and 20 μm. This produced hydrophilic surfaces with contact angles of 60 $^\circ$ and 70 $^\circ$ and hydrophobic surfaces with contact angles of 115 $^\circ$ and 130 $^\circ$. Surface temperatures from 25 °C to 300 °C and Weber numbers from 15 to 85 were considered. Results were similar to Bertola's finding in that droplet breakup occurs at high Weber numbers and temperatures for these surfaces,

and atomization was present during nucleate boiling. It was found that the hydrophobic surfaces largely suppress the deposition state in favor of rebound compared to the hydrophilic surfaces. For the surfaces with wider structure pitch (both hydrophilic and hydrophobic), droplet breakup was almost entirely eliminated.

Concerning the presence of thermal atomization, Roisman et al. [15] studied atomization of droplets in the breakup state on a smooth aluminum substrate. Droplets of varying diameter were caused to impact the surface, and it was found that at a given impact velocity, thermal atomization was present for droplet diameters above some critical value. For impact velocities below about 2 m/s, the critical diameter scales as $1/V_0$. Above 2 m/s, it scales as $1/V_0^2$. Accordingly, Roisman asserts that while Weber number may be a good indicator for the presence of thermal atomization at higher impact velocities, this is not the case for low velocities. It was shown that for these low velocity cases, a dimensionless number representing the ratio of droplet contact time to typical droplet spreading time characterizes the presence of thermal atomization.

1.1.4.2 Droplet Dynamics

Commonly studied dynamics involved in droplet impingement scenarios include maximum spreading diameter, residence time, and maximum rebound height. Residence time is generally defined as the time from droplet impact until the droplet entirely rebounds from the surface. For hydrophilic surfaces, residence time is only applicable in the Leidenfrost state. For SmH or SH surfaces, residence time is defined at all surface temperatures. Maximum rebound height applies to all droplet states except breakup.

It is well established that maximum spreading diameter increases with increasing Weber number for a given surface contact angle and temperature [2, 3, 27]. Antonini et al. [28] performed a study using various surface types (ranging from hydrophilic to hydrophobic) with advancing/receding contact angle hysteresis between 5° and 50°. All tests were performed at room temperature. It was found that for $We < 200$, maximum spreading diameter increases for increasingly hydrophobic surfaces. This trend was not found for $We > 200$. The time to reach maximum spreading was found to decrease with increasing Weber number on hydrophilic surfaces. On hydrophobic surfaces, this trend was seen only at high Weber numbers. Clavijo et al. [3] performed a similar study comparing maximum spreading in the Leidenfrost regime. Four surfaces were

considered: smooth hydrophilic, smooth hydrophobic, post-patterned superhydrophilic, and post-patterned superhydrophobic. It was established that maximum spreading diameter is larger in the Leidenfrost regime than at room temperature on SH surfaces. Various post-patterned surfaces were found to have roughly the same maximum Leidenfrost diameter, which were lower than either of the smooth surfaces, suggesting that surface roughness plays a larger role than wettability. Of the smooth surfaces, the hydrophobic displays a larger maximum diameter than the hydrophilic when in a Leidenfrost state.

Residence time in the film boiling regime has been found to be largely independent of Weber number, surface temperature, and microstructure geometry [27]. However, for superheated hydrophobic surfaces, Park et al. [29] showed that residence time during nucleate boiling decreases with increasing surface temperature.

Regarding droplet rebound height, Li et al. [16] performed a study of three surfaces of varying wettability: a SmH surface with contact angle of 100°, a rough hydrophilic surface with contact angle of 50°, and a rough SH surface with contact angle of 170°. It was shown that for the SmH surface, maximum rebound height increases with surface temperature. This was attributed to the Marangoni effect, which is defined by a surface tension gradient that induces a flow in the direction of increasing surface tension. Maximum rebound height on the hydrophilic and SH surfaces exhibited no dependence on surface temperature. The Marangoni effect was said to be suppressed on these surfaces; on the hydrophilic because of high contact angle hysteresis and on the SH because of inhibited heat transfer to the droplet.

1.1.4.3 Wetting/Dewetting Dynamics

Droplet wetting on microstructured surfaces refers to the presence of the Wenzel state, where liquid penetrates the cavities between structures. For droplets impinging hydrophilic surfaces, this is usually the dominant state. For SH surfaces, the Cassie-Baxter state dominates, though the droplet is prone to wetting upon impact. The main cause of wetting in the impact region is said to be the water hammer pressure [30], which results from liquid compression behind the shock wave envelope [31, 32]. Dewetting is the process of transitioning from the Wenzel back to the Cassie-Baxter state. Rates of dewetting for SH surfaces of various surface microstructure, contact angle, and roughness factor have been investigated. Pittoni et al. [33] recorded dewetting

rate of room temperature graphite surfaces with contact angles of 140° and 160°. It was found that on the 160° surface, wetting was not observed at all. On the 140° surface, the rate of dewetting was found to increase with increasing Weber number. Clavijo et al. [34] considered droplet wetting on post-patterned surfaces of varying structure height and pitch. Weber number and solid fraction were held constant and surface temperature was varied between 20 °C and 95 °C. Height and pitch of the posts were not found to be individually significant, but the ratio of height to pitch (or overall surface roughness) was found to be a major contributing factor in droplet dewetting rate, where increasing roughness leads to increasing dewetting rate. Additionally, increasing surface temperature also increases dewetting rate.

1.1.4.4 Thermal Atomization Dynamics

The size of thermally atomized particles during droplet impingement has been studied by Cossali et al. [14] and Moita and Moreira [13, 35]. It is of note that Cossali combined the traditional analysis method for thermal atomization, high-speed image processing, with phase Doppler anemometry to estimate particle size distribution in impingement scenarios. For more on this analysis method, see also Castanet et al. [36]. It has been found that atomized particle size increases with surface temperature and overall surface roughness. Particle size is inversely proportional to Weber number. Cossali found these trends to be significant in the film boiling regime but not during nucleate boiling.

Clavijo et al. [3] considered the effect of surface wettability on the volume of thermally atomized liquid present (or thermal atomization intensity) in droplet impingement scenarios. Post-patterned superhydrophilic, smooth hydrophilic, SmH, and post-patterend SH surfaces were fabricated from silicon substrates. Surface temperatures from 125 °C to 415 °C and Weber numbers from 10 to 225 were considered. It was found that thermal atomization intensity is lower on the SH surface than on any of the others. The presence of atomization was mapped with surface temperature and Weber number (Figure 1.7), showing that atomization occurs more often on the superhydrophilic and hydrophilic surfaces than the other two. At the lowest Weber numbers and for temperatures under about 300 °C, the superhydrophilic and hydrophilic surfaces always exhibit atomization. The SmH and SH never exhibit atomization for these Weber numbers due to the tendency for droplet rebound, which causes the droplet to maintain a thick lamella for its lifetime.

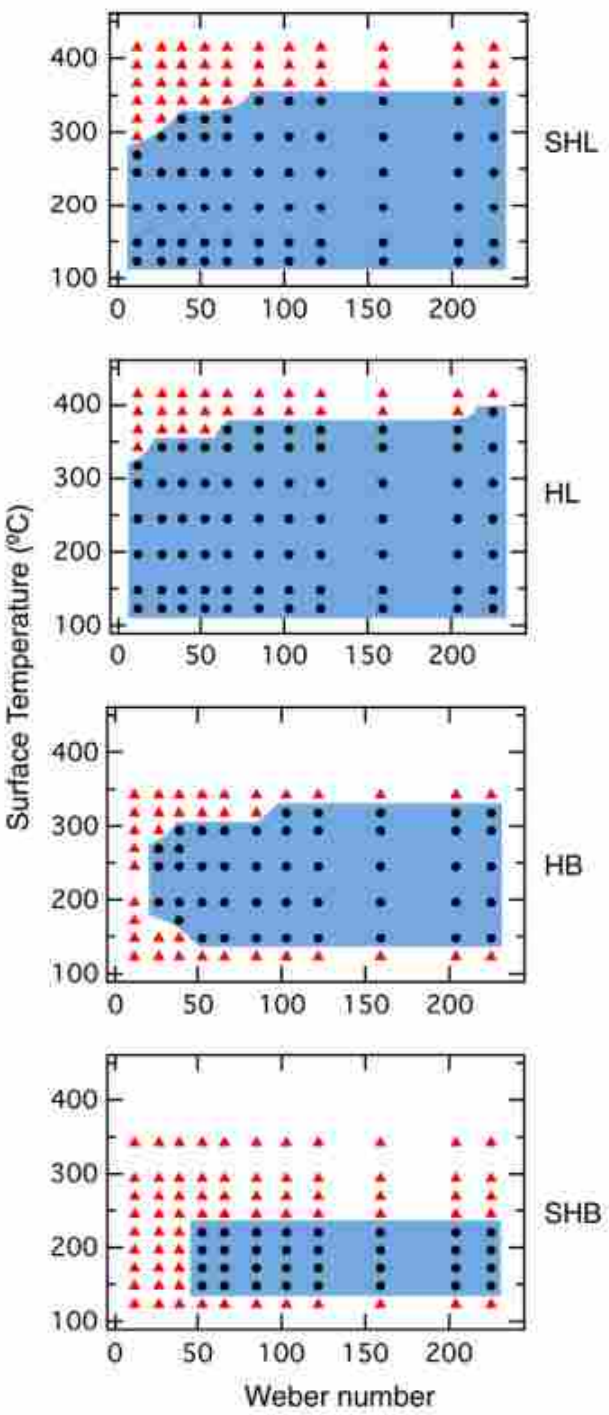

Figure 1.7: Thermal atomization regime map presented by Clavijo et al. [3]. Black circles represent scenarios for which atomization was observed. In this figure, the test surfaces are labeled as follows: SHL: post-patterned superhydrophilic, HL: smooth hydrophilic, HB: smooth hydrophobic, SHB: post-patterned superhydrophobic.

A subsequent study by Clavijo was the first to attempt to quantify specific trends in thermal atomization intensity with time and surface temperature [20]. Three post-patterned SH surfaces of similar solid fraction and varying pitch were used, and Weber number was held constant. A smooth hydrophobic surface was also considered. It was shown that atomization intensity at a given temperature increases with time after impact as the droplet spreads and the lamella thins. Atomization generation begins in the nucleate boiling regime and intensity increases with surface temperature until it reaches a maximum. Intensity then decreases with increasing temperature until the LFP is reached, where atomization is suppressed due to film boiling. Atomization intensity increases with decreasing structure pitch. The lowest pitch surface considered in the study was shown to exhibit even more atomization than is observed on the smooth surface. The inverse relationship of atomization intensity with pitch was attributed to the ability for vapor to escape laterally through the post arrays, which occurs more easily for higher pitch surfaces.

1.1.4.5 Leidenfrost Point

For impinging droplets, the LFP can be defined as the lowest surface temperature for which thermal atomization is no longer observed. LFP has been shown to increase with increasing Weber number [3, 26, 27, 37] and with increasing surface roughness [20, 38]. Hyungdae et al. [38] suggested that as surface roughness (e.g. through the addition of microposts) promotes intermittent liquid-solid contact with the posts, effectively prolonging transition boiling and raising the LFP. Clavijo et al. showed that adding a hydrophobic coating to both smooth and post-patterned silicon substrates significantly reduces the LFP compared to their hydrophilic counterparts [3]. Additionally, Bertola and Sefiane showed that impinging water droplets treated with polyethylene oxide have a much lower LFP than pure droplets.

1.2 Thesis Objectives

This work seeks to quantify trends in thermal atomization during droplet impingement on SH surfaces for varying surface temperatures, Weber numbers, and microstructure configurations. While previous work has been concerned with droplet morphology and the simple question of whether or not atomization occurs during a given scenario, this work seeks to quantify the in-

tensity of atomization. Atomization intensity with time is considered for a droplet, and relative atomized particle velocities are outlined for varying Weber numbers and microstructure configurations. Trends in atomization intensity with surface temperature are of particular interest. The intensity of thermal atomization at a given temperature is compared to the presence of the nucleate, transition, or film boiling regimes. The LFP is compared for varying Weber numbers and microstructure configurations. A relatively new image processing technique is used to estimate thermal atomization, and suggestions for improvement on this technique are explored.

SH surfaces have high potential in many practical applications, but where high heat transfer and boiling is involved, little is understood about the dynamics associated with these surfaces. Characterizing the phenomenon of thermal atomization during droplet impingement on these surfaces gives important insight into these dynamics. Of special interest is the characterization of how SH surface microstructure configuration impacts thermal atomization behavior. This work increases understanding of heat transfer on SH surfaces while also serving as a springboard into further research.

1.3 Thesis Overview

This chapter provided background information, explanation of concepts important to the work herein, and a review of relevant literature. It has not been an exhaustive review of the research leading up to the present work, as any attempt at that would fill volumes. Instead, enough information was provided to give the reader a general understanding of the relevance and importance of the present work. The following chapters will outline the process of gathering and analyzing data and present results, discussion, and conclusions.

Chapter 2 presents methodology for data acquisition and analysis. The experimental setup, important parameters, and associated uncertainties are presented. The image processing technique used to quantify trends in thermal atomization intensity is new and has undergone some revision since the beginning of this work. The process of analyzing high-speed image data will be thoroughly outlined. Recommendations for further improvements of the technique will also be presented.

Chapter 3 is a paper currently in preparation for being submitted to the International Journal of Heat and Mass Transfer (IJHMT) which builds on Clavijo's 2018 study [20]. Droplet impinge-

ment scenarios on a SmH and three post-patterned SH surfaces of similar solid fraction and pitches of 8 μm, 12 μm, and 16 μm are considered for a range of superheat temperatures from 120 °C to 320 °C and Weber numbers of 20, 40, 85, 150, and 200. Trends in thermal atomization intensity are quantified, and a scaling is presented, which models vapor flow through the micropost arrays. It is found that the 8 μm pitch surface always exhibits the highest atomization intensity. Atomization intensity on the SmH relative to the 8 μm pitch is highly dependent on Weber number. The 12 μm and 16 μm pitch surfaces always exhibit much less atomization than the other two, though they display no specific trend in relation to each other. The scaling supports the notion that vapor escape through microposts contributes to the suppression of atomization for surfaces of higher pitch, and that local wetting plays a role as well.

Chapter 4 is a paper also in in preparation for being submitted to the IJHMT. Thermal atomization during droplet impingement on SH surfaces with two distinct microstructure configurations is considered: square posts and square holes. Tests are done for each configuration with structure heights of 4 μm, 8 μm, and 12 μm. Surface temperature varies between 120 °C and 250 °C and Weber numbers of 40, 85, 150, and 240 are considered. Structure spacing and solid fraction are held constant. Comparing the two configurations at each structure height and Weber number, atomization intensity is generally roughly equal or higher on the hole-patterned surface. Some exceptions exist, and reasoning behind this is discussed. Microstructure height significantly affects trends in atomization intensity with surface temperature and Weber number. The LFP is seen to decrease with increasing height. Chapter 5 includes overall conclusions of the work contained in this thesis and suggestions for further research.

CHAPTER 2. METHODOLOGY

This chapter contains descriptions of the SH surface fabrication method, experimental apparatus, and image processing technique. Uncertainty is reported throughout the chapter, and a summary of uncertainty is included as a separate section. A detailed uncertainty analysis is found in Appendix B.

2.1 Fabrication of SH Surfaces

As discussed in Chapter 1, SH surfaces are the product of surface microroughness and hydrophobic surface chemistry. The surfaces used in the present work are fabricated using a series of processes in the Clyde Building cleanroom facility on BYU campus. The fabrication method will be discussed in this section.

Each of the SH surfaces used in the present work is fabricated by etching a microstructure pattern into a silicon wafer and coating the surface with Teflon. Reactive-ion etching is performed on the wafer, where the surface is placed under a vacuum and subjected to a plasma which bombards it with high-energy ions. Figure 2.1 shows scanning electron microscope (SEM) images of the three types of surface microstructures used in the present work: circular posts, square posts,

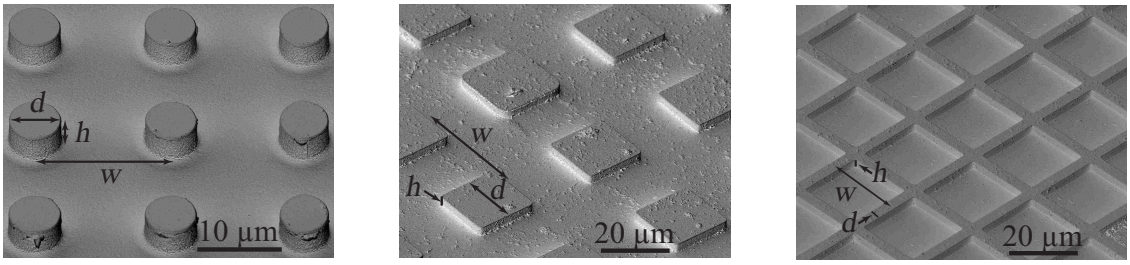

Figure 2.1: SEM images of the three microstructure types used in the present work: (a) circular posts with $w = 16$ μm, $d = 5$ μm, $h = 4$ μm, (b) square posts with $w = 40$ μm, $d = 20$ μm, $h = 4$ μm, and (c) square holes with $w = 24$ μm, $d = 4$ μm, $h = 4$ μm.

and square holes. Each microstructure pattern is accomplished by first applying photoresist to the wafer to block the etching process in desired areas (e.g. top of posts or top of hole walls). Because of the crystalline structure of the silicon, etching occurs essentially normal to the surface. The depth of the etch is determined by the number of etching cycles the wafer is exposed to.

The photoresist pattern is applied by spin-coating the entire wafer with resist and exposing it to ultraviolet (UV) light under a photomask. The mask assures that the wafer is exposed only in the desired areas. Two types of photoresist are used, positive and negative. When positive resist is exposed to UV light, its structure weakens and becomes more soluble. The wafer can then be immersed in a developer solution until the weaker, exposed resist dissolves, leaving the desired pattern. When negative photoresist is exposed, it polymerizes and becomes less soluble, so when it is developed, the exposed resist remains. Using the same mask, positive and negative resists will leave opposite patterns. Photomasks are made from glass, with chrome printed on the surface to block UV light in the desired pattern. The process of applying photoresist to the wafer is referred to as photolithography.

After etching, the remaining photoresist is removed with acid, and a thin layer of chromium is deposited on the wafer using an electron beam evaporator. A chromium source and wafer are placed in a chamber under vacuum, and the electron beam hits the chromium, evaporating it. The wafer is placed above the source and is coated as source material is evaporated. The chromium layer is strictly for adhesion, since Teflon doesn't adhere well to silicon. Teflon is then applied. Upon completion of the surfaces, sessile and dynamic contact angles are measured. A droplet on the surface is imaged (or filmed in the case of dynamic angles) with high background contrast using an SLR camera. Images are then processed using an existing MATLAB code. Contact angle measurements have been determined to have uncertainty of about $\pm 3^\circ$. Sessile contact angles for the SH surfaces used for the present work are nominally 150°. Advancing angles are nominally 160° with hysteresis between 5° and 15°. The sessile angle on the SmH is about 115° with advancing angle of 120° and hysteresis of 7°.

Appendix A contains a step-by-step description of the surface fabrication process, including information about the equipment and materials used. This description applies to the SH surfaces that were fabricated for the studies outlined in this thesis. Additional information about the equipment and processes used can be found on the BYU cleanroom website.

2.2 Experimental Setup

Experiments are performed to quantify trends in the volume of atomization present during droplet impingement on SmH and various micropatterned SH surfaces for a range of surface temperatures from 120 °C to 320 °C and Weber numbers from 20 to 240. The temperature range is restricted by the Teflon, which degrades at around 340 °C. Figure 2.2 shows a schematic of the experimental setup. High-speed images are captured at 3000 fps using a Photron APX RS Fastcam. A 105 mm lens is used with 92 mm of extension tubes. F-stop is set at f/11. The camera is positioned with the lens about 15.5 cm from the impacting droplet and focused on the point of impact. Each frame is 1024 $\times$ 1024 pixels, and spatial resolution (which allows parameters like droplet diameter and impact velocity to be calculated for each scenario) is nominally 12 μm/pixel. Droplets are dispensed by a syringe whose height can be adjusted to vary Weber number. Droplet diameter is held constant at nominally 2.26 $\pm$ .01 mm.

The surface to be tested is placed on an aluminum block, which is heated with two embedded cartridge heaters. A SOLO 9696 temperature controller and K-type thermocouple are used to monitor and control the temperature of the block. The thermocouple is placed in a small hole drilled into the side of the block about 1 cm deep and 0.5 cm below the surface. Discrepancies between the thermocouple readout and actual temperature of the surface were tested by taking infrared (IR) temperature measurements on a silicon wafer painted matte black. Measurements were captured using a FLIR SC6100 IR camera. Emissivity of the surface was assumed to be 0.97. Figure 2.3 shows an example readout from the IR camera for a test surface at 190 °C. The discrepancy between the thermocouple and IR measurements was found to be consistently 1.8%. Additionally, the temperature variation across the wafer was about 3 °C. Heating was found to be fairly uniform in the center of the wafer, and the edges tended to be slightly cooler than the center, as seen in Figure 2.3. Combined uncertainty in surface temperature, including uncertainty associated with the temperature controller and thermocouple, was estimated at about $\pm$3 %. Very little heat is removed during a single droplet impingement event [39], and the time it takes to save high-speed data is sufficient for the surface to again reach a steady state before another test. A halogen lamp is used to illuminate the droplet. Because of temporal variations in background intensity that arise from alternating current, the lamp is run by direct current. Sandblasted glass diffuses the light and

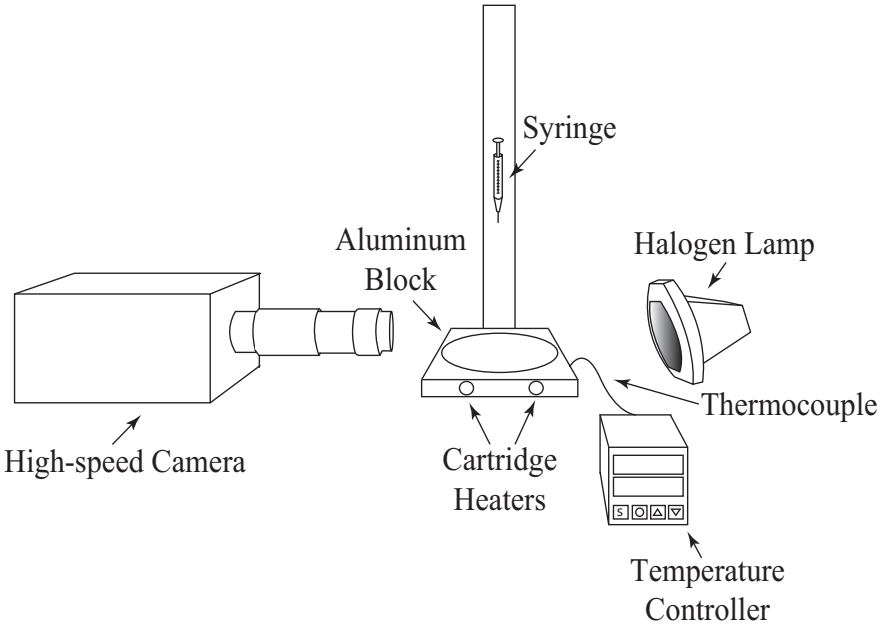

Figure 2.2: Experimental setup consisting of a high-speed camera, syringe, aluminum block with embedded cartridge heaters, halogen lamp with sandblasted glass, temperature controller, and thermocouple.

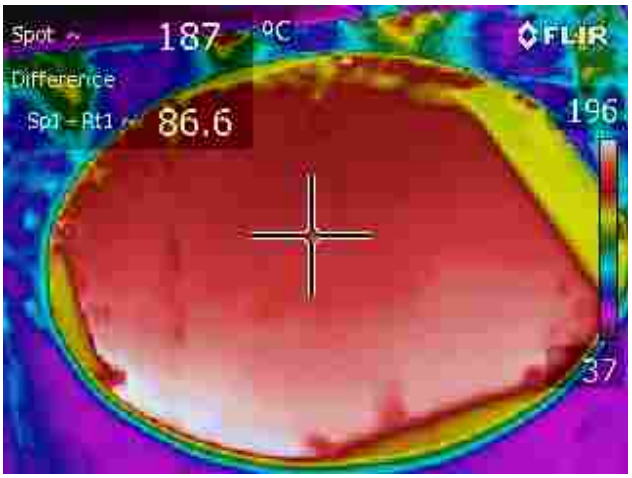

Figure 2.3: Example screen shot of the IR read-out for a matte black test surface at 190 °C.

maintains a uniform background. Halogen lighting produces a significant amount of heat, so the lamp is kept turned off at all times except during an impingement event.

High-speed images of droplet impingement events are saved in grayscale TIFF format, beginning with the frame just before the droplet enters the field of view. Between 40 and 80 frames are saved, depending on Weber number, to capture all atomization behavior. A data set consists of impingement events on one surface at one Weber number for a range of surface temperatures beginning with 120 °C. Temperature is increased by 10 °C or 20 °C increments until the LFP (which varies surface-to-surface) or temperature limit is reached. Between 15 and 30 trials are recorded at each temperature.

Prior to recording a data set, spatial resolution, Weber number, and droplet intensity are calculated to assure that these parameters fall within the desired range. In order to calculate spatial resolution, a droplet is dropped onto the aluminum heating block (at room temperature), a ruler is placed directly above it, and one frame is recorded. The frame is loaded into MATLAB, and spatial resolution is calculated in μm/pixel by dividing the known physical distance between two points by the number of pixels between those points.

For the Weber number calculation, an impingement event at room temperature is recorded on the test surface. Droplet diameter and impact velocity to be used in the Weber number calculation are measured from this event in the manner described in Section 2.3. Droplet intensity is defined as the maximum difference between pixel values in the primary droplet and the background. The purpose of tracking this parameter is to assure that the background lighting stays as consistent as possible between data sets; it is held at a value of approximately 0.7. Spatial resolution, Weber number, and droplet intensity are averaged over at least three separate images or events. Additionally, one hundred frames of the background with no droplet present are saved to quantify background noise. These frames are used in thresholding during image processing. The image processing methods used to calculate each of these parameters are described in the next section.

2.3 Image Processing Method

Image processing is used in the present work for two main purposes: to calculate experimental parameters such as Weber number and droplet intensity and to estimate thermal atomiza-

tion intensity. All image processing was performed using MATLAB version R2018a, and existing MATLAB functions for image processing such as `imread`, `im2bw`, and `regionprops` were utilized. The first step in processing a given frame is locating any liquid present. The procedure by which this is done is the same for both calculating droplet properties and estimating atomization intensity. After that, the procedure changes based on the desired operation. Methods for identifying liquid, calculating properties, and estimating atomization are detailed in this section. Limitations of the atomization intensity calculation will then be discussed, and suggestions for further improvements will be given.

2.3.1 Identifying Liquid Locations

The first step in all of the image processing procedures is to identify the locations of any liquid droplets that may be present in the frame. Figure 2.4 shows the various stages in locating liquid droplets for two example frames ($t = 0$ ms is shown left and $t = 3$ ms is shown right) of a droplet impinging a SmH surface at $T_s = 220$ °C and $We = 85$. These stages are marked by the original frame, difference frame, and binary frame; each of which will be discussed below. Note that the frames in Figure 2.4 are cropped to 850 × 850 pixels or about 10.2 × 10.2 mm.

A grayscale image is loaded into the program as a matrix of values between zero and one, representing pixel intensities where zero is black and one is white. All of the operations performed on the image are element-wise matrix operations. Columns and rows of the matrix represent horizontal and vertical locations in the frame, respectively, and each frame represents a particular instant in time. The original image, shown in Figure 2.4a, is subtracted from the blank background frame (the frame just prior to the droplet entering the field of view). An absolute value is taken to produce the difference image displayed in Figure 2.4b. In the difference frame, pixels associated with liquid have nonzero values while background pixels are zero. Some noise may be introduced in this step in the form of pixels which don't represent liquid but still have nonzero values in the difference frame. This commonly occurs near the edge of the impinging droplet due to a slight distortion in the background around the droplet edge. It can also be due to random flickering in the background lighting.

To create a binary image, the MATLAB function `im2bw(IM,T)` is used, where `IM` is the matrix representing the difference frame and `T` is a pixel intensity threshold. The result is a

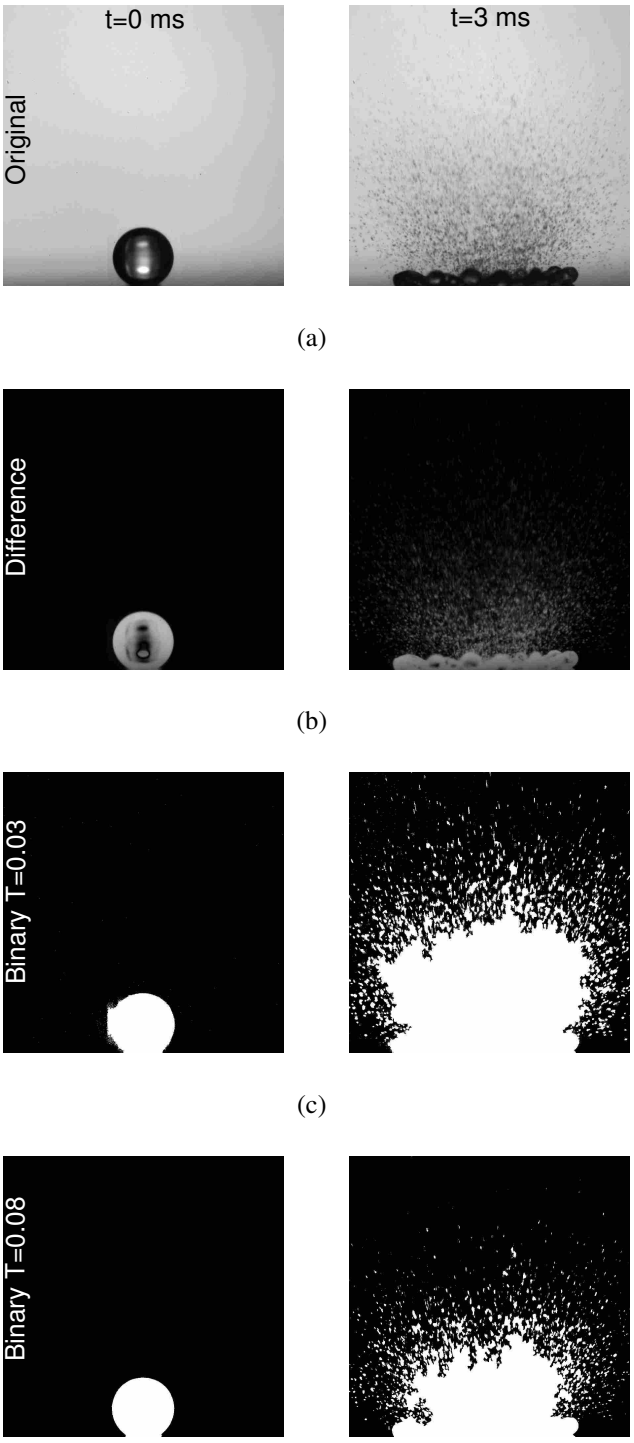

Figure 2.4: Visual process of locating liquid present in a frame. The stages are (a) original image, (b) original subtracted by the background (difference image), (c) binary image using $T = 0.03$, and (d) binary image using $T = 0.08$. Images are for a droplet impinging a SmH surface at $T_s = 220$ °C and $We = 85$ for t=0 ms (left) and t=3 ms (right) and are cropped to 850 $\times$ 850 pixels.

binary image where all pixels with a value less than `T` in the difference frame become zero and all other pixels become one. This threshold should be chosen high enough to minimize noise and low enough so as to not cut off the edges of the liquid. Note the difference between Figure 2.4c, which uses a low threshold (0.03) and contains significant visible noise, and Figure 2.4d, which appears to accurately represent the actual location and size of liquid droplets in each pictured frame using a threshold of 0.08. The methods for choosing a threshold will be discussed in the following sections. Note the dark area of the droplet seen in the left frame of Figure 2.4b. Occasionally, this dark area translates to a black region within the white droplet in the binary image. These black regions are eliminated using MATLAB's `imfill` so that droplet properties can be accurately obtained.

The MATLAB function `regionprops(BW,P)` can be used on a binary image to produce a MATLAB `struct` that contains a list of white space regions and their properties. Here, `BW` is the binary image produced from the difference frame, and white space represents liquid in the frame. `P` is a list of properties. Thus, the `struct` represents a list of liquid regions and for the purposes of the current research contains the properties: `Area`, `Centroid`, `BoundingBox`, and `PixelList`. `Area` and `Centroid` properties are fairly straightforward: for a given region listed in the `struct`, `Area` is the number of pixels in the region and `Centroid` is the geometric centroid. `BoundingBox` is an array that specifies the location of the upper-left corner, width, and height of a box that completely encloses the region. `PixelList` is a matrix that contains the locations of each pixel in the region.

2.3.2 Calculating Droplet Properties

Weber number and droplet intensity for a given data set are determined from the impingement events at room temperature discussed in Section 2.2. Six frames in total are processed beginning before droplet impact and the last frame being the impact frame, as depicted by Figure 2.5, where t represents time before impact. Note that the images shown are the difference frames which have the initial background subtracted. A MATLAB `struct` of liquid regions is obtained after the manner laid out in Section 2.3.1. The threshold, `T`, for converting the difference frame to binary is chosen visually. Ideally, the `struct` would contain only one region, but in the case that some noise or a reflection of the droplet in the test surface is present, the primary droplet is chosen

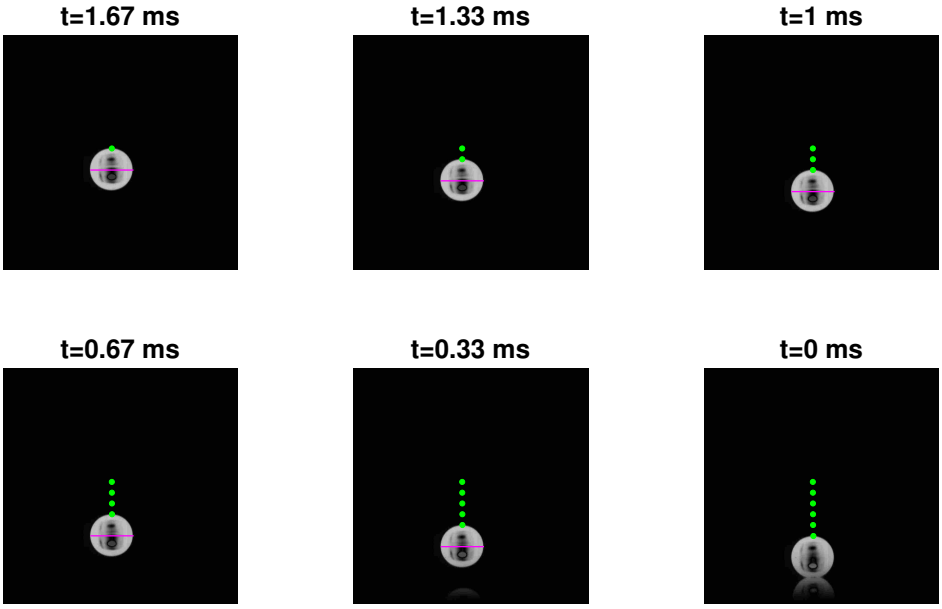

Figure 2.5: Example of sequential frames used to calculate droplet diameter and impact velocity for a droplet impinging a SmH surface at room temperature and $We = 85$. Frames are portrayed in the "difference" stage, where the background has been subtracted, and t is time before impact. Note that $T = 0.08$ was used in the binarization stage. Green dots in each frame represent the location of the top of the droplet in the current and preceding frames. The magenta line in each frame represents the calculated diameter. Diameter is not calculated for the impact frame.

to be the region with the largest `Area` property. This method of choosing the region representing the droplet is checked visually, and has been accurate for all the scenarios considered.

For each frame that is processed, the droplet diameter (shown as the magenta lines in Figure 2.5) is calculated in pixels as $D_0 = \sqrt{4A_p/\pi}$, where A_p is the `Area` property of the droplet (number of pixels in the region). This is then converted to millimeters using the spatial resolution that was calculated previously. Note that diameter is not calculated for the impact frame because the calculation assumes a circular projected droplet area, which is usually not the case at impact. The impact velocity is estimated by tracking the location of the top of the droplet in each frame (using the `BoundingBox` property). This location is marked by green dots in Figure 2.5. The pixel distance traveled by the droplet between two successive frames is obtained and converted to

meters, and this value is divided by the time step between frames to obtain a velocity in m/s. This calculation is performed for each of the five possible successive image pairs, and impact velocity is taken to be the average of these. Weber number is then calculated as $We = \rho V_0^2 D_0/\sigma$, where ρ and σ are density and surface tension of water at room temperature.

In this work, droplet intensity is taken to be the maximum pixel value (from the difference frame) in the region representing the primary droplet. This is calculated simply by locating the primary droplet and isolating the maximum value.

2.3.3 Estimating Atomization Intensity

Thermal atomization intensity on a given test surface and for a given surface temperature and Weber number is estimated from 15 to 30 separate impingement events and averaged. Each event is processed frame-by-frame so that manual adjustments may be made where necessary. The frame to be processed is cropped to a field of view of 10.2 $\times$ 10.2 mm with the droplet centered horizontally, and the aforementioned `struct` of liquid regions is obtained. The threshold used to convert the frame to binary (using `im2bw(IM,T)`) is calculated the same way for each data set. The threshold is presumed to be largely dependent on the background brightness and the noise due to lighting flicker. To calculate the threshold, at least 100 background images without a droplet present are used. The first frame of these is dedicated as the point of reference, and the absolute value of the difference between this frame and each other frame is calculated. Any remaining nonzero pixel values in these frames after subtracting them are considered background noise. These pixel values are averaged, and the threshold is chosen to be ten standard deviations above this noise average. This method of thresholding was chosen based on visual observation of multiple impingement events in an attempt to normalize noise between data sets. Ten standard deviations is a somewhat arbitrary value that was found to minimize noise in many scenarios without cutting off droplet edges.

To proceed with the atomization estimation, atomized liquid particles that are present in the frame must be isolated from the primary droplet and any secondary droplets that may be created by means other than thermal atomization (such as droplet breakup or rebound). To do this, a mask is created. Figure 2.6 depicts the process of masking the primary droplet using the same two example frames shown in Figure 2.4. To produce the mask shown in Figure 2.6b, first a size threshold is

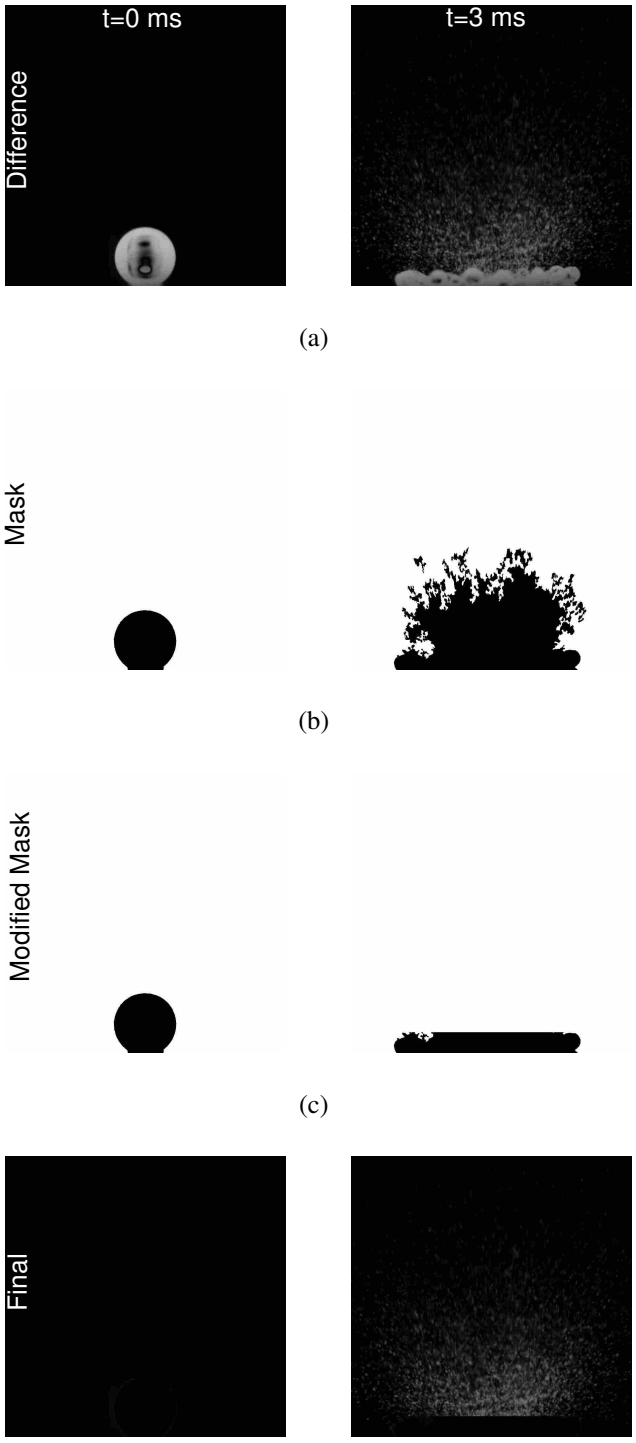

Figure 2.6: Image processing steps: (a) the difference image, (b) a mask produced from a binary image with $T = 0.08$, (c) the manually modified mask, and (d) the final image, produced by multiplying the modified mask and difference frame. Images are for a SmH surface at $T_s = 220$ °C and $We = 85$ for t=0 ms (left) and t=3 ms (right) and are cropped to 850 × 850 pixels.

chosen, so as to only consider liquid regions from the `struct` that are significantly larger than an atomized particle. This size threshold is chosen manually and can be adjusted between processing impingement events. Generally, a threshold of 1000 pixels is sufficient, but at high Weber numbers where droplet breakup is common, a lower threshold may be chosen to accommodate smaller secondary droplets. The mask is first assigned to be a matrix of size equal to that of the difference frame, where each value in the matrix is one. All regions in the `struct` with the `Area` property greater than the size threshold are isolated. The locations of pixels in each of these regions are obtained using the `PixelList` property, and these are set to zero.

As seen in the right frame of Figure 2.6b, atomized particles may overlap each other where atomization is abundant, causing large regions of atomization to be included in the mask. This may be remedied manually by choosing a region and setting all pixel values in this region to one, thus subtracting from the mask. Similarly, if there are any regions that ought to be masked but are not, the mask may be modified by addition. In general, one or two mask adjustments are required to account for noise and excessive thermal atomization. When a suitable mask is obtained, the final frame is produced by multiplying the the mask by the difference frame. This produces an image such as is seen in Figure 2.6d. Note that due to noise, there will always be nonzero pixel values in the final frame, even where atomization isn't actually present. The final value for atomization intensity is taken to be the sum of nonzero pixel values in the final frame. Note that due to the three-dimensional nature of the atomization spray, some particles appear more in-focus than others in the frame. These in-focus particles carry a higher contrast with the background, and are thus weighted more heavily in the final intensity value.

For each impingement event, atomization intensity through time is adjusted to account for droplet delay in the impact frame. Time is considered to begin at initial droplet impact, as shown in the left frames of Figures 2.4 and 2.6. However, the droplet in the impact frame is often in an advanced stage of impingement, and in these scenarios, atomization intensity is forced to zero at $t = 0$ and linearly interpolated between calculated values. It has been seen that this method of interpolation has a minimal effect on the overall intensity results.

2.3.4 Limitations of Atomization Intensity Calculation

Because of the three-dimensional nature of thermal atomization, the total volume of thermal atomization cannot be quantified with the approach outlined here, which only captures atomization in a plane. Even using two cameras simultaneously could only capture atomized particles on the very edges of the spray. Therefore, the image processing method seeks only to identify trends in atomization intensity for the various scenarios considered in this thesis. These trends have proven to be repeatable when effort is taken to standardize parameters such as background lighting and noise, but the controlling of these parameters has yet to be perfected. The current method of controlling lighting is the use of droplet intensity, as discussed above. Two main problems persist with this method. The first is that not all factors affecting contrast are currently known, and are therefore unlikely to be taken into account with this single parameter. One of the biggest factors appears to be supply voltage of the halogen lamp. However, voltage can only be safely adjusted up to about 120 V, giving only limited control over contrast. Other factors may include the angle of the lamp and the surrounding light, but these have yet to be successfully manipulated to affect contrast.

Another problem with using droplet intensity as it is currently calculated is that it is difficult to control background uniformity, so the parameter may not represent the background lighting in the entire field of view. In some scenarios the background is visually uniform, and in others there is a region close to the test surface that appears darker than the rest of the background. This causes contrast to change based on where droplets are in the field of view and renders the droplet intensity less useful as a controlling parameter. Controlling uniformity by changing the light angle has been somewhat successful but gives a limited range of control. This problem merits further investigation. Improving the method for analyzing background lighting will greatly enhance the ability to control experimental conditions and improve repeatability of experiments.

Variation in background lighting not only affects calculated atomization intensity, but is also a major contributor to the noise that was discussed in Section 2.3.1. A standardized threshold for the conversion to binary using `im2bw(IM,T)` has been used in an attempt to reduce this type of noise (as discussed in Section 2.3.3), but it has been found to do little to prevent variations in the amount of noise present between frames. Noise is increased in frames where the sides of the droplet are exposed, such as in the impact frame or during droplet rebound. Additionally,

there is often temporal variations in noise during an impingement event, which may be caused by unavoidable light flicker. In some scenarios, these sources of extra noise may be eliminated manually by modifying the droplet mask, but this method is ineffective when large quantities of atomized particles are present, as they become intermixed with noise (see Figure 2.4c). Rather than using the standardized threshold, manually choosing the threshold used to convert to binary for each frame would likely be a more viable solution to reducing noise. However, the extra human error introduced by doing this should be investigated.

The method of time-adjusting atomization intensity using interpolation has been shown to affect overall results very little, since any given scenario will only be shifted by a maximum of one time step. The interpolation method also introduces a slight discontinuity by forcing intensity to zero at $t = 0$, because measured intensity never actually reaches zero due to noise. For these reasons, it would be advisable to simply abandon this practice in future work.

It has been observed that low image contrast has a detrimental effect on the visibility of small droplets. To date, very little investigation into increasing contrast has been performed, either in the experimentation or post-processing stages, and this area should be considered for further improvements. It is worth mentioning that the impingement experiments are time-consuming and often must be performed over the space of days or weeks, so lighting conditions, equipment setup, and other parameters are bound to change between experiments. While high-speed imaging is a convenient method of capturing thermal atomization, other methods that are not dependent on surrounding lighting could also prove beneficial, such as phase Doppler anemometry [14, 36].

Overall, the image processing technique is a convenient and repeatable method for estimating trends in thermal atomization intensity during droplet impingement scenarios. The accuracy and precision of this technique is largely dependent on environmental variables, and methods for controlling these variables, while currently adequate, merit further investigation.

2.4 Uncertainty of Experimental Parameters

An uncertainty analysis was performed on all important experimental parameters, and a summary of uncertainty is provided here. A detailed explanation of the uncertainty analysis and 95% confidence intervals are found in Appendix B. Note that atomization intensity, as calculated by the image processing technique, is a relative value and is dependent on parameters such as

background lighting for which accurate uncertainty cannot be predicted. The repeatability of atomization intensity measurements is estimated using a 95% confidence interval, as explained in Appendix B.

2.4.1 Atomization Intensity

Atomization intensity is measured for between 15 and 30 impingement events for each scenario considered using the image processing technique. The final value of atomization intensity in a given scenario is taken to be the average of these trials. As discussed above, atomization intensity is calculated as the sum of pixel intensities in the "final frame" (see Figure 2.6). For the various studies considered in this thesis, atomization intensity is normalized. However, in order to give a complete summary of the relative atomization intensity on each test surface considered, atomization intensity in this section is presented as the raw calculated value.

Six surface microstructure shapes are considered for the research in this thesis (see Figure 2.1): smooth (no microstructure), 8 μm pitch circular posts, 12 μm pitch circular posts, 16 μm pitch circular posts, 40 μm pitch square posts, and 24 μm pitch square holes. Table 2.1 gives 95% confidence intervals for the atomization intensity found for each of these microstructures. In each case, microstructure height is 4 μm, Weber number is 85, and surface temperature is chosen to maximize atomization intensity. Surface temperature is 220 °C for the smooth, 300 °C for the 8 μm pitch posts, 180 °C for the 12 μm and 16 μm pitch posts, 160 °C for the square posts, and 140 °C for the square holes.

2.4.2 Surface Microstructure Configuration

Surface microstructure parameters (height, width, and pitch) are measured with a Zeta 20 3D optical profilometer with reported error of $\pm$ 1%. Sessile and dynamic contact angles are measured with image processing using an automated polynomial fitting method. This method has been shown to have error less than $\pm 3^{\circ}$ [4].

Table 2.1: 95% confidence interval for atomization intensity. For each microstructure shape, height is 4 μm, Weber number is 85, and surface temperature is chosen to maximize atomization intensity: 220 °C for the smooth, 300 °C for the 8 μm pitch posts, 180 °C for the 12 μm and 16 μm pitch posts, 160 °C for the square posts, and 140 °C for the square holes.

Microstructure	Atomization Intensity	Confidence Interval	Confidence Interval (%)
Smooth	28,750	$\pm$ 1,079	$\pm$ 3.8%
8 μm Pitch Circular Post	37,710	$\pm$ 1,594	$\pm$ 4.2%
12 μm Pitch Circular Post	511	$\pm$ 212	$\pm$ 41.4%
16 μm Pitch Pircular Post	523	$\pm$ 175	$\pm$ 33.4%
Square Post	157	$\pm$ 31	$\pm$ 19.9%
Square Hole	240	$\pm$ 24	$\pm$ 9.9%

2.4.3 Experimental Parameters

Table 2.2 displays uncertainties for spatial resolution, droplet diameter, impact velocity, Weber number, and surface temperature. For most of these parameters, the actual measured values differ slightly from the value reported throughout this thesis. This has been done for convenience, and both reported and measured values are presented here. Additionally, some parameters have a range of values associated with them, and for these parameters the maximum uncertainty is reported.

Table 2.2: Reported and measured values used in this work and their corresponding uncertainties.

Parameter	Reported Value	Measured Value	Maximum Uncertainty
Spatial Resolution (μm/pixel)	12	11.94	$\pm$ 0.3%
Droplet Diameter (mm)	2.3	2.26	$\pm$ 1.1%
Impact Velocity (m/s)	-	0.84 – 2.76	$\pm$ 4.3%
Weber Number	20 – 240	21.9 – 237.8	$\pm$ 8.7%
Surface Temperature (°C)	120 – 320	118.4 – 316.6	$\pm$ 3.5%

CHAPTER 3. EFFECT OF WEBER NUMBER AND MICROPOST ARRAY CONFIGURATION ON THERMAL ATOMIZATION INTENSITY DURING DROPLET IMPINGEMENT ON POST-PATTERNED SUPERHYDROPHOBIC SURFACES

This chapter is in preparation for being submitted to the International Journal of Heat and Mass Transfer. The format has been been modified to meet the requirements of this thesis.

3.1 Contributing Authors and Affiliations

Preston Emerson, Julie Crockett, Daniel Maynes Department of Mechanical Engineering, Brigham Young University, Provo, Utah 84602

3.2 Abstract

An experimental study of thermal atomization during droplet impingement on hydrophobic and superhydrophobic surfaces of varying microstructure was performed. A smooth hydrophobic and three different post-patterned superhydrophobic surfaces of similar solid fraction were investigated. Atomization quantity was estimated using a high-speed image processing technique and found to be dependent on the micropost array pitch, surface temperature, and Weber number. Three main mechanisms are hypothesized to account for atomization dynamics in these scenarios: lamella thickness, droplet wetting, and vapor escape through the microposts. It was found that atomization generally increases with increasing Weber number and decreasing pitch, but the relationship between droplet wetting and vapor escape is more complex. In addition, Leidenfrost point was found to increase with increasing Weber number and decreasing pitch. A scaling model was developed to explore the effect of resistance to vapor flow through the micropost arrays on atomization, which describes the experimental findings well.

3.3 Introduction

The study of liquid droplet impingement provides insight into droplet morphology and heat transfer in real world applications such as spray cooling of metals and fuel injection in combustion engines. When a water droplet impacts a solid surface heated above the saturation temperature, boiling takes place and in some scenarios the rising vapor bubbles burst through the lamella, causing a spray of very small droplets away from the surface. This phenomenon is called thermal atomization, and understanding it is integral to understanding heat transfer during droplet impingement. Classic pool boiling regimes (convective, nucleate, transition, and film) have been shown to apply to impinging droplets [1, 3, 15, 17–20], where the regime depends mainly on the surface temperature, T_s, and partially on the Weber number [17], defined as $We = \rho V_0^2 D_0/\sigma$. Here, ρ and σ are the droplet density and surface tension, respectively, D_0 is initial droplet diameter, and V_0 is droplet impact velocity. The relative amount of thermal atomization present in an impingement scenario is directly linked to the boiling regime [17, 19, 20], where the bulk of atomization occurs during nucleate boiling, which is characterized by the rapid formation of vapor bubbles. At some surface temperature within nucleate boiling, the quantity of atomization reaches a maximum, and transition boiling begins. As the surface temperature increases beyond this point, the vapor bubbles begin to grow larger and merge until a stable vapor film is formed between the impacting droplet and the surface. The onset temperature of the film boiling regime is called the Leidenfrost point (LFP), and it is marked by the total suppression of atomization, as the vapor film insulates the droplet and allows lateral vapor escape through the film layer.

In recent years, the popularity of microstructured superhydrophobic (SH) surfaces has grown in fluids and heat transfer research. The water-repelling nature of these surfaces can be attributed to the presence of the Cassie-Baxter state, which occurs when water sits atop surface microstructures without penetrating the air cavities below. This leads to reduced liquid-solid contact and high droplet contact angles. However, when water penetrates the air cavities, the Wenzel state occurs and drop mobility on the surface is inhibited. This state is also referred to as wetting. It has been shown that for SH surfaces, surface microstructure configuration significantly affects the heat transfer and boiling regimes for both pool boiling [8] and droplet [3, 20, 40] scenarios. Figure 3.2 shows the three SH microstructure configurations used in this study and shows the characteristic parameters: structure shape (circular posts), height (h), pitch, or center-to-center spacing (w), and

solid fraction, or the ratio of liquid-solid contact area to total projected surface area (f_s). Searle et al. [8] showed that in pool boiling applications, post-patterned SH surfaces exhibit a very low LFP and a more gradual transition from nucleate to film boiling, while rib-patterned surfaces yield a higher LFP and more abrupt transition. It was also noted that heat transfer during nucleate boiling increases with solid fraction. Hays et al. [40] showed a similar trend with solid fraction for heated, sessile droplet scenarios.

The effect of microstructure on droplet boiling behavior and morphology on SH surfaces can be attributed mainly to the air cavities which reside beneath the droplet. Figure 3.1 illustrates three important dynamics affecting droplet morphology and thermal atomization for a droplet impinging a SH surface in the nucleate boiling regime. First, as the droplet spreads, the droplet lamella grows thin, and vapor bubbles form in the lamella, which may burst through and cause thermal atomization. A thinner lamella leads to less resistance to rising bubbles bursting through. Lamella thickness is a function of Weber number, where increasing Weber number leads to a thinner lamella and greater thermal atomization intensity (amount of thermal atomization present) [26].

Wetting often occurs at the stagnation point of an impinging droplet when liquid penetrates the cavities between structures [30, 33, 34]. This leads to temporarily higher liquid-solid contact area in the stagnation region, which causes more boiling to occur and increases thermal atomization intensity. Subsequently, dewetting occurs, when the liquid exits the cavities and the Cassie-Baxter state is again present. In a 2009 study, Deng et al. [30] asserted that, initially, wetting in the stagnation region is driven mainly by the water hammer pressure, which results from liquid compression behind the shock envelope that develops upon impact [32]. Within approximately 1 ms, the water hammer pressure dissipates, and the dynamic pressure governs wetting behavior in the droplet spreading phase. Pittoni et al. [33] found that for SH graphite surfaces at room tem-

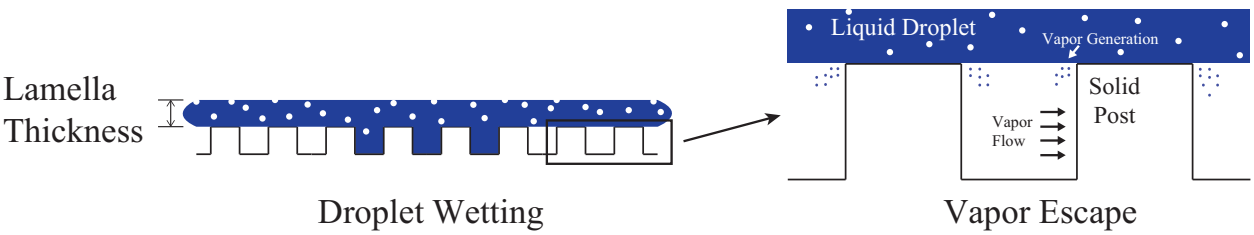

Figure 3.1: Schematic of a droplet impinging a microstructured SH surface in the nucleate boiling regime, such as the ones shown in Figure 3.2.

perature, dewetting rates for impinging droplets increase with increasing Weber number. Clavijo et al. [34] showed that for post-patterned SH surfaces at subcritical temperatures, dewetting rate increases with surface temperature. Clavijo also showed that the roughness factor of the surface, $r = 1 + \pi dh/w^2$, is integral in determining dewetting rates. Here, d is micropost diameter. Clavijo's model showed that increasing roughness factor increases the surface energy gradient between the Wenzel and Cassie states, which in turn increases the rate of dewetting.

The final important factor for impact behavior illustrated in Figure 3.1 is vapor escape. Vapor bubbles that are formed in the spreading droplet may escape laterally through the channels that exist between microstructures (see Figure 3.2). Vapor escape may be limited by high flow volume through narrow structure pitch. Surface microstructure configurations that allow greater vapor escape are hypothesized to suppress thermal atomization during droplet impingement by decreasing the volume of vapor that is forced through the lamella. As pitch increases, both droplet wetting and vapor escape occur more easily, resulting in competing effects on the generation of thermal atomization such that the dominant effect is often not readily apparent.

In a 2018 study by Clavijo et al. [20], thermal atomization during droplet impingement was quantified for a smooth hydrophobic (SmH) and three post-patterned SH surfaces of similar solid fraction and varying pitch. Weber number was held constant for all experiments. It was shown that for the SH surfaces, the amount of atomization present in an impingement scenario decreases with increasing pitch. This behavior was attributed to the increased ability for vapor escape, reducing the amount of vapor that must burst through the lamella. An analytical model by Ishino et al. [42] for viscous forces of a fluid flowing through a micropost array was used to justify this finding, demonstrating the inverse relationship between pitch and the drag force of the flow. Clavijo also showed the LFP to be dependent on pitch.

Here, thermal atomization intensity for SmH and post-patterned SH surfaces is explored for a range of Weber numbers and surface temperatures. The SH surfaces have similar solid fraction and varied pitch (8 μm, 12 μm, and 16 μm), and contact angle is held constant at nominally $\theta = 150^\circ$. While previous work has been mainly concerned with whether or not atomization exists in a given scenario, here it is shown that by adjusting microstructure pitch the intensity of atomization in a scenario can be manipulated while maintaining constant surface contact angle. A

scaling analysis is developed to describe experimental results, which includes stokes drag on vapor flowing laterally through the micropost arrays.

3.4 Methodology

This section outlines the fabrication process for SH surfaces, the droplet impact experimental setup, and the image processing technique used to evaluate thermal atomization intensity.

3.4.1 Substrate Fabrication

Surface superhydrophobicity can be produced by applying micro- or nano-roughness and a hydrophobic coating. This allows for the presence of the Cassie-Baxter state, reducing the liquid-solid contact area. Scanning electron microscope (SEM) images showing the surface microstructure of the SH surfaces used in this study are shown in Figure 3.2. Photolithography is used to deposit a micropost array mask onto a silicon wafer, which is then etched via ion etcher to $h \approx 4$ μm. A layer of chromium (nominal thickness of 100 nm) deposited on the surface is necessary for adhesion of Teflon, which is applied by spin coating, resulting in a thickness of nominally 200 nm.

Table 3.1 provides micropost array dimensions (measured using an optical profilometer with uncertainty of $\pm 1\%$) for each SH surface considered. Sessile contact angles of the SH surfaces are $150^\circ \pm 3^\circ$ with advancing/receding angle hysteresis between 6° and 15°. A SmH surface with a sessile contact angle of $115^\circ \pm 3^\circ$ was fabricated by coating a smooth silicon wafer with Teflon.

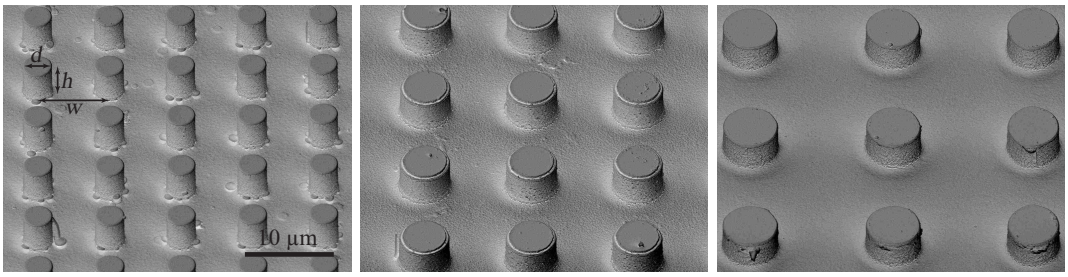

(a) (b) (c)

Figure 3.2: SEM images of the micropost arrays of the (a) 8 μm (b) 12 μm and (c) 16 μm pitch surfaces. The scale bar applies to all three images.

Table 3.1: Micropost array dimensions measured with an optical profilometer for each SH surface.

Surface	Pitch (μm)	Diameter (μm)	Solid Fraction
8 μm pitch	7.97	3.29	0.134
12 μm pitch	11.93	4.11	0.093
16 μm pitch	15.92	3.36	0.035

3.4.2 Experimental Apparatus

A schematic of the experimental setup is shown in Figure 3.3. Water droplets of nearly constant diameter, $D_0 = 2.3 \pm .024$ mm, are dispensed from a syringe whose height can be adjusted to vary Weber number. The silicon substrate sits atop an aluminum heating block, heated with cartridge heaters and kept at constant temperature using a SOLO 9696 temperature controller with a K-type thermocouple. Impingement events are captured as TIFF images at 3000 fps using a Photron APX RS Fastcam. A halogen lamp is positioned behind the droplet, and light is diffused through sand-blasted glass, producing a uniform background. Spatial resolution for all scenarios is nominally 12 μm/pixel. Weber numbers of 20, 40, 85, 150, and 200 are considered for each surface with uncertainty ranging from ± 1.9 for $We = 20$ to ± 6.1 for $We = 200$. Events are captured in increments of 20 °C from 120 °C to 320 °C $\pm$ 3%. The temperature range is restricted by the Teflon, which degrades at temperatures above about 340 $^{\circ}C$. Between 10 and 20 trials are captured at each temperature, from which average results are calculated.

3.4.3 Image Processing

High-speed images were analyzed for thermal atomization intensity using MATLAB in the same fashion used by Clavijo [20]. A summary of the analysis method is included here. The image processing technique is two-dimensional and sensitive to environmental variables in the experimentation stage, the most important of which are background lighting and spatial resolution. Impingement events are saved in grayscale TIFF format, beginning with the frame just before the droplet enters the field of view (the background image) and given sufficient time after impact to allow for all atomization behavior to be observed.

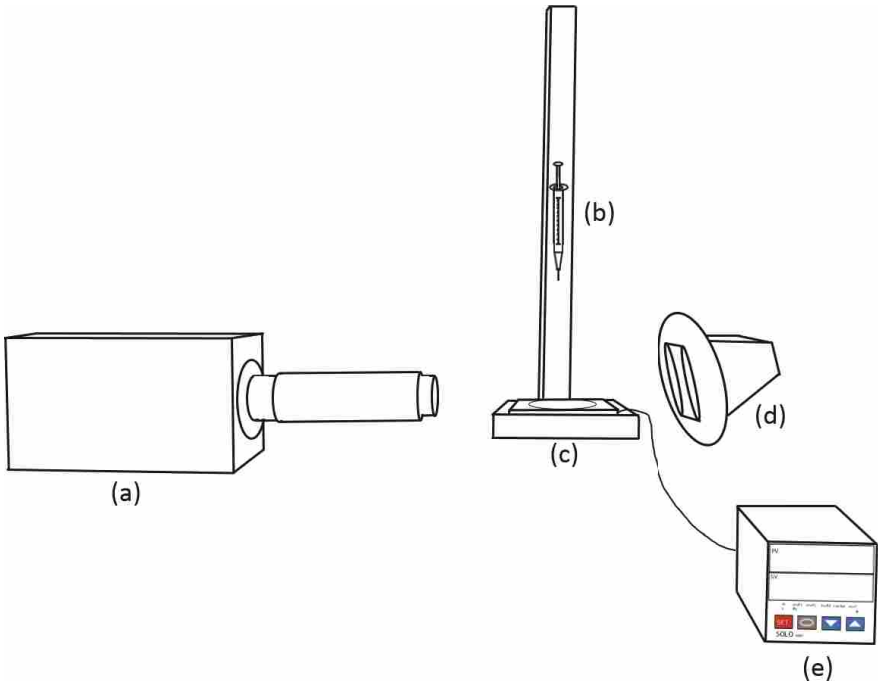

Figure 3.3: Schematic of the experimental setup consisting of (a) high-speed camera (b) needle to dispense water droplets (c) heating block with cartridge heaters (d) halogen backlight (e) temperature controller with thermocouple.

The frame to be analyzed is cropped to have a field of view of about 10.2 $\times$ 10.2 mm with the droplet centered horizontally. The background image is subtracted from the original image to reduce noise. The total intensity of in-plane atomization in the frame, A, is found by summing the values of pixels in the background-subtracted frame that contain atomization. Because of the three-dimensional nature of the atomization spray, some atomized particles appear more in-focus (and thus darker) in the original frame. The pixels associated with these particles hold higher value in the background-subtracted frame, so they are weighted more heavily in the final value of A.

Thermal atomization results will be presented in this study as the normalized value $A^* = A/A_{max}$, where A_{max} is the maximum value of A over the range of surface temperatures considered for the SmH surface at $We = 85$. This scenario is the same that Clavijo used to normalize, and it represents a transition Weber number for droplet breakup behavior. Figure 3.4 displays the droplet morphology at maximum spread for impingement on the 8 μm pitch surface for a range of Weber numbers and surface temperatures. Breakup is characterized by droplets being ejected from the periphery of the primary droplet. These droplets are generally much larger than those of thermally

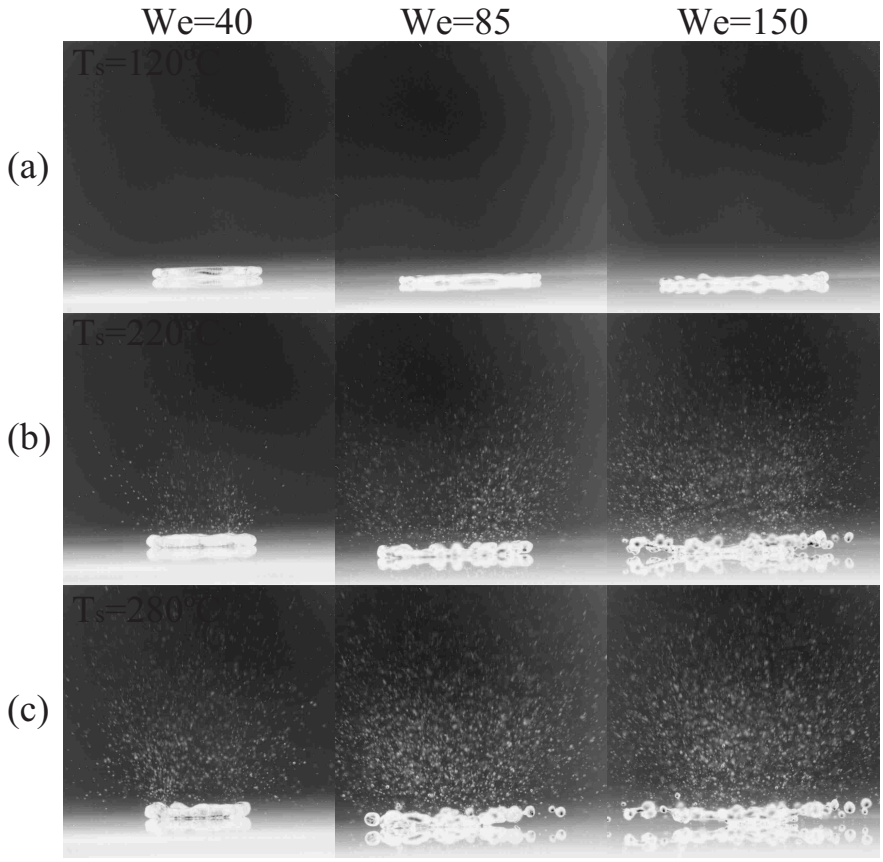

Figure 3.4: Droplet morphology on the 8 μm pitch SH surface approximately 3 ms after impact at (a) 120 $^{\circ}C$ (b) 220 $^{\circ}C$ and (c) 280 $^{\circ}C$, and for $We = 40$, 85, and 150.

induced atomization. This can be seen in Figs. 3.4b and 3.4c. Where breakup occurs, the primary droplet is often seen to begin to levitate above the surface rather than rebounding. In this study, where $We < 85$ breakup behavior was rarely observed, and the droplet retracts and rebounds off the surface. For $We > 85$, breakup occurs at most surface temperatures explored. It is observed that for Weber numbers where droplet breakup occurs, the likelihood of breakup increases with surface temperature. For $We = 85$, breakup occurs only at the highest surface temperatures explored.

3.5 Results and Discussion

In Figure 3.5 the temporal progression of an impinging droplet on the SmH and 8 μm pitch surfaces is shown for $T_s = 240$ $^{\circ}$C and $We = 85$. For this scenario, both surfaces exhibit about the same atomization intensity. Atomization is generated as the droplet spreads and vapor

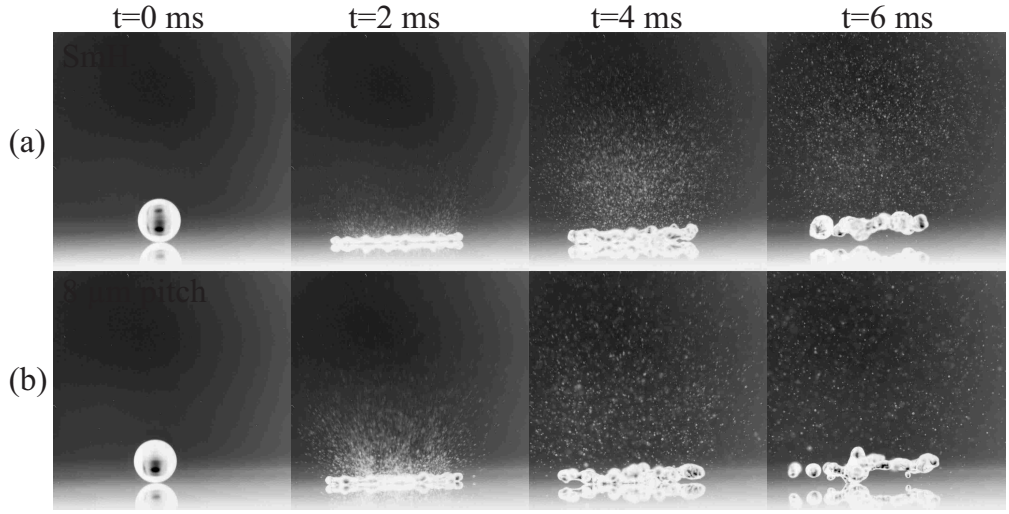

Figure 3.5: Time progression of a droplet impinging the (a) SmH surface and (b) 8 μm pitch surface at $We = 85$ and $T_s = 240$ °C.

bubbles are forced through the lamella. By $t = 4$ ms, atomization generation appears to have ceased and atomized particles are leaving the field of view. At $t = 6$ ms the primary droplet has begun to levitate. The rate at which particles leave the field of view is indicative of the velocity with which the atomized particles are traveling. From these experiments, the approximate start time of atomization and the time for which atomized particles begin leaving the field of view can be estimated. Although exact time atomization generation ceases is not able to be determined with any accuracy, high-speed images seem to indicate that generation ceases before a significant volume of fluid droplets begin exiting the field of view.

Figure 3.6 displays A^* throughout the life of the droplet at the maximum atomizing temperature for each surface ($T_s = 220$ °C for the SmH, $T_s = 280$ °C for the 8 μm pitch, and $T_s = 180$ °C for the 12 μm and 16 μm pitch surfaces). Time, t, is measured from droplet impact with a timestep of $\Delta t = 0.33$ ms. Plot insets show the low-atomizing cases (12 μm and 16 μm pitch surfaces). Note that $A^* < 0.001$ is assumed zero, and some cases are left out of the insets because they fall below this threshold. The trends in A^* confirm the visuals of Figure 3.5: A^* initially increases with time (as atomization is generated) and reaches a maximum value, $A^*_{max,t}$, before decreasing (as atomized particles leave the field of view). The time at which $A^*_{max,t}$ occurs is the time when atomized particles begin leaving the field of view.

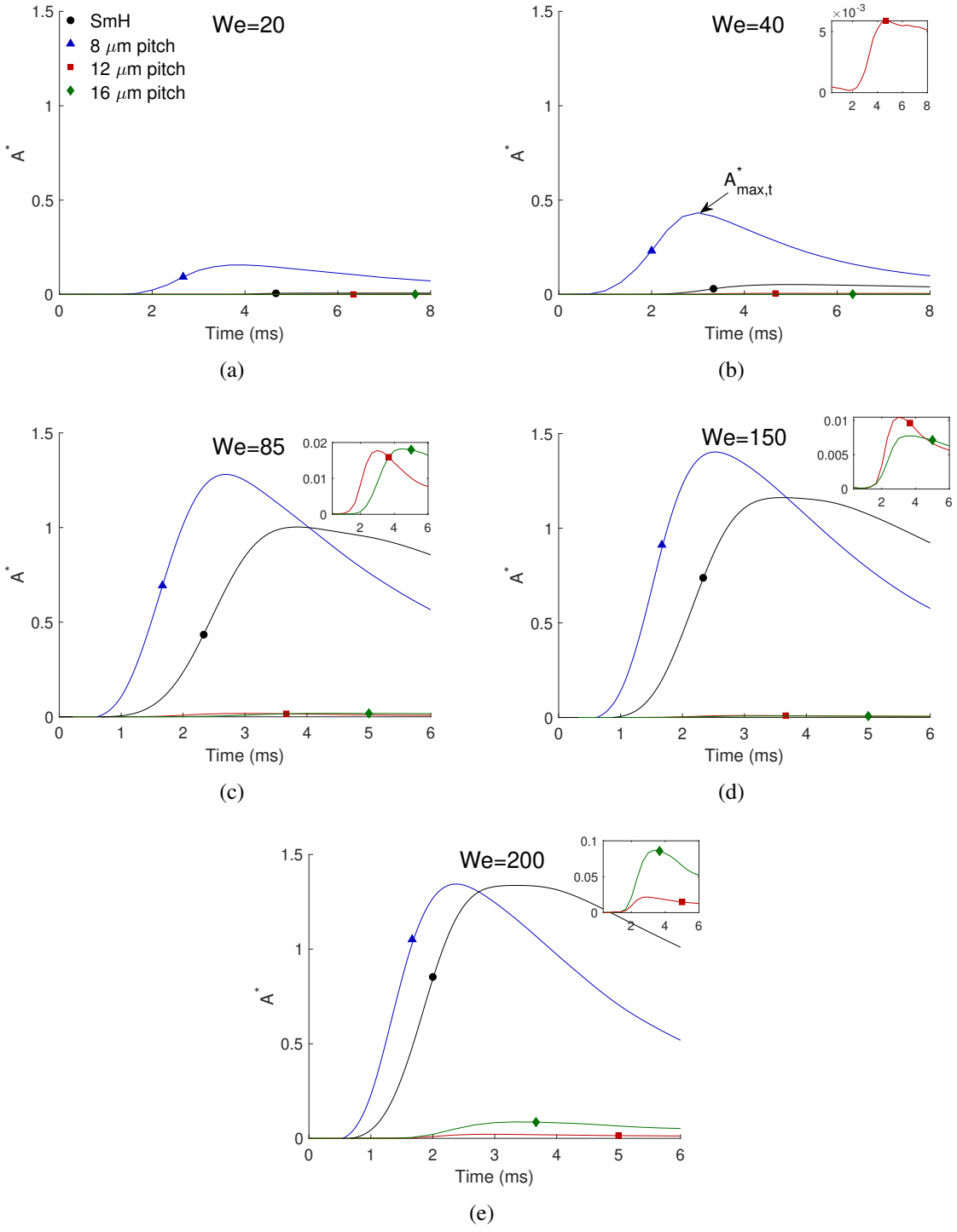

Figure 3.6: Thermal atomization intensity plotted as a function of time on each surface at (a) $We = 20$ (b) $We = 40$ (c) $We = 85$ (d) $We = 150$ and (e) $We = 200$. The data corresponds to a surface temperature that results in the highest atomization intensity for each surface: 220 °C for SmH, 280 °C for 8 μm pitch, and 180 °C for 12 μm and 16 μm pitch. Plot insets display A^* with a smaller scale to show trends for the 12 μm and 16 μm pitch surfaces. Note that $A^* < 0.001$ is assumed zero, and some cases are left out of insets because they fall below this threshold.

Maximum atomization intensity is significantly affected by both pitch (in the case of SH surfaces) and Weber number. For all of the surfaces considered, atomization intensity increases with increasing Weber number. This is attributed to the fact that increasing Weber number promotes a thinner lamella, which provides less resistance to vapor bubbles bursting through. Interestingly, the SmH surface does not exhibit the highest thermal atomization intensity. In fact, at $We = 20$ and $We = 40$ the amount of atomization present on the SmH is noticably smaller than on the 8 μm pitch SH surface. Lamella thickness is not expected to change significantly between surfaces, so droplet wetting on the 8 μm pitch is the likely cause for enhanced atomization intensity on this surface. As Weber number increases, the difference in atomization intensity between the SmH and 8 μm pitch surfaces decreases considerably, until (at $We = 200$) maximum atomization is virtually the same on both surfaces. Although wetting increases at elevated Weber number, Pittoni [33] showed that the rate of droplet dewetting also increases with Weber number, which may explain why these surfaces exhibit more similar atomization intensities at high Weber numbers.

Both the 12 μm and 16 μm pitch SH surfaces always exhibit much less atomization than the SmH and 8 μm pitch surfaces. We hypothesize that suppression of atomization on these surfaces is attributed mainly to their larger pitch, which allows relatively easy vapor escape beneath the droplet. It should be noted that wetting would also occur on these surfaces, but vapor escape presumably dominates over wetting effects. Their slightly smaller solid fractions may also play a minor role in the suppression of atomization through decreased heat transfer. A scaling model to explore the influence of vapor escape will be presented in Section 3.6 and describes the results well. Clavijo showed that atomization quantity decreases with increasing pitch at $We = 85$. However, the present results of Figure 3.6 show that atomization on the 16 μm pitch surface is not always lower than on the 12 μm pitch surface. This is most evident at $We = 200$. The difficult balance between droplet wetting and vapor escape likely causes this behavior, and will be discussed further below.

Regarding the slopes of the A^* vs. time curves, where A^* is increasing and decreasing, the slope steepens as Weber number increases. This is consistent for all surfaces, and implies an increased atomization generation rate and particle velocity with Weber number. Since generation rate and particle velocity are directly tied to atomization intensity, which also increases with increasing Weber number, this result is expected.

At $We = 20$ and $We = 40$, where the SmH surface exhibits small A^*, the increasing and decreasing slopes of the data are small, suggesting a low generation rate and slow moving particles. The magnitude of the decreasing slope for the data in Figure 3.6b is very small for this surface, suggesting that at $We = 40$, most of the atomized particles stay within the field of view for the entire measured time. However, the slopes for the 8 μm pitch SH surface, which exhibits significantly more atomization than the other surfaces at $We = 20$ and $We = 40$, are much steeper, suggesting larger generation rates and particle velocities. At $We = 200$, maximum atomization intensities on the SmH and 8 μm pitch surfaces are almost identical. As is the case at all of the Weber numbers considered, the slopes for the 8 μm pitch SH surface remain steeper than those for the SmH surface. The insets in Figure 3.6 show that atomization generation rate and particle velocity also increase with Weber number for the 12 μm and 16 μm pitch surfaces. For Weber numbers where maximum atomization intensity is comparable on these surfaces, the 12 μm pitch surface exhibits greater generation rates and particle velocities.

Similar to maximum atomization intensity and atomized particle velocity, the onset time of atomization is a strong function of Weber number and pitch. For all surfaces tested, the atomization initiation time occurs earlier as Weber number increases, as can be seen in Figure 3.6. Atomization generation is dependent on the amount of vapor generated, lamella thickness, and the ability for vapor escape. At higher Weber number, the droplet spreads faster, resulting in greater liquid-solid contact and a thinner lamella at earlier times. The earliest atomization initiation time is always observed for the 8 μm pitch SH surface, and the variation in initiation time for this surface shows the smallest depenence on Weber number. Initiation time for the SmH occurs at around 4 ms at $We = 20$, while it is 1 ms at $We = 200$. The initiation time for the SmH surface approaches that for the 8 μm pitch surface as Weber number increases. Initiation time for the 12 μm and 16 μm pitch surfaces is between 3 ms and 4 ms at low Weber number and around 1 ms at high Weber number, similar to the SmH. The influence of each of the mechanisms affecting atomization initiation time merits further investigation.

Figure 3.7 presents $A^*_{max,t}$ as a function of surface temperature for each Weber number. Data for low atomizing scenarios (mainly the 12 μm and 16 μm pitch surfaces) are shown in the insets. Boiling regimes can be identified in this figure by observing trends in relative atomization intensity with surface temperature. The onset temperature for atomization marks the beginning of nucleate

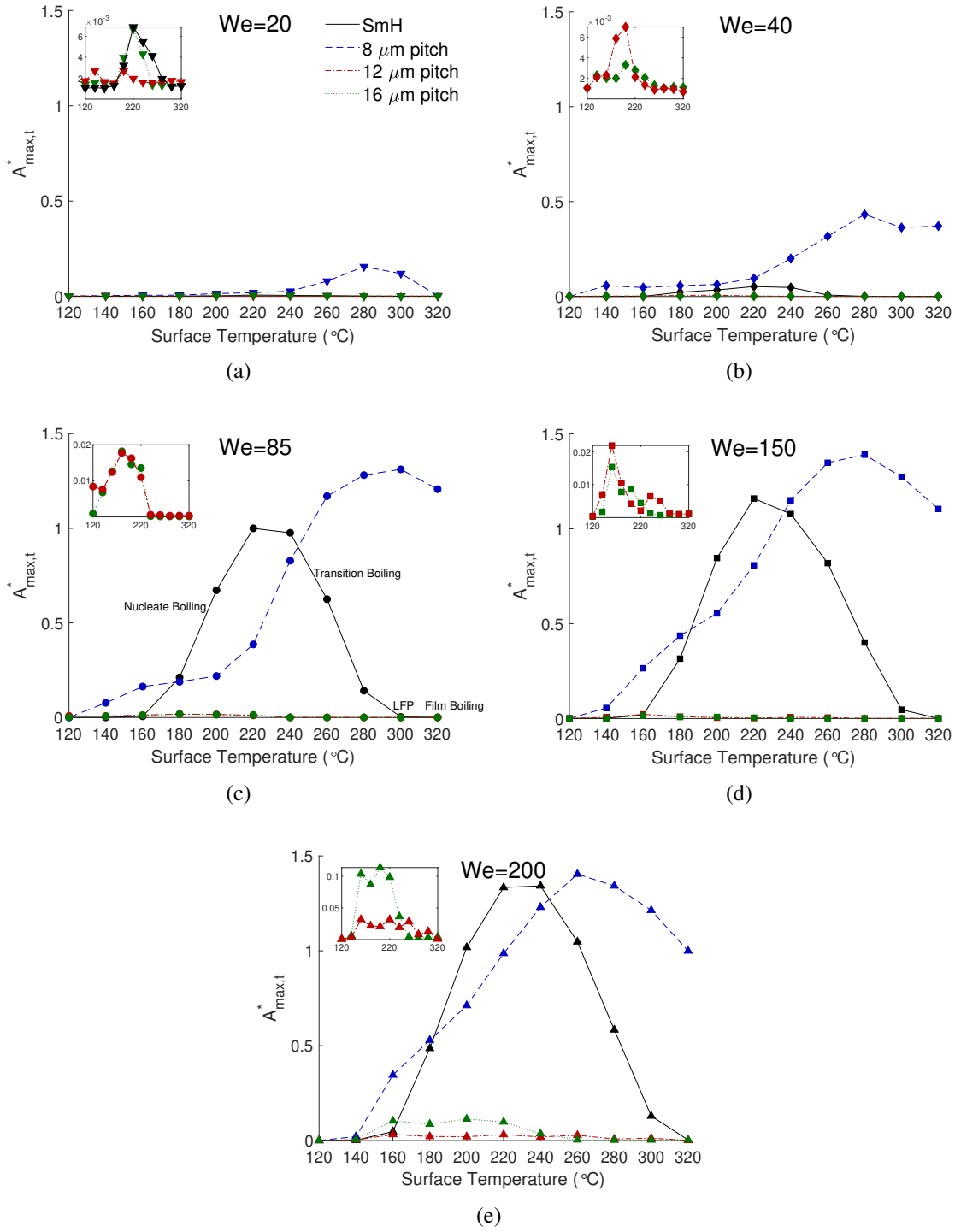

Figure 3.7: Maximum observed atomization intensity as a function of surface temperature for all surfaces considered at (a) $We = 20$ (b) $We = 40$ (c) $We = 85$ (d) $We = 150$ and (e) $We = 200$. Plot insets show trends for low atomizing scenarios (12 μm and 16 μm pitch surfaces). In the $We = 85$ plot, boiling regimes and the LFP for the SmH surface are labeled.

boiling. As temperature increases in the nucleate boiling regime, atomization intensity increases, as more and more vapor bubbles form in the droplet lamella. Atomization intensity decreases with increasing surface temperature during transition boiling, until the LFP is reached, where the droplet impinges on a stable vapor film and atomization is suppressed. A striking difference in data trends is observed for the SmH surface compared to the three SH surfaces. The nucleate boiling regime on the SmH surface begins at around 160 °C, and $A^*_{max,t}$ increases steeply in this regime. Nucleate boiling continues until approximately 220 °C, where the maximum atomization intensity is observed for the temperature range. Transition boiling is then present until the LFP at around 320 °C.

For each of the SH surfaces, the onset of nucleate boiling occurs at a lower temperature compared to the SmH surface, around 140 °C. On the 8 μm pitch SH surface atomization intensity increases more gradually with surface temperature, experiencing a prolonged nucleate boiling regime and peaking at a higher temperature than for the SmH surface. Transition boiling can be observed, starting about $T_s = 280$ °C. The LFP appears to be higher than the maximum temperature explored here except for the $We = 20$ case, where the LFP seems to occur at 320 °C. High-speed images reveal that for surface temperatures of 300 °C and 320 °C, only half the impingement events on the 8 μm pitch surface result in the film boiling regime, with no atomization present. For the other impingement events, atomization characteristic of nucleate boiling is observed. These two results (film boiling and nucleate boiling) occur randomly during repeat trials at the same temperature, suggesting that the transition to film boiling is still occurring in this temperature range.

There is a range of surface temperatures in the nucleate boiling regime where $A^*_{max,t}$ is higher for the SmH surface than for the 8 μm pitch SH surface, generally between $T_s = 180$ °C and 240 °C. Above this range, the SmH surface has a quick transition to film boiling, while the 8 μm pitch surface continues to yield higher quantities of atomization. In a 2012 study on pool and droplet boiling near the LFP, Hyungdae et al. [38] found that increasing surface roughness (e.g. by adding microposts) promotes intermittent wetting during transition boiling, allowing for increased liquid-solid contact and effectively raising the LFP. For the surfaces in this study, the increased roughness caused by microposts on the 8 μm pitch surface likely promotes intermittent wetting, allowing for a higher LFP than on the SmH surface. We hypothesize that from 180 °C to 240 °C,

vapor escape, rather than intermittent wetting, is the dominate factor, causing lower atomization intensity on the 8 μm pitch surface for this range of temperatures.

For the 12 μm and 16 μm pitch surfaces, the LFP occurs at lower temperatures than for the SmH and 8 μm pitch surfaces, especially at low Weber numbers. On these surfaces, vapor escape through the microposts should be much greater than for the 8 μm pitch surface, as will be shown in Section 3.6. The range of temperatures for which atomization is present on these surfaces increases modestly with increasing Weber number. In general, results show that the LFP decreases with increasing SH surface pitch. This may be explained by the tendency for droplet wetting on each of the surfaces. Clavijo [34] found that the roughness factor, $r = 1 + \pi dh/w^2$, has a significant effect on the rates at which impinging droplets dewet a surface, where dewetting rate increases with roughness factor. 12 μm and 16 μm pitch surfaces have lower roughness than the 8 μm pitch surface, prolonging liquid-solid contact. This promotes the formation of a stable vapor film and decreases the LFP.

In Figure 3.8, $A^*_{max,t}$ is shown as a function of surface temperature for each surface considered. Note the difference in scale for the 12 μm and 16 μm pitch surfaces. For all surfaces, $A^*_{max,t}$ generally increases with Weber number. This is to be expected considering the thinner lamella associated with high Weber numbers. On both the SmH and 8 μm pitch SH surfaces, the increase in $A^*_{max,t}$ between $We = 20$ and $We = 85$ is much larger than the increase between $We = 85$ and $We = 200$. This supports the findings of Pittoni [33] discussed above, that dewetting rate increases with Weber number, leading to less noticeable wetting effects at high Weber numbers. It is also likely that some critical Weber number exists which is associated with maximum possible atomization intensity. Increasing Weber number beyond this will no longer have any effect on $A^*_{max,t}$. LFP also appears to increase with Weber number for all surfaces considered here, concomitant with enhanced wetting at high Weber numbers, delaying the formation of a stable vapor film.

3.6 Scaling Analysis

A scaling analysis is now performed to estimate trends in resistance to vapor flow through a micropost array. Vapor formed during boiling in a droplet spreading on a post-patterned SH surface may enter the channels between microposts and flow laterally beneath the droplet. We hypothesize that decreasing resistance to vapor flow in the channels results in the suppression of

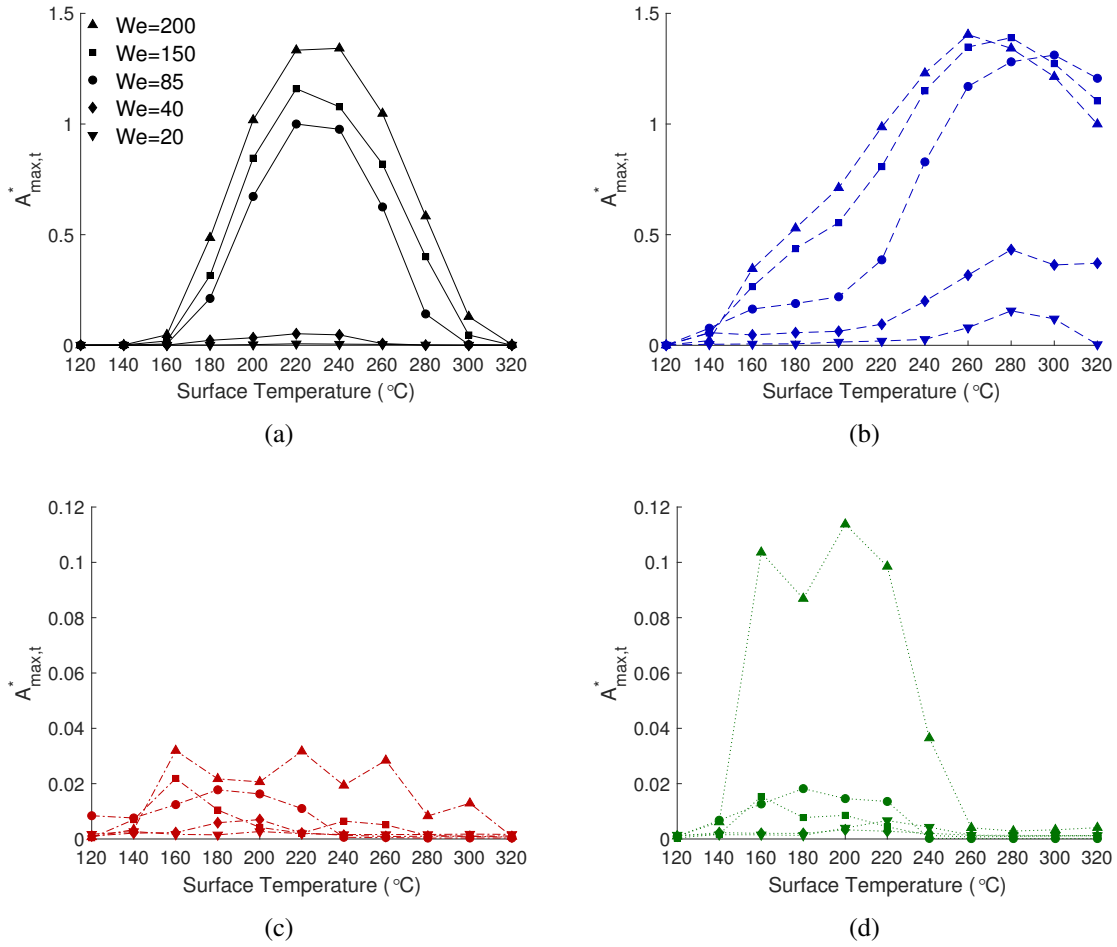

Figure 3.8: Maximum observed thermal atomization intensity as a function of surface temperature at each Weber number for (a) the SmH (b) the 8 μm pitch (c) the 12 μm pitch and (d) the 16 μm pitch surfaces. Note the change of scale between the high-atomizing surfaces (SmH and 8 μm pitch) and low-atomizing surfaces (12 μm and 16 μm pitch).

atomization by limiting the amount of vapor to burst upwards through the droplet lamella. It will be shown that the resistance to flow between microposts scales with three main parameters: surface temperature, Weber number, and pitch of the post array. Results of the scaling will be compared to the experimental data to show that resistance to vapor flow between posts is indeed a good predictor of thermal atomization intensity. It should be noted that resistance to vapor bubbles rising in the droplet lamella and bursting through is also important in determining atomization intensity in a given scenario. However, this scaling focuses solely on vapor flow between microstructures.

3.6.1 Derivation

Both droplet boiling and vapor flow between microposts are complex phenomena, and many assumptions are made for the purposes of this scaling. Boiling is assumed to always be in the nucleate boiling regime, where increasing vapor generation is associated with increasing heat flux (as opposed to transition and film boiling, where vapor contributes to insulation of the droplet). The droplet is also assumed to be in the Cassie-Baxter state for the duration of impingement, and wetting effects are completely neglected. During spreading, vapor flows radially in all directions beneath the droplet from the center to the edge. We consider here vapor flow along one radius of the droplet in a direction of flow parallel to the rows of posts. Figure 3.9 depicts vapor flowing between posts in this direction. A unit cell of the micropost array is defined as the area between four posts, illustrated by the dashed line in Figure 3.9a, where w, the width of the unit cell, is set to be equal to the pitch of the post array. The flow is given a no slip condition when flowing between posts, and zero shear is assumed along all other boundaries of the unit cell, as shown. Figure 3.9b shows the vapor flow rate, Q, through the unit cell. Continuity yields the following:

$$Q_{uc} = Q_{in} + Q_{gen} \tag{3.1}$$

where Q_{uc} is total vapor flow rate through the unit cell, Q_{in} is vapor flow into the unit cell from previous cells, and Q_{gen} is vapor generated due to boiling which then enters the unit cell.

In a 2009 publication, Tamayol and Bahrami [44] modeled Stokes flow through a unit cell identical to the one shown in Figure 3.9a. Here, relatively low flow velocities through the microchannels are likely, such that Stokes flow can also be assumed. Tamayol derived the pressure drop across a unit cell, ΔP_{uc}, as a function of flow rate:

$$\Delta P_{uc} = \frac{\mu Q_{uc}}{w^2} f\left(d/w\right) \tag{3.2}$$

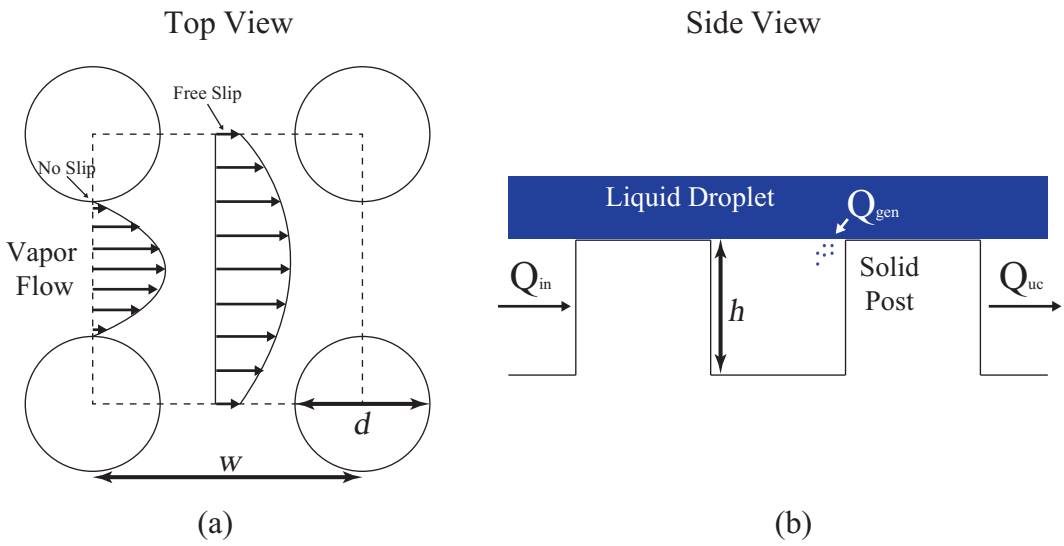

Figure 3.9: Schematic of vapor flow through a unit cell of the micropost array depicting (a) a top view (unit cell is outlined by the dashed line and velocity profiles are shown) and (b) a side view showing vapor flow rate (Q) in and out of the unit cell.

where,

$$f(d/w) = 6\left\{\frac{2(d/w)}{1-(d/w)^2} + \frac{3(d/w)^2\left[\tan^{-1}\left(\frac{d/w}{\sqrt{1-(d/w)^2}}\right)+\frac{\pi}{2}\right]}{(1-(d/w)^2)^{5/2}}\right\} + 12(1-d/w)\left[\frac{1+1.274f_s}{2}\right] \tag{3.3}$$

Note that in order to conform with Tamayol's expression, vapor flow rate is taken to be the average volumetric flow rate through the post array per unit height of the posts. Here, μ is dynamic viscosity of the flow. For the purposes of this analysis, a scaling of the total pressure drop from the center to the edge of the spreading droplet, ΔP_{tot}, will be derived. This parameter will be presented as a representation of resistance to vapor flow between microposts.

First, we consider the balance in Equation 3.1 for the case of vapor flowing through a line of unit cells, as shown in Figure 3.10, where N is the number of unit cells in the radius. For this analysis, the droplet is assumed to be at maximum spread, and the number of unit cells considered can be expressed as $N = D_{max}/2w$, where D_{max} is the diameter of maximum spread. Wildeman et

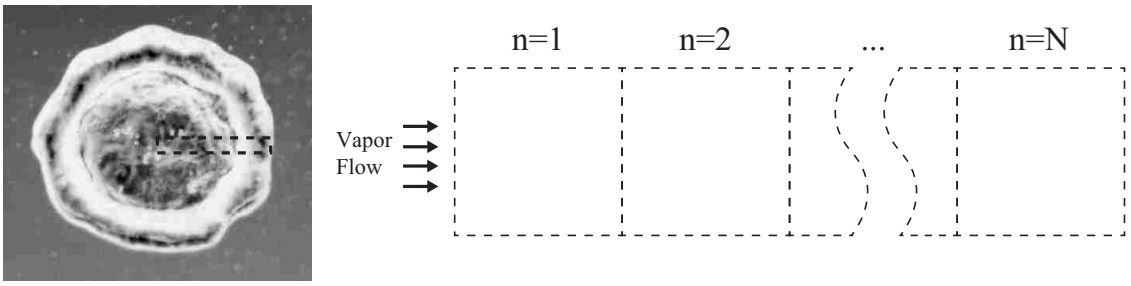

Figure 3.10: Left: top-down high-speed image of a droplet impinging a SH surface 2.7 ms after impact at $We = 40$ and $T_s = 220$ °C. Right: schematic of vapor flow through the unit cells contained in the radius of the droplet (indicated in the high-speed image by the dashed line), where N is the number of unit cells in the radius.

al. [45] derived the maximum spreading diameter for a free-slip case:

$$D_{max} = D_0 \sqrt{\frac{4}{1 - cos\theta_a} \left(\frac{We}{24} + 1 \right)} \tag{3.4}$$

where θ_a is the advancing contact angle. θ_a is nominally 160 ° for the surfaces considered in this study. Results from our experiments show that this expression for D_{max} matches within 4.5% of the maximum spreading diameter observed on each SH surface for the range of Weber numbers considered.

Although the radial nature of the problem causes spreading in the vapor flow, this effect is neglected, and vapor flow into the nth unit cell, $Q_{in,n}$ is taken to be total vapor flow through the previous unit cell, $Q_{uc,n-1}$. Vapor flow due to boiling, Q_{gen}, is assumed equal for each unit cell in the radius, and scales as:

$$Q_{gen} \sim \frac{q_d'' A_c}{h_{fg} \rho_{vap} h} \tag{3.5}$$

where q_d'' is heat flux to the spreading droplet, A_c is the interfacial contact area of the unit cell (taken to be $A_c = w^2$), h_{fg} is the latent heat of vaporization for water, and ρ_{vap} is the density of water vapor. The vapor is assumed to behave as an ideal gas, and ρ_{vap} is calculated as a function of surface temperature. Heat flux to the droplet is calculated as [19, 39]:

$$q_d''(t) = \frac{\sqrt{k_s \rho_s c_{p,s}} \Delta T_e}{\sqrt{\pi t}} \tag{3.6}$$

where k_s, ρ_s, and $c_{p,s}$ are the thermal conductivity, density, and specific heat (respectively) of the SH surface, $\Delta T_e = T_s - T_{sat}$ is the excess temperature, and t is the time after droplet impact. The droplet is assumed to be at maximum spread, and the time for which this occurs was found experimentally to be $t_{msd} \approx 2.7$ ms. Because the SH surfaces are composed of solid posts and air cavities, bulk surface properties are determined using the solid fraction following the approach of Guo et al. [39]: $k_s = k_{silicon} f_s + k_{air}(1 - f_s)$ and $\rho_s c_{p,s} = \rho_{silicon} c_{p,silicon} f_s + \rho_{air} c_{p,air}(1 - f_s)$. Values of the material properties for the surfaces considered here can be found in Table 3.2.

Because vapor generation is the same in each unit cell, vapor flow through the nth unit cell can be expressed as:

$$Q_{uc,n} = nQ_{gen} \tag{3.7}$$

Combining Equations 3.2 and 3.7, the pressure drop across the nth unit cell scales as:

$$\Delta P_{uc,n} \sim \frac{n\mu Q_{gen}}{w^2} f\left(d/w\right) \tag{3.8}$$

The total pressure drop, ΔP_{tot}, from the center to the edge of the droplet is then calculated by summing $\Delta P_{uc,n}$ along the radius:

$$\Delta P_{tot} \sim \frac{\mu Q_{gen}}{w^2} f\left(d/w\right) \sum_{n=1}^{N} n \tag{3.9}$$

or

$$\Delta P_{tot} \sim \frac{\mu Q_{gen}}{2w^2} f\left(d/w\right) \left(N^2 + N\right) \tag{3.10}$$

Note that for this scaling, the factor of $1/\sqrt{\pi}$ from Equation 3.6 is neglected because it is an unimportant scaling parameter.

Table 3.2: Properties of materials.

Property	Water	Silicon	Air
ρ (kg/m^3)	998	2329	1.29
c_p (J/kgK)	4200	700	1006
k (W/mK)	0.6	120	0.026

3.6.2 Results

Scaling results will be presented to show how resistance to vapor flow through the micro-post arrays (represented as pressure drop) varies with microstructure pitch, Weber number, and surface temperature. Results will then be compared to experimentally obtained atomization intensity to show the correlation between resistance to vapor flow and atomization. Scaled pressure drop will be presented as ΔP^*, total pressure drop from the center to the edge of the droplet normalized by the maximum value for all scenarios considered, occurring on the 8 μm pitch surface at $T_s = 320$ °C and $We = 200$.

Figure 3.11 demonstrates how ΔP^* varies with pitch for a constant solid fraction of $f_s = 0.15$. A surface temperature of 180 °C was chosen, as it was observed to be in the nucleate boiling regime for each of the SH surfaces considered experimentally. Figure 3.11 shows that as Weber number increases, ΔP^* increases, caused by an increase in maximum spread diameter of the droplet. As pitch increases, ΔP^* decreases. Significantly, ΔP^* decreases much more for an increase from 8 μm to 12 μm than an increase from 12 μm to 16 μm (see Figure 3.7). Correspondingly, experimental data show that a much higher maximum atomization intensity is observed on the 8 μm pitch surface than on the 12 μm or 16 μm pitch surfaces, supporting the hypothesis that atomization intensity decreases with decreasing resistance to vapor flow.

Figure 3.12 shows ΔP^* as a function of surface temperature for varying Weber number and pitch. Scaling results are shown for We =40, 85, 150, and 200 and for the 8 μm, 12 μm, and 16 μm pitch SH surfaces. Total pressure drop increases notably with surface temperature due to increasing vapor generation. Here, ΔP^* on the 8 μm pitch surface is nearly an order of magnitude greater than on the other surfaces. On the 12 μm and 16 μm pitch surfaces, ΔP^* exhibits much less variation with either varying pitch or Weber number. This same behavior is observed in experimental atomization intensity data. Note that while Figure 3.12 displays the entire range of experimental surface temperatures considered, the scaling will actually break down as the onset of transition boiling is reached for each surface. This threshold varies with Weber number, but is nominally 280 °C on the 8 μm pitch surface, and between 180 °C and 220 °C for the 12 μm and 16 μm pitch surfaces.

Figure 3.13 shows experimentally obtained atomization intensity, $A^*_{max,t}$, as a function of ΔP^*. Note that only scenarios that were determined to be in the nucleate boiling regime were

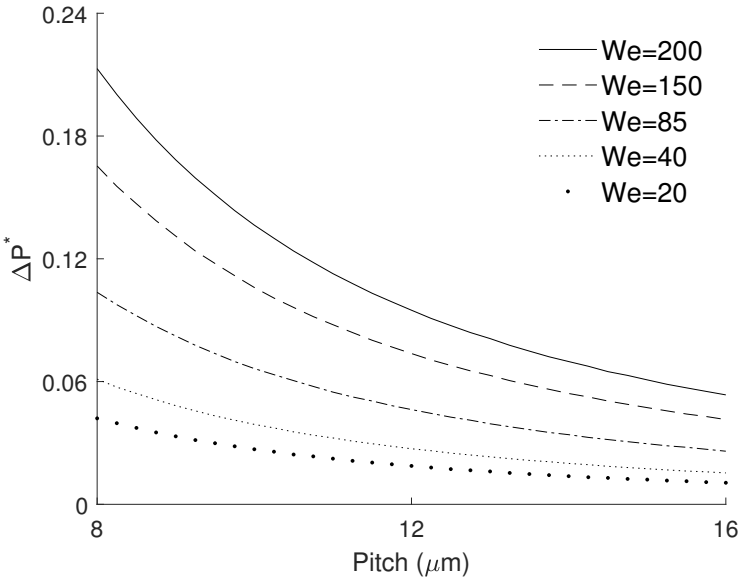

Figure 3.11: Normalized scaling of ΔP_{tot} as a function of pitch at varying Weber numbers, and at $T_s = 180$ °C and $f_s = 0.15$.

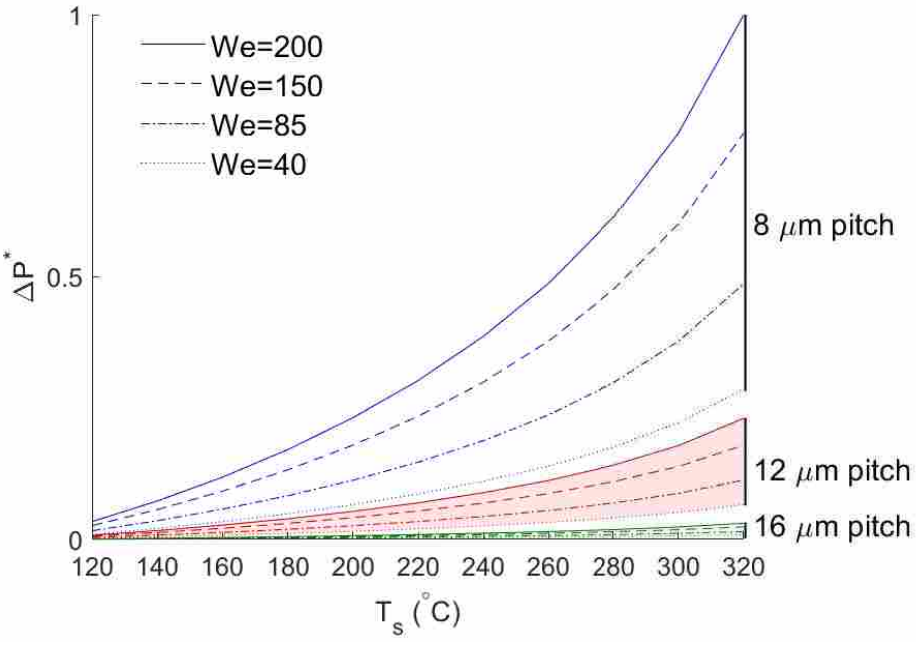

Figure 3.12: Normalized scaling of ΔP_{tot} as a function of surface temperature on each SH surface for Weber numbers of 40, 85, 150, and 200.

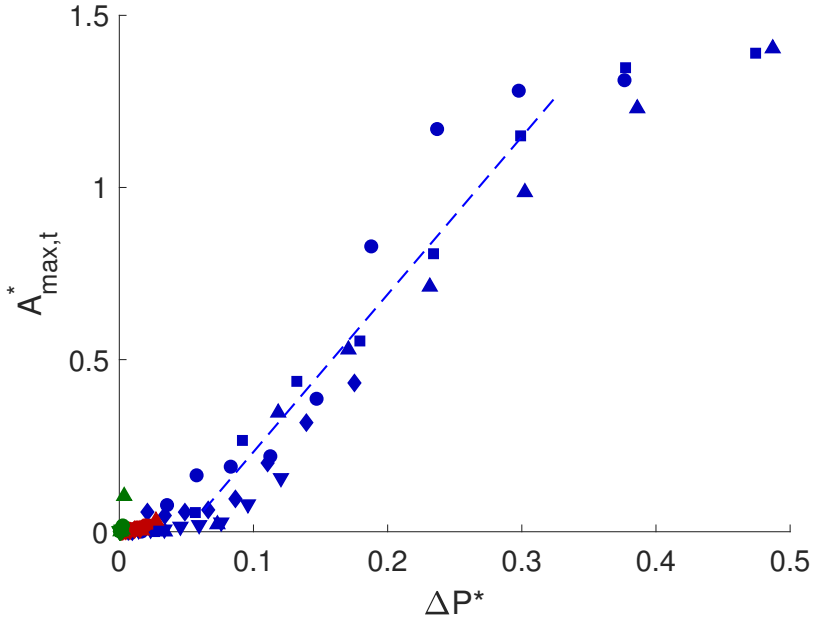

Figure 3.13: $A^*_{max,t}$ as a function of ΔP^* on all surfaces. Only scenarios in the nucleate boiling regime are plotted. Blue markers represent data on the 8 μm pitch surface, red represent the 12 μm pitch surface, and green represent the 16 μm pitch surface. Different Weber numbers are represented as different markers. Down-pointing triangles: $We = 20$, diamonds: $We = 40$, circles: $We = 85$, squares: $We = 150$, and up-pointing triangles: $We = 200$. Dashed line represents a loose fit to the 8 μm pitch surface data.

included in this plot, where the nucleate boiling regime was taken to be all temperatures up until and including the maximum atomization intensity for the temperature range. For each of the SH surfaces considered, $A^*_{max,t}$ is shown to be a strong function on ΔP^*, indicating that resistance to vapor flow through microstructures in a given scenario is a good predictor of thermal atomization intensity. Note that after $\Delta P^* \approx 0.3$, atomization intensity begins to level off somewhat. This indicates that as resistance to vapor flow increases, it approaches a point where vapor flow is no longer possible. If $A^*_{max,t}$ were obtained for values beyond this point, it would theoretically remain constant with increasing ΔP^*.

3.7 Conclusions

Thermal atomization intensity present during droplet impingement on superheated SmH and post-patterned SH surfaces was investigated for a range of microstructure pitches and Weber numbers. Atomization intensity in a given impingement scenario is tied to the boiling regime present. Atomization increases in the nucleate boiling regime and decreases during transition boiling until the LFP is reached, whereupon film boiling dominates and atomization is suppressed.

The rate of atomization generation, atomized particle velocity, and atomization start time were also investigated. Atomization generation rate and particle velocity both increase with Weber number for all the surfaces studied here, with the 8 μm pitch surface always exhibiting the highest values of each. Generation start time decreases as Weber number increases, and the 8 μm pitch surface was found to always have the earliest start times, which may also be attributed to its low microstructure pitch. The LFP was found to increase with increasing Weber number and decreasing pitch.

Atomization on the SmH surface increases with Weber number due to decreasing lamella thickness. Each of the SH surfaces follows the same trend, but the microstructure configuration on these surfaces significantly alters the amount of atomization generation compared with the SmH by enabling both droplet wetting and lateral vapor escape through the micropost arrays. The 8 μm pitch surface always exhibits the greatest quantity of atomization, presumably due to its low pitch, which allows intermittent wetting at high temperatures but restricts a large portion of vapor escape. However, at high Weber number, the 8 μm pitch and SmH surfaces exhibit almost identical atomization quantities, which supports findings by Pittoni [33] that wetting effects play less of a role at high Weber numbers. It was also found that on the SmH and 8 μm pitch surfaces, there appears to be a point at which increasing Weber number no longer affects the amount of atomization observed.

Both the 12 μm and 16 μm pitch surfaces exhibit very low quantities of atomization compared with the SmH and the 8 μm pitch because of their enhanced ability for vapor escape.

A scaling model was developed to explore the resistance to vapor flow through the SH micropost arrays, neglecting the effects of wetting and lamella thickness. The scaling indicates that resistance to vapor flow, expressed as ΔP^*, and consequently atomization intensity, should increase dramatically with decreasing pitch, and this is what experimental data shows. Trends with Weber

number and surface temperature were also confirmed. Atomization intensity was shown a strong function of ΔP^*, indicating that Weber number and surface temperature both play a significant role in resistance to vapor flow, and that resistance to vapor flow through microstructures is a good parameter in predicting thermal atomization generation during nucleate boiling.

CHAPTER 4. THERMAL ATOMIZATION INTENSITY DURING DROPLET IMPINGEMENT ON POST- AND HOLE-PATTERNED SUPERHYDROPHOBIC SURFACES

This chapter is in preparation for being submitted to the International Journal of Heat and Mass Transfer. The format has been been modified to meet the requirements of this thesis.

4.1 Contributing Authors and Affiliations

Preston Emerson, Julie Crockett, Daniel Maynes Department of Mechanical Engineering, Brigham Young University, Provo, Utah 84602

4.2 Abstract

Thermal atomization during droplet impingement on SH surfaces with two distinct microstructure configurations is considered: square posts and square holes. Tests are done for each configuration with structure heights of 4 μm, 8 μm, and 12 μm. Surface temperature varies between 120 °C and 250 °C and Weber numbers of 40, 85, 150, and 240 are considered. Structure spacing and solid fraction are held constant. Comparing the two configurations at each structure height and Weber number, atomization intensity is generally roughly equal or higher on the hole-patterned surface. Some exceptions exist, and reasoning behind this is discussed. Microstructure height significantly affects trends in atomization intensity with surface temperature and Weber number. The LFP is seen to decrease with increasing height.

4.3 Introduction

Superhydrophobic (SH) surfaces are characterized by their highly water-repellent nature, which leads to an array of unique fluid and thermal qualities including drag reduction, self-cleaning, and thermal insulation. The most important feature of SH surfaces is surface roughness on the micro- or nanoscale. It is this feature that produces superhydrophobicity by the presence of the

Cassie-Baxter state. A water droplet sitting on a microstructured surface is depicted in Figure 4.1. Liquid is said to be in the Cassie-Baxter state when it rests on top of the structures without penetrating the air cavities beneath, as shown in Figure 4.1a. When liquid penetrates the air cavities, as in Figure 4.1b, it is in the Wenzel state. This state is also referred to as wetting.

If surface cavities are small enough (generally on the nanoscale) capillary forces alone are often sufficient to prevent liquid penetration and create superhydrophobicity. However, many SH surfaces are fabricated with structures on the microscale, assisted by a hydrophobic coating to promote the Cassie state. The wettability of a surface, or the degree to which it is hydrophilic or hydrophobic, is quantified using droplet contact angle, θ, as seen in Figure 4.1a, where high contact angle indicates greater hydrophobicity and low contact angle indicates greater hydrophilicity. Surfaces with contact angles above 90 $^\circ$ are considered hydrophobic. To be considered superhydrophobic, contact angles must exceed around 120 $^\circ$. The contact angle θ is called the sessile (or static) contact angle. Dynamic contact angles can also be measured for a droplet impacting a surface (advancing angle) and rebounding from the surface (receding angle).

The current study is concerned with water droplets impinging SH surfaces at temperatures above the liquid saturation point. Consider first a smooth surface. As a droplet impacts, it begins to boil and vapor generation occurs. The classic boiling regimes—convective, nucleate, transition, and film—are observed. Boiling dynamics greatly affect droplet morphology. During nucleate boiling, vapor bubbles are rapidly generated in the lamella of the spreading droplet. These bubbles burst upwards, sending out a fine spray of liquid particles known as thermal atomization. The intensity of thermal atomization found in a given scenario increases with surface temperature, as more and more nucleation sites develop. As surface temperature increases further, transition boiling occurs, where bubbles grow in size and coalesce with one another. Atomization intensity decreases in this regime due to the insulating effect of the large bubbles at the liquid-solid interface. At some surface temperature, labeled the Leidenfrost point (LFP), heat flux to the droplet is so great that a stable vapor film is formed almost immediately upon impact, which insulates the droplet and suppresses thermal atomization altogether. This marks the onset of film boiling.

The effect of SH surface microstructure on both hydrodynamic and thermodynamic behavior has been widely studied [2,8,20,33,34,39,40]. Structures can be random or deliberately placed. Deliberate, organized structures such as ribs, posts, and holes are commonly etched into a surface

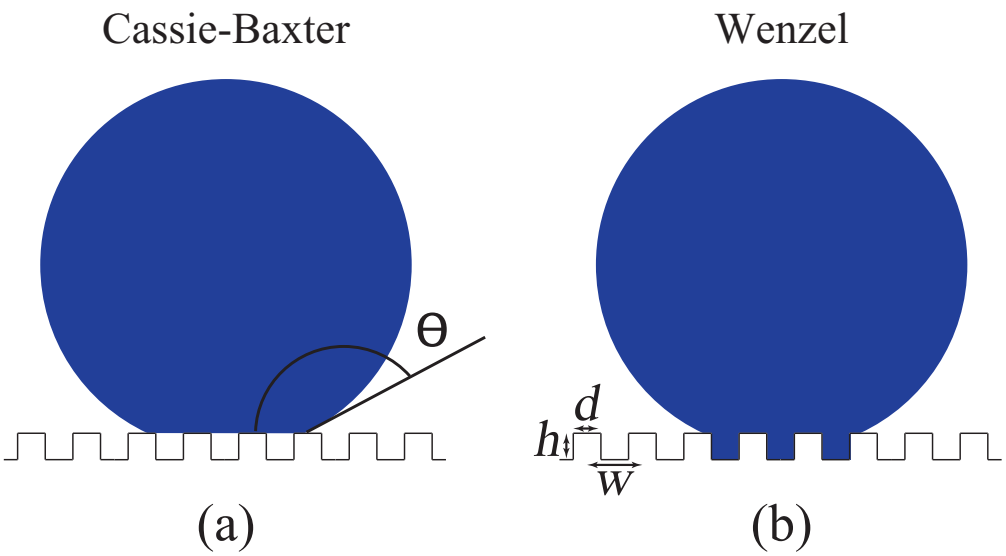

Figure 4.1: A droplet resting on a microstructured SH surface in the (a) Cassie-Baxter state and (b) Wenzel state.

so that parameters such as structure height, h, width, d, and pitch (center-to-center spacing), w, can be controlled. Solid fraction, f_s, is the area of the top of structures divided by the total projected surface area and has proven to be an important parameter governing behavior. In general, as solid fraction decreases, contact angle increases. Pittoni et al. [33] showed that for impinging droplets, increasing advancing contact angle decreases the effect of droplet wetting. Zhang et al. [2] did extensive experimentation of impinging droplets and documented six impact modes which can be specifically manipulated by changing microstructure. Clavijo et al. [20] established that varying pitch of post-patterned SH surfaces significantly alters thermal atomization intensity during droplet impingement.

In Chapter 3 of this thesis, it was established that thermal atomization intensity on post-patterned surfaces is influence by three important factors: droplet lamella thickness, droplet wetting, and vapor escape. Lamella thickness was found to be dependent on Weber number, defined as $We = \rho V_0^2 D_0/\sigma$, where ρ and σ are droplet density and surface tension, respectively, and V_0 and D_0 are droplet impact velocity and initial diameter. A thinner lamella is seen to allow for more atomization. Droplet wetting increases liquid-solid contact, which in turn increases heat transfer to the droplet. Droplet wetting also promotes atomization. Vapor escape occurs when vapor (generated during boiling) flows laterally through microstructures. This reduces the amount of vapor that

bursts through the lamella and suppresses atomization. It was found that a complicated relationship exists between droplet wetting and vapor escape.

In this chapter, two specific surface microstructures will be explored: square posts and square holes. Solid fraction and spacing between structures, s, are held constant. Structure heights of 4 μm, 8 μm, and 12 μm are considered. The post surfaces allow for vapor escape, while the hole surfaces are meant to restrict it completely. Droplet wetting is also affected by these microstructure configurations, where the restriction of vapor escape on the hole surfaces causes more resistance to wetting on these surfaces as well. Thermal atomization intensity on each of these surfaces is compared for surface temperatures ranging from 120 °C to 250 °C and Weber numbers of 40, 85, 150, and 240. It is shown that post- and hole-patterned surfaces do indeed exhibit vastly different trends in atomization intensity, and that these trends are significantly altered by varying structure height. These findings contribute to the understanding of how altering SH microstructure configuration can be used to affect droplet morphology and atomization intensity in superheated droplet impingement scenarios.

4.4 Methodology

This section briefly outlines the fabrication process for the post- and hole-patterned SH surfaces used for this study, the droplet impact experimental setup, and the image processing technique used to evaluate thermal atomization intensity.

Scanning electron microscope (SEM) images showing the surface microstructure of the SH surfaces used in this study can be seen in Figure 4.2. Definitions of structure height, h, spacing, s, and length, d is shown for each surface. Photolithography is used to deposit photoresist on a smooth silicon wafer. The photoresist is exposed through a photomask and developed, leaving a pattern on the wafer. The wafer is then etched via ion etcher to the desired structure height. A layer of chromium (nominal thickness of 100 nm) deposited on the surface is necessary for adhesion of Teflon, which is used as a hydrophobic coating. The Teflon is spin coated with a nominal thickness of 200 nm. Solid fraction is held constant at 0.30 $\pm$0.03 for all surfaces. Spacing is nominally 20 μm $\pm$1%, and structure heights of 4 μm, 8 μm, and 12 mum $\pm$10% are used. Sessile contact angles of the SH surfaces are $150^\circ \pm 3^\circ$. Advancing angles are nominally $160^\circ \pm 3^\circ$ with hysteresis

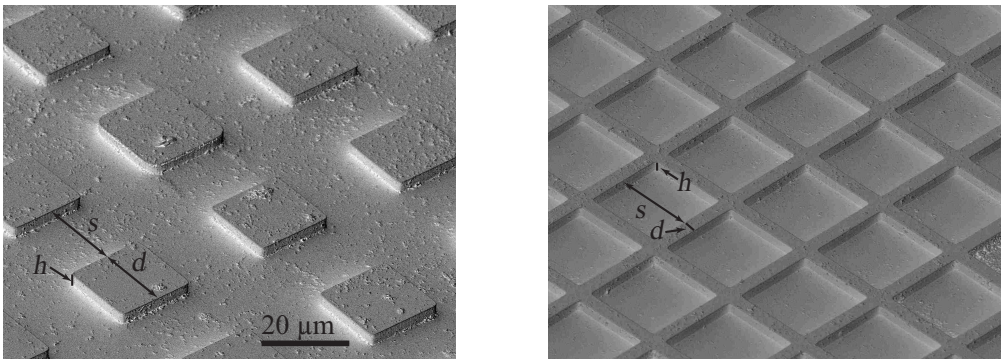

(a) (b)

Figure 4.2: SEM images of the (a) post-patterned and (b) hole-patterned surfaces with structure height of 4 μm.

of about 8°. A smooth hydrophobic (SmH) surface with a sessile contact angle of $115° \pm 3°$ was also fabricated by coating a plain silicon wafer with Teflon.

A schematic of the experimental setup is shown in Figure 4.3. Water droplets of nearly constant diameter, $D_0 = 2.3 \pm .024$ mm, are dispensed from a syringe whose height can be adjusted to vary Weber number. The silicon substrate sits atop an aluminum heating block, heated with cartridge heaters and kept at constant temperature using a SOLO 9696 temperature controller with K-type thermocouple. Impingement events are captured as grayscale TIFF images at 3000 fps using a Photron APX RS Fastcam. A halogen lamp is positioned behind the droplet, and light is diffused through sand-blasted glass, producing a uniform background. Spatial resolution for all scenarios is nominally 12 μm/pixel $\pm$ 0.2 %. Weber number uncertainty ranges from $\pm$2.6 for $We = 40$ to $\pm$6.7 for $We = 240$ and surface temperature uncertainty is $\pm$3 %. The temperature range is restricted by the Teflon, which degrades at temperatures above about 340 °C. Between 15 and 30 trials are captured at each temperature, from which average results are calculated.

High-speed images were analyzed for thermal atomization intensity using MATLAB. The image processing technique is sensitive to environmental variables in the experimentation stage, the most important of which are background lighting and spatial resolution. Impingement events are saved beginning with the frame just before the droplet enters the field of view and given sufficient time after impact to allow for all atomization behavior to be observed.

The current frame to be analyzed is cropped to have a field of view of about 10.2 $\times$ 10.2 mm with the droplet centered horizontally. The absolute value of the current frame minus the

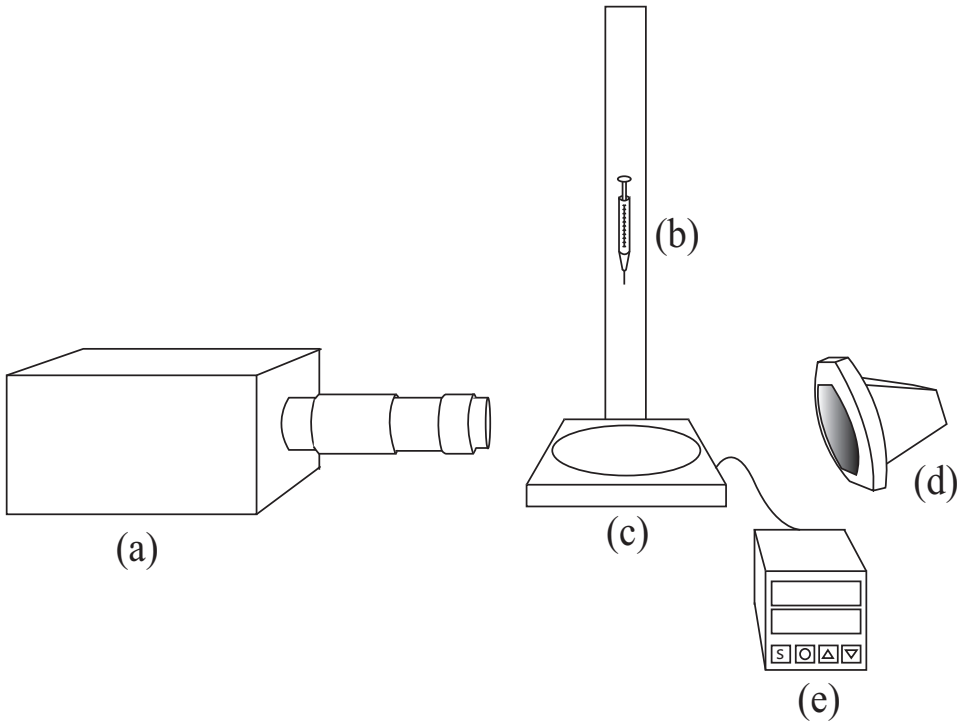

Figure 4.3: Schematic of the experimental setup consisting of (a) high-speed camera (b) needle to dispense water droplets (c) heating block with cartridge heaters (d) halogen backlight (e) temperature controller with thermocouple.

plain background image is taken to reduce noise. The total intensity of in-plane atomization in the frame is found by summing the values of pixels in the differenced frame that contain atomization. Because of the three-dimensional nature of the atomization spray, some atomized particles appear more in-focus (and thus darker) in the original frame. The pixels associated with these particles hold higher value in the differenced frame, so they are weighted more heavily in the final atomization intensity calculation.

4.5 Results and Discussion

It is useful to compare thermal atomization intensity for the post and hole SH surfaces studied here to atomization occurring on a SmH surface. Figure 4.4 shows a droplet impinging a SmH surface compared with droplets impinging 4 μm height post- and hole-structured SH surfaces at $We = 85$ and $t = 3$ ms. Respective temperatures were chosen to show maximum atomization on each surface: 220 °C for SmH, 160 °C for posts, and 140 °C for holes. Thermal atomization

Figure 4.4: Atomization intensity on the SmH, 4 μm height post, and 4 μm hole surfaces at $We = 85$ and $t = 3$ ms. Temperature was chosen for each surface to show maximum atomization: 220 °C for SmH, 160 °C for post, and 140 °C for hole.

intensity for the SH surfaces in this study is less than 5% of that found on the SmH surface, consistent with findings that decreasing surface solid fraction decreases heat transfer to the liquid and suppresses atomization [8, 20]. For the purposes of this study, atomization intensity will be scaled between zero and one by normalizing by the maximum atomization intensity occurring on the SH surfaces for the scenarios considered. This maximum value occurs on the 4 μm height post surface at $T_s = 180$ °C and $We = 240$.

Figure 4.5 shows the temporal progression of an impinging droplet on the 8 μm height hole surface for the range of Weber numbers. Surface temperatures correspond to maximum atomization and are 150 °C for $We = 40$, 190 °C for $We = 85$, 160 °C for $We = 150$, and 180 °C for $We = 240$. Time is measured beginning with initial droplet impact. As the droplet spreads, the lamella becomes thinner and vapor bubbles burst through, generating thermal atomization. Atomized particles travel radially in all directions from the source of generation. For all Weber numbers except the highest, the droplet begins to retract. At $We = 240$, droplet breakup occurs and by $t = 6$ ms, the droplet begins to levitate above the surface. Atomization generation appears to cease prior to about 4 ms as atomization is no longer observed near the droplet at this time.

Additionally, Figure 4.6 displays the trend of atomization intensity with surface temperature for a droplet impinging the 8 μm height hole surface at $We = 85$ and $t = 3$ ms for a range of surface temperatures. As surface temperature increases in the nucleate boiling regime (here, from 150 °C to 190 °C), atomization intensity increases. After $T_s = 190$ °C, the droplet transitions to

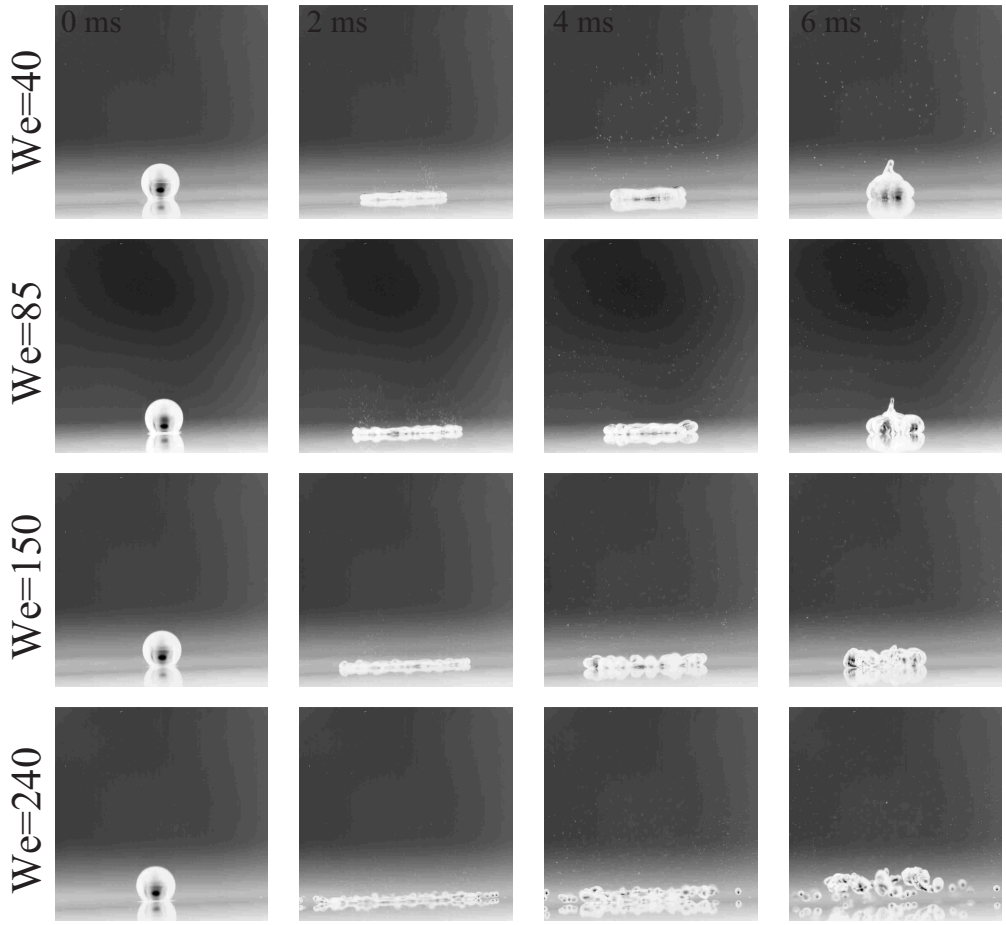

Figure 4.5: Droplet impinging the 8 μm height hole surface for the range of Weber numbers. Surface temperature was chosen to be for maximum atomization and is 150 °C for $We = 40$, 190 °C for $We = 85$, 160 °C for $We = 150$, and 180 °C for $We = 240$.

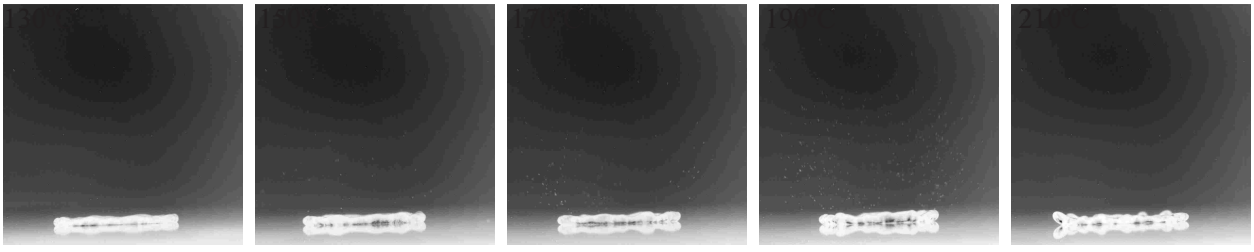

Figure 4.6: Atomization intensity for a range of surface temperatures on the 8 μm height hole surface at $We = 85$ and $t = 3$ ms.

film boiling, and atomization is suppressed. For this scenario, the LFP occurs at around 210 °C. The trend of atomization intensity with surface temperature is discussed in greater depth below.

Atomization intensity through time is shown in Figure 4.7 for the 4 μm height post and hole surfaces at each Weber number. Surface temperature is chosen such that intensity on each surface is roughly equal; 160 °C for $We = 40$, 180 °C for $We = 85$, 160 °C for $We = 150$, and for $We = 240$ is 200 °C for posts and 160 °C for holes. Note that since surface temperature varies for each scenario, trends in atomization with varying Weber number cannot be judged from these plots. The scales are adjusted for each plot to best show temporal trends. It can be seen that atomization intensity increases with time as thermally atomized particles are generated. At some time after impact, atomization intensity reaches a maximum value, $A^*_{max,t}$, and begins to decrease. The time for which this occurs, t_{max}, marks the point when atomized particles begin exiting the field of view. The exact time for which atomization generation ceases cannot be determined from these experiments. However, it appears from high-speed images that for most scenarios, atomization generation ceases before particles begin exiting the field of view. The relative rates for which atomization is generated and leaves the field of view are reflected in the initial and final slopes of the time curve, respectively.

It can be seen from Figure 4.7 that the onset of atomization generation occurs a little after 2 ms at $We = 40$ and decreases slightly with increasing Weber number. This trend is constant for the range of structure heights considered, and in general, experiments show that atomization begins slightly earlier on the hole surfaces than on the posts. The fact that onset of atomization is delayed on posts compared to holes is likely due to the ability for vapor escape through the posts. Upon impact, heat transfer is initially small and increases as the droplet spreads due to increasing liquid-solid contact. On the post surfaces, any vapor that is formed escapes through the microstructures until heat transfer is great enough to overcome this effect. On the hole surfaces, vapor may not escape, and it remains in the lamella as bubbles, which eventually burst through.

The initial slope of the time curve is about the same for both posts and holes, but the final slope is consistently steeper on the hole surfaces, indicating faster traveling particles leaving the field of view. Figure 4.8 plots peak atomization time, t_{max}, with Weber number for each SH surface. Again, surface temperatures were chosen to correspond with the maximum atomizing case in each scenario. As Weber number increases, t_{max} decreases, from around 6 ms to 3 ms, for each surface.

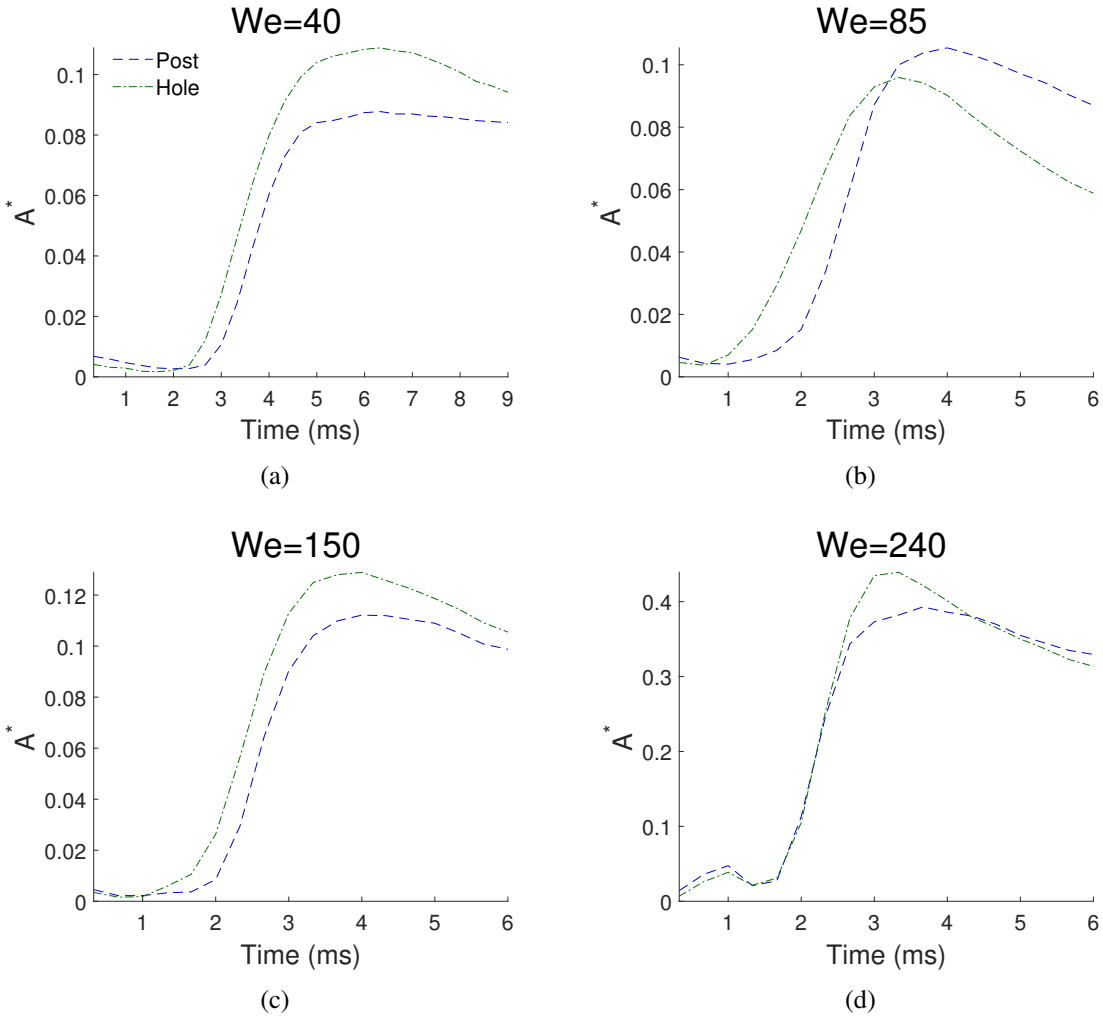

Figure 4.7: Atomization intensity plotted with time for the 4 μm height post and hole surfaces at (a) $We = 40$, $T_s = 160$ °C (b) $We = 85$, $T_s = 180$ °C (c) $We = 150$, $T_s = 160$ °C and (d) $We = 240$, $T_s = 200$ °C for posts, $T_s = 160$ °C for holes. Temperature is chosen at each Weber number such that atomization intensity is similar on both surfaces; note that for $We = 240$, temperature is different for posts and holes. Atomization intensity scale is adjusted for each plot to show all trends.

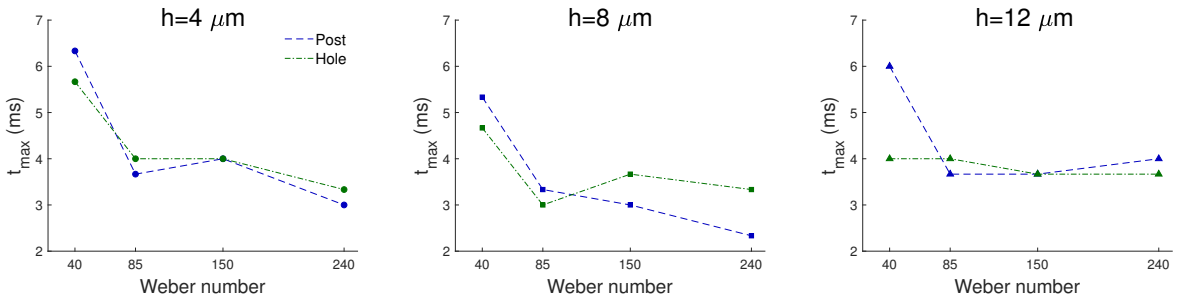

Figure 4.8: Time for maximum atomization plotted with Weber number on the 4 μm, 8 μm, and 12 μm height post and hole surfaces. Surface temperature was chosen to be for the maximum atomizing case on each surface and at each Weber number.

This suggests that initial particle velocity increases with Weber number. Additionally, for the post surfaces, peak atomization time remains roughly constant with varying structure height for all Weber numbers considered. This is also the case for holes at high Weber numbers. However, at $We = 40$, peak atomization time decreases from 5.7 ms for a height of 4 μm to 4 ms for a height of 12 μm. This suggests that at low Weber number, initial particle velocity increases with increasing hole depth. The reasons for this are not entirely known, but may be connected to the reaction force of the air trapped in the holes upon impingement.

Figure 4.9 displays atomization intensity with surface temperature on post and hole structures for the entire range of microstructure heights (increasing left to right) and Weber numbers (increasing top to bottom). First considering only the 4 μm height surfaces (left column in Figure 4.9), atomization intensity follows the same trend seen in Figure 4.6. It can be seen that atomization intensity initially increases with surface temperature. This marks the nucleate boiling regime. Intensity reaches a maximum value and begins to decrease during transition boiling until the LFP is reached, where film boiling dominates, and atomization is suppressed. In general, both post and hole surfaces have a LFP between 180 °C and 220 °C, compared to 320 °C on the SmH. Maximum atomization intensity increases with Weber number on both surfaces, consistent with results in Chapter 3. This is attributed mainly to the fact that the droplet lamella thins as Weber number increases, allowing a greater number of vapor bubbles to burst through. For each case except at the highest Weber number, a smaller atomization intensity is seen on the post surface. It is hypothesized that the ability for vapor escape through the microposts suppresses atomization by limiting the amount of vapor that penetrates the lamella. Vapor escape is restricted on the hole

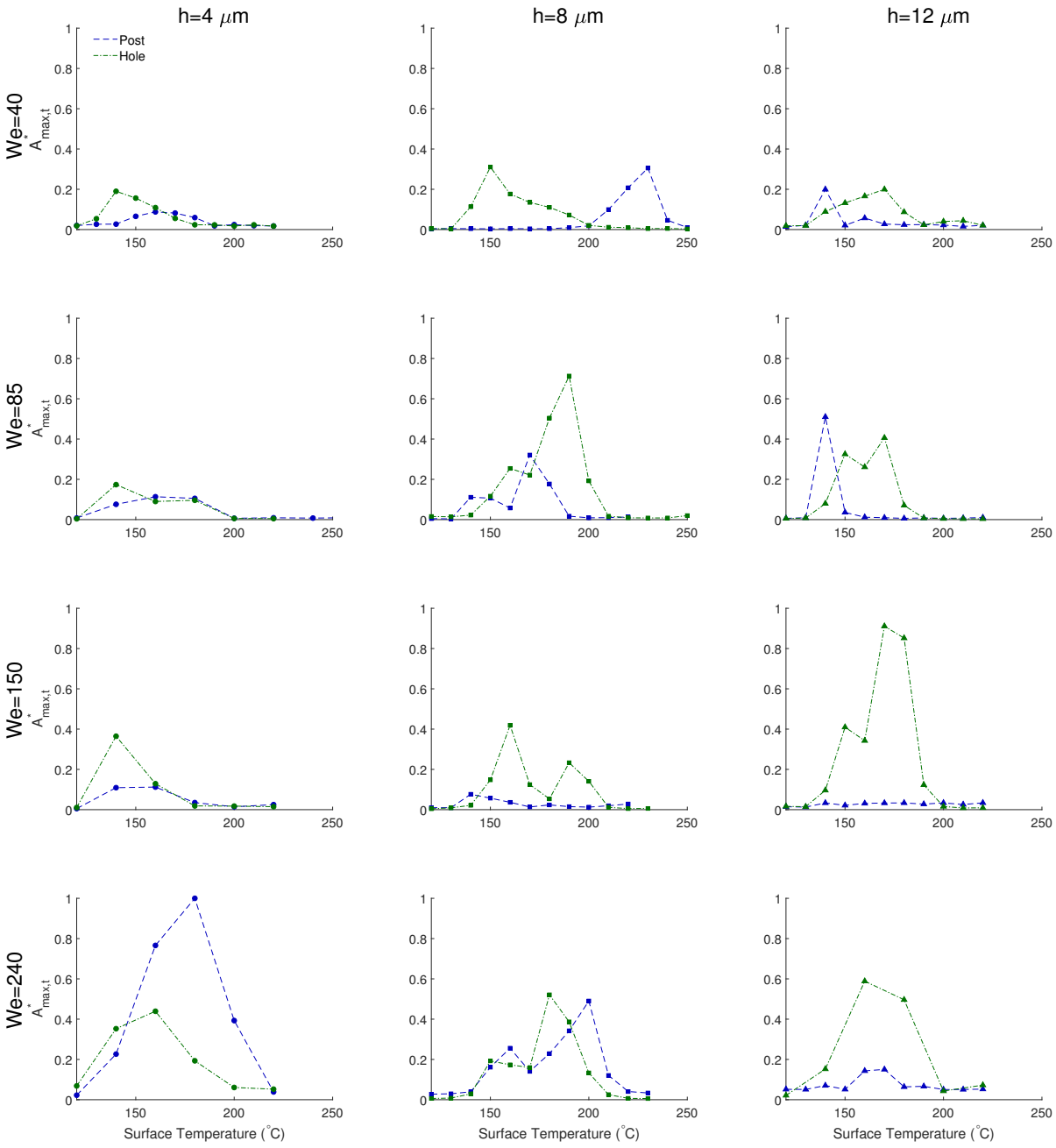

Figure 4.9: $A^*_{max,t}$ plotted with temperature for post and hole structures and for the range of structure heights (increasing left to right) and Weber numbers (increasing top to bottom).

surface, as the structures do not provide an escape path. At $We = 240$, the posts exhibit much more atomization than the holes, which may be caused by the ability for wetting on this surface, which increases liquid-solid contact and allows for more vapor generation. Wetting also restricts vapor escape locally. Conversely, the hole surface limits wetting, as trapped air in the holes restricts liquid penetration.

Interestingly, for the 4 μm height surfaces, the surface temperature corresponding to maximum atomization is consistently higher on the post surface than on the holes. One possible explanation for this is intermittent wetting, which has been found to occur during transition boiling on post-patterned surfaces [38]. As vapor bubbles in the spreading droplet grow larger and begin to coalesce, vapor escape through the posts prevents a stable film from forming and allows intermittent liquid-solid contact with the posts. This behavior could prolong the nucleate and transition boiling regimes in the droplet, causing atomization to peak at a higher temperature.

The trends for the 4 μm height surfaces are in many cases significantly altered on surfaces with taller microstructures. The LFP for the deeper hole structures remains between 180 °C and 220 °C for the range of Weber numbers but varies significantly for the taller posts. For the 8 μm height posts, the range of temperatures for which atomization is visible is somewhat unpredictable, and the LFP occurs anywhere between 180 °C and 250 °C. However, for the 12 μm height posts, the LFP is much lower, about 150 °C for all cases except at $We = 240$, where it is 180 °C. Thus, variations in LFP with structure height is insignificant for hole-patterned surfaces, while for post-patterned surfaces, LFP generally seems to decrease with increasing height. This is supported by the findings of Tran et al. [27] for post-patterned hydrophilic surfaces, who found LFP to decrease for circular posts of increasing height. This behavior was shown to be largely attributed to droplet wetting. As post height increases, increased liquid-solid contact due to wetting causes greater heat transfer, which in turn supports film boiling at lower surface temperatures. While the hydrophobic coating used in the current study promotes the Cassie-Baxter state (as opposed to the dominating Wenzel state in the scenarios considered by Tran), liquid penetration still occurs on the SH surfaces at early impact times due to the water hammer and dynamic pressures [30, 33], increasing liquid-solid contact.

Thermal atomization intensity increases slightly with structure height for the hole surfaces, whereas for the posts, atomization behavior is more dependent on Weber number. At $We = 40$

and $We = 85$, maximum atomization intensity is larger for 8 μm and 12 μm height posts than for 4 μm height posts. However, the range of temperatures for which atomization is present shrinks with increasing structure height. At $We = 150$ and $We = 240$, atomization intensity decreases with increasing post height. Here, there is a balance between vapor escape and droplet wetting, which was discussed extensively in Chapter 3. As post height increases, the channels for vapor escape grow larger, and suppression of atomization would be expected. However, taller structures also provide more potential for liquid-solid contact in the form of droplet wetting. It has also been shown that dewetting rates increase with post height, surface temperature, and Weber number [33,34]. For Weber numbers between 85 and 150, a transition occurs, below which droplet wetting dominates, causing greater atomization intensity with taller post height. Above this transition Weber number, vapor escape dominates, causing greater suppression of atomization for taller posts.

As for variations in atomization intensity with Weber number, for the 8 μm and 12 μm hole surfaces, intensity is lowest at $We = 40$ but fluctuates at higher Weber numbers with no specific trend. Atomization on the taller post surfaces changes little from $We = 40$ to $We = 85$, but at $We = 150$, seems to be almost completely suppressed for the entire range of surface temperatures. At $We = 240$, atomization intensity increases again, though less so for the 12 μm height posts. Taller posts promote the suppression of atomization for Weber numbers between 85 and 240, but allow atomization above this range. For the 8 μm and 12 μm height structures, atomization intensity at each Weber number is generally either the same or greater on the holes than posts. Additionally, the taller structure surfaces are more likely to have a much wider gap between atomization intensities on the hole and post surfaces than the 4 μm height surfaces. This is attributed to the ability of post surfaces to suppress atomization through vapor escape, an ability which is enhanced with taller posts.

Surface temperature corresponding to maximum atomization shifts with structure height for both hole- and post-structured surfaces. For hole surfaces, as height increases, maximum atomizing temperature increases, though the range of surface temperatures for which atomization is observed, from about 130 °C to 200 °C, is unchanged. For the 8 μm height post surface, the range for atomization varies randomly with Weber number, with the maximum atomizing temperature sometimes above the holes and sometimes below. For the 12 μm height posts, peak atomization temperature is low, from 140 °C to 160 °C, since the LFP occurs at such a low temperature.

4.6 Conclusions

Thermal atomization during droplet impingement on post- and hole-patterned SH surfaces with structure heights of 4 μm, 8μm, and 12 μm was investigated for a range of Weber numbers and surface temperatures. Solid fraction and structure spacing were held constant for each surface. In general, the post-patterned surfaces exhibit lower atomization intensities than the holes, supporting the conclusion that atomization can be suppressed by allowing vapor escape through microstructures.

For the 4 μm height structures, atomization intensity increases with Weber number, but this trend is much less straightforward for the 8 μm and 12 μm heights. Structure height was not found to significantly affect the LFP on hole surfaces, but for post surfaces, LFP decreases with increasing height, presumably due to intermittent wetting. For hole surfaces, the temperature corresponding to maximum atomization shifts slightly higher as structure height increases; for posts, the opposite trend is seen.

Several hydrodynamic mechanisms were used to explain these trends, including total droplet wetting (presence of the Wenzel state), intermittent wetting, and vapor escape. Wetting influences dynamics on hole surfaces less than posts because air trapped in the holes restricts this mechanism. Holes also prevent vapor escape, so atomization intensity on these surfaces is mainly a function of Weber number (lamella thickness) and surface temperature. Wetting and vapor escape are both possible on post surfaces, and these effects are often in competition with one another. As post height increases, vapor escape appears to dominate over wetting in most scenarios causing the suppression of atomization.

CHAPTER 5. CONCLUSIONS

Superhydrophobic surfaces show promise in various practical applications. The work contained in this thesis has been concerned with morphology and heat transfer of droplets impinging superheated SH surfaces. Specifically, trends in thermal atomization intensity were quantified for different impingement scenarios, and this work has contributed to the body of research by beginning to describe exactly how thermal atomization intensity can be manipulated by adjusting SH surface microstructure. A variety of microstructure configurations were considered, as well as a range of surface temperatures and Weber numbers. Each of these parameters was shown to have significant impact on thermal atomization intensity. This chapter summarizes the conclusions of this work and briefly outlines possible future related work.

5.1 Effect of Weber Number and Microstructure Pitch on Thermal Atomization for Post-patterned SH Surfaces

Thermal atomization intensity during droplet impingement was investigated for a SmH and three post-patterned SH surfaces with microstructure pitches of 8 μm, 12 μm, and 16 μm. Atomization intensity in a given impingement scenario is shown to be tied to the droplet boiling regime. Atomization increases in the nucleate boiling regime and decreases during transition boiling until the LFP is reached, whereupon film boiling dominates and atomization is suppressed.

Atomization intensity on the SmH surface increases with Weber number due to decreasing lamella thickness. Each of the SH surfaces follows the same trend, but the microstructure configuration on these surfaces significantly alters the amount of atomization generation compared with the SmH by enabling both droplet wetting and lateral vapor escape through the micropost arrays. Findings by Clavijo et al. [20] that atomization increases with decreasing pitch for SH surfaces was generally confirmed. However, it was found that at some Weber numbers, the 16 μm pitch

surface exhibits more atomization than the 12 μm pitch. This is likely due to a complex balance between droplet wetting and vapor escape, both of which increase with increasing pitch.

The 8 μm pitch surface always exhibits the greatest quantity of atomization, presumably due to its low pitch, which allows intermittent wetting at high temperatures but restricts a large portion of vapor escape. However, at high Weber number, the 8 μm pitch and SmH surfaces exhibit almost identical atomization quantities, which supports findings by Pittoni [33] that wetting effects play less of a role at high Weber numbers. It was also found that on the SmH and 8 μm pitch surfaces, there appears to be some point at which increasing Weber number no longer affects the amount of atomization observed. Both 12 μm and 16 μm pitch surfaces exhibit very low quantities of atomization compared with the SmH and the 8 μm pitch because of the greater space available for vapor escape.

Atomization generation rate, atomized particle velocity, and onset time for atomization generation were also investigated. Atomization generation rate and particle velocity both increase with Weber number for all the surfaces studied, with the 8 μm pitch surface always exhibiting the highest values of each. Atomization generation onset time decreases as Weber number increases, and the 8 μm pitch surface was found to always have the earliest onset times, which may also be attributed to its low microstructure pitch. The temperature for which atomization ceases is deemed the LFP, and it was found to increase with increasing Weber number and decreasing pitch.

A scaling model was developed to account for resistance to vapor flow through the SH micropost arrays. Existing models were used to estimate trends in pressure drop through post arrays, ΔP_{tot}. Effects of wetting and lamella thickness were neglected. Scaling model results indicate that resistance to vapor flow, ΔP_{tot}, and consequently atomization intensity, should increase dramatically with decreasing pitch, and this is, in fact, what experimental data shows. It was shown that when experimental data is plotted against the scaled pressure drop in the nucleate boiling regime, atomization intensity collapses loosely onto one line. This indicates that ΔP_{tot} is a good parameter in predicting thermal atomization generation during nucleate boiling.

5.2 Effect of Microstructure Pattern and Height on Thermal Atomization: Post- and Hole-patterned SH surfaces

Thermal atomization during droplet impingement on post- and hole-patterned SH surfaces with structure heights of 4 μm, 8μm, and 12 μm was investigated for a range of Weber numbers and surface temperatures (above the saturation point). Solid fraction and structure spacing were held constant for each surface. Post-patterned surfaces are constructed with square posts, leaving channels in between. These channels allow vapor (which is generated by boiling) to escape laterally beneath the droplet rather than be forced through the droplet lamella. Hole-patterned surfaces are constructed of square holes. Hole walls restrict vapor escape and trap air upon droplet impact.

In general, post-patterned surfaces exhibit lower atomization intensities than holes, supporting the conclusion that atomization can be suppressed by allowing vapor escape between microstructures. This effect is more pronounced for taller structures, as increasing post height allows for more vapor escape. Holes prevent vapor escape, so atomization intensity on these surfaces is more a function of Weber number (lamella thickness) and surface temperature than structure height. However, atomization intensity on the holes is slightly larger for 12 μ height structures than for the other heights.

For the 4 μm height structures, atomization intensity increases with Weber number, but this trend is much less straightforward for the 8 μm and 12 μm heights. Structure height was not found to significantly affect the LFP on hole surfaces. However, for post surfaces, LFP decreases with increasing height, presumably due to intermittent wetting. For hole surfaces, the temperature corresponding to maximum atomization shifts slightly higher as structure height increases; for posts, the opposite trend is seen. The reasons for this merit further investigation.

Several hydrodynamic mechanisms were used to explain these trends, including total droplet wetting (presence of the Wenzel state), intermittent wetting, and vapor escape. Wetting influences dynamics on hole surfaces less than posts because air trapped in the holes restricts this mechanism. Wetting and vapor escape are both possible on post surfaces, and these effects are often in competition with one another. As post height increases, vapor escape appears to dominate over wetting in most scenarios causing the suppression of atomization.

5.3 Suggested Future Work

Results contained in this thesis represent an important addition to the body of research relating to heat transfer on SH surfaces. Further work supporting the study of circular post-patterned SH surfaces could consist of more structure pitches between 8 μm and 12 μm. This would provide further insight into atomization mechanisms, since the difference in atomization intensity at these two pitch values is very large.

Regarding the square post- and hole-patterned surfaces, a relatively small solid fraction ($f_s = 0.3$) and large spacing between structures ($s = 20$ μm) were used. These parameters resulted in relatively low atomization intensity on both post and hole surfaces compared to a SmH surface. Increasing solid fraction and decreasing pitch would be beneficial, because it would allow for results to be repeated with higher maximum atomization intensities.

Weber number was varied in this work by varying initial droplet height. Varying Weber number by using liquids of different surface tension would represent additional realistic scenarios and alter results. Droplet impingement on inclined surfaces has been studied, but thermal atomization in these scenarios has yet to be recorded. Additionally, all of the work here focused on single droplet impingement. Recording thermal atomization of two impinging droplets side-by-side may give insight into droplet interactions in sprays on heated surfaces.

Finally, the contribution of this work may be enhanced by quantifying the heat flux associated with the specific scenarios studied. This may be done using a heat flux sensor or some other method to record the precise amount of heat removed from the surface during impingement. This would aide understanding of the relationship between droplet morphology and heat removal and support efforts to create a more complete vaporization model to enhance the scaling model accomplished here.

REFERENCES

[1] Bertola, V., 2015. "An impact regime map for water drops impacting on heated surfaces." *International Journal of Heat and Mass Transfer,* **85**, jun, pp. 430–437. viii, 9, 11, 12, 38

[2] Zhang, W., Yu, T., Fan, J., Sun, W., and Cao, Z., 2016. "Droplet impact behavior on heated micro-patterned surfaces." *Journal of Applied Physics,* **119**(11), mar, p. 114901. viii, 12, 13, 64, 65

[3] Clavijo, C. E., Crockett, J., and Maynes, D., 2017. "Hydrodynamics of droplet impingement on hot surfaces of varying wettability." *International Journal of Heat and Mass Transfer,* **108**, may, pp. 1714–1726. viii, 7, 9, 13, 15, 16, 17, 38

[4] Miller, D., 2017. "A comparison between self-cleaning properties via rolling droplets and condensation on superhydrophobic surfaces." mathesis, Brigham Young University, Dec. 2, 35

[5] Twain, M., 1872. *Roughing It*. American Publishing Company. 2

[6] Zheng, Q., and L, C., 2014. "Size effects of surface roughness to superhydrophobicity." *Procedia IUTAM,* **10**, pp. 462–475. 5

[7] Rohsenow, W. M., 1971. "Boiling." *Annual Review of Fluid Mechanics,* **3**(1), jan, pp. 211–236. 5

[8] Searle, M., Emerson, P., Crockett, J., and Maynes, D., 2018. "Influence of microstructure geometry on pool boiling at superhydrophobic surfaces." *International Journal of Heat and Mass Transfer,* **127**, dec, pp. 772–783. 5, 38, 39, 64, 69

[9] Rein, M., 1993. "Phenomena of liquid drop impact on solid and liquid surfaces." *Fluid Dynamics Research,* **12**(2), aug, pp. 61–93. 7

[10] Yarin, A., 2006. "DROP IMPACT DYNAMICS: Splashing, spreading, receding, bouncing…." *Annual Review of Fluid Mechanics,* **38**(1), jan, pp. 159–192. 7

[11] Rioboo, R., Tropea, C., and Marengo, M., 2001. "OUTCOMES FROM a DROP IMPACT ON SOLID SURFACES." *Atomization and Sprays,* **11**(2), p. 12. 7, 9

[12] Eggers, J., Fontelos, M. A., Josserand, C., and Zaleski, S., 2010. "Drop dynamics after impact on a solid wall: Theory and simulations." *Physics of Fluids,* **22**(6), jun, p. 062101. 7

[13] Moita, A., and Moreira, A., 2007. "Drop impacts onto cold and heated rigid surfaces: Morphological comparisons, disintegration limits and secondary atomization." *International Journal of Heat and Fluid Flow,* **28**(4), aug, pp. 735–752. 7, 9, 15

[14] Cossali, G., Marengo, M., and Santini, M., 2008. "Thermally induced secondary drop atomisation by single drop impact onto heated surfaces." *International Journal of Heat and Fluid Flow,* **29**(1), feb, pp. 167–177. 7, 9, 15, 34

[15] Roisman, I. V., Breitenbach, J., and Tropea, C., 2018. "Thermal atomisation of a liquid drop after impact onto a hot substrate." *Journal of Fluid Mechanics,* **842**, mar, pp. 87–101. 7, 9, 13, 38

[16] Li, X., Ma, X., and Lan, Z., 2009. "Behavioral patterns of drop impingement onto rigid substrates with a wide range of wettability and different surface temperatures." *AIChE Journal,* **55**(8), aug, pp. 1983–1992. 7, 9, 14

[17] Bernardin, J. D., Stebbins, C. J., and Mudawar, I., 1997. "Mapping of impact and heat transfer regimes of water drops impinging on a polished surface." *International Journal of Heat and Mass Transfer,* **40**(2), jan, pp. 247–267. 9, 38

[18] Bertola, V., 2009. "An experimental study of bouncing leidenfrost drops: Comparison between newtonian and viscoelastic liquids." *International Journal of Heat and Mass Transfer,* **52**(7-8), mar, pp. 1786–1793. 9, 10, 38

[19] Breitenbach, J., Roisman, I. V., and Tropea, C., 2017. "Drop collision with a hot, dry solid substrate: Heat transfer during nucleate boiling." *Physical Review Fluids,* **2**(7), jul. 9, 38, 55

[20] Clavijo, C., Stevens, K., Crockett, J., and Maynes, D., 2018. "Thermally induced atomization during droplet impingement on superheated hydrophobic and superhydrophobic surfaces." *International Journal of Heat and Mass Transfer,* **126**, nov, pp. 1357–1366. 9, 17, 18, 38, 40, 42, 64, 65, 69, 79

[21] Sajadi, S. M., Irajizad, P., Kashyap, V., Farokhnia, N., and Ghasemi, H., 2017. "Surfaces for high heat dissipation with no leidenfrost limit." *Applied Physics Letters,* **111**(2), jul, p. 021605. 10

[22] Jerng, D. W., and Kim, D. E., 2018. "Dynamic leidenfrost temperature on micro-textured surfaces: Acoustic wave absorption into thin vapor layer." *Applied Physics Letters,* **112**(5), jan, p. 053902. 10

[23] Bernardin, J. D., and Mudawar, I., 2004. "A leidenfrost point model for impinging droplets and sprays." *Journal of Heat Transfer,* **126**(2), p. 272. 10

[24] Burton, J. C., Sharpe, A. L., van der Veen, R. C. A., Franco, A., and Nagel, S. R., 2012. "Geometry of the vapor layer under a leidenfrost drop." *Physical Review Letters,* **109**(7), aug. 10

[25] Wang, Z., Xiong, J., Yao, W., Qu, W., and Yang, Y., 2019. "Experimental investigation on the leidenfrost phenomenon of droplet impact on heated silicon carbide surfaces." *International Journal of Heat and Mass Transfer,* **128**, jan, pp. 1206–1217. 10

[26] Tran, T., Staat, H. J. J., Prosperetti, A., Sun, C., and Lohse, D., 2012. "Drop impact on superheated surfaces." *Physical Review Letters,* **108**(3), jan. 12, 17, 39

[27] Tran, T., Staat, H. J. J., Susarrey-Arce, A., Foertsch, T. C., van Houselt, A., Gardeniers, H. J. G. E., Prosperetti, A., Lohse, D., and Sun, C., 2013. "Droplet impact on superheated micro-structured surfaces." *Soft Matter,* **9**(12), p. 3272. 13, 14, 17, 75

[28] Antonini, C., Amirfazli, A., and Marengo, M., 2012. "Drop impact and wettability: From hydrophilic to superhydrophobic surfaces." *Physics of Fluids,* **24**(10), oct, p. 102104. 13

[29] Park, J. Y., Min, C.-K., Granick, S., and Cahill, D. G., 2012. "Residence time and heat transfer when water droplets hit a scalding surface." *Journal of Heat Transfer,* **134**(10), p. 101503. 14

[30] Deng, T., Varanasi, K. K., Hsu, M., Bhate, N., Keimel, C., Stein, J., and Blohm, M., 2009. "Nonwetting of impinging droplets on textured surfaces." *Applied Physics Letters,* **94**(13), mar, p. 133109. 14, 39, 75

[31] Bowden, F. P., and Field, J. E., 1964. "The brittle fracture of solids by liquid impact, by solid impact, and by shock." *Proceedings of the Royal Society of London. Series A. Mathematical and Physical Sciences,* **282**(1390), nov, pp. 331–352. 14

[32] Field, J., 1999. "ELSI conference: invited lecture." *Wear,* **233-235**, dec, pp. 1–12. 14, 39

[33] Pittoni, P. G., Lin, Y.-C., and Lin, S.-Y., 2014. "The impalement of water drops impinging onto hydrophobic/superhydrophobic graphite surfaces: the role of dynamic pressure, hammer pressure and liquid penetration time." *Applied Surface Science,* **301**, may, pp. 515–524. 14, 39, 47, 51, 60, 64, 65, 75, 76, 80

[34] Clavijo, C. E., Crockett, J., and Maynes, D., 2016. "Wenzel to cassie transition during droplet impingement on a superhydrophobic surface." *Physical Review Fluids,* **1**(7), Nov. 15, 39, 40, 51, 64, 76

[35] Moita, A. S., and Moreira, A. L. N., 2011. "Scaling the effects of surface topography in the secondary atomization resulting from droplet/wall interactions." *Experiments in Fluids,* **52**(3), may, pp. 679–695. 15

[36] Castanet, G., Dunand, P., Caballina, O., and Lemoine, F., 2013. "High-speed shadow imagery to characterize the size and velocity of the secondary droplets produced by drop impacts onto a heated surface." *Experiments in Fluids,* **54**(3), mar. 15, 34

[37] Bertola, V., and Sefiane, K., 2005. "Controlling secondary atomization during drop impact on hot surfaces by polymer additives." *Physics of Fluids,* **17**(10), p. 108104. 17

[38] KIM, H., TRUONG, B., BUONGIORNO, J., and HU, L.-W., 2012. "Effects of micro/nano-scale surface characteristics on the leidenfrost point temperature of water." *Journal of Thermal Science and Technology,* **7**(3), pp. 453–462. 17, 50, 75

[39] Guo, C., Maynes, D., Crockett, J., and Zhao, D., 2019. "Heat transfer to bouncing droplets on superhydrophobic surfaces." *International Journal of Heat and Mass Transfer,* **137**, jul, pp. 857–867. 23, 55, 56, 64

[40] Hays, R., Maynes, D., and Crockett, J., 2016. "Thermal transport to droplets on heated superhydrophobic substrates." *International Journal of Heat and Mass Transfer,* **98**, jul, pp. 70–80. 38, 39, 64

[41] Liu, G., Fu, L., Rode, A. V., and Craig, V. S. J., 2011. "Water droplet motion control on superhydrophobic surfaces: Exploiting the wenzel-to-cassie transition." *Langmuir,* **27**(6), mar, pp. 2595–2600.

[42] Ishino, C., Reyssat, M., Reyssat, E., Okumura, K., and Quéré, D., 2007. "Wicking within forests of micropillars." *Europhysics Letters (EPL),* **79**(5), aug, p. 56005. 40

[43] Roisman, I. V., Horvat, K., and Tropea, C., 2006. "Spray impact: Rim transverse instability initiating fingering and splash, and description of a secondary spray." *Physics of Fluids,* **18**(10), oct, p. 102104.

[44] Tamayol, A., and Bahrami, M., 2009. "Analytical determination of viscous permeability of fibrous porous media." *International Journal of Heat and Mass Transfer,* **52**(9-10), apr, pp. 2407–2414. 53

[45] Wildeman, S., Visser, C. W., Sun, C., and Lohse, D., 2016. "On the spreading of impacting drops." *Journal of Fluid Mechanics,* **805**, sep, pp. 636–655. 55

APPENDIX A. FABRICATION OF SUPERHYDROPHOBIC SURFACES

The SH surfaces used in the current work are fabricated by using photolithography and etching processes to create surface microstructures. The surface is then coated with Teflon to provide hydrophobicity. Figure A.1 shows SEM images of the three types of structures used. This appendix provides a detailed description of the fabrication process along with relevant parameters and information pertaining to the chemicals and equipment used.

A.1 Fabrication Process

A silicon wafer, 0.5 mm thick and 100 mm in diameter, is placed on a spinner and cleaned with acetone and isopropyl alcohol. It is then baked in a dry oven at 150 °C for about 10 minutes. The wafer is spin-coated with photoresist and baked on a hot plate for one minute. Two types of photoresist are used: AZ 2020 (negative photoresist) and AZ 3330 (positive photoresist). When AZ 3330 is used, the wafer is first coated with HMDS to help with adhesion. Table A.1 provides specifications for the spin and bake processes for each chemical. The same developer chemical, AZ 300 MIF, is used for both photoresists. The wafer is then exposed under a photomask of the desired pattern using a Karl Suss Aligner. Exposure time is dependent on the strength of the

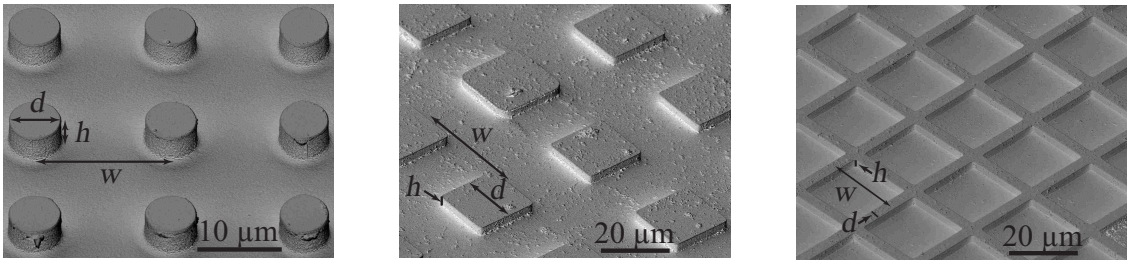

Figure A.1: SEM images of the three microstructure types used in the present work: (a) circular posts with $w = 16$ μm, $d = 5$ μm, $h = 4$ μm, (b) square posts with $w = 40$ μm, $d = 20$ μm, $h = 4$ μm, and (c) square holes with $w = 24$ μm, $d = 4$ μm, $h = 4$ μm.

Table A.1: Lithography chemicals and specifications used for the fabrication of SH surfaces.

Chemical	Type	Spin Speed (rpm)	Spin Time (s)	Bake Temperature (°C)	Bake Time (s)
AZ 3330	Positive	5500	60	90C	60
HMDS	Adhesion	2000	5	-	-
AZ 2020	Negative	2750	60	110	60

exposure, which can be measured using a light detector. The exposure energy of the photoresist can be found on a datasheet and used with the detector readout to calculate exposure time. Generally, exposure times between 10 and 20 seconds were used here. Note that the entire lithography process must be done in a filtered-light environment to avoid premature UV exposure.

For the circular post structures shown in Figure 2.1a, AZ 2020 is used with a photomask that exposes a pattern of circles onto the wafer. The wafer is then developed by submerging in AZ 300 MIF and lightly swirling the chemical until photoresist can be seen only in the exposed area. In this case, the pattern of circles remains. For the square holes shown in Figure 2.1c, AZ 2020 is used with a mask of ribs. The wafer is exposed twice with the mask rotated 90 ° between exposures. This leaves a crossed-rib photoresist pattern that remains after development. For the square posts show in Figure 2.1b, a different rib mask is used in the crossed-rib method described above, but AZ 3330 photoresist is used, so the ribs are dissolved during development, leaving a pattern of squares. After development, the wafer is rinsed in deionized (DI) water and baked again on a hotplate, following the same specifications as the pre-exposure bake.

Etching is performed using an STS plasma etcher. The number of etching cycles performed to reach the desired microstructure height varies greatly depending on both micropattern dimensions and machine upkeep. To start, a relatively low number of cycles are performed, depending on the desired final etching depth. The surface is then taken to a Zeta 20 3D optical profilometer, which scans the surface and provides micropattern measurements. The remaining required number of cycles to reach the desired etching depth may then be calculated. The surfaces fabricated for this work are etched to between 4 μm and 12 μm.

After etching, the remaining photoresist is removed from the surface using Nanostrip, a sulfuric acid compound commonly used to dissolve organic materials in microfabrication processes. The acid is highly corrosive, and extra precaution is used to prevent contact with skin. The wafer is

submerged in Nanostrip and placed on a hotplate at 90 °C for three to four hours. The acid is then allowed to cool to room temperature before being disposed of. The wafer is rinsed in DI water and subjected to an oxygen burn using a Technics Planar Etch 2 plasma etching machine. The oxygen burn is to remove any organic material that may remain on the surface. The wafer is then baked in a dry oven at 150 °C for about 10 minutes to dehydrate.

A chromium layer, nominally 100 nm thick, is deposited on the surface using a Denton Vacuum E-beam Evaporator. A solution of 0.2% Teflon in Fluorinert FC-40 liquid is applied to the wafer and spin-coated. The wafer is then placed on a hotplate and ramped up to 330 °C over the course of about 10 minutes. It is baked at this temperature for 20 minutes and then allowed to cool back down to room temperature. Through the baking process, the FC-40 is evaporated and the Teflon is applied uniformly to the surface. Baking must be done in a highly ventilated area, ideally under a fume hood, because FC-40 can cause health problems when inhaled. The thickness of the Teflon is nominally 200 nm. Microstructure dimensions of the completed surface are measured using the optical profilometer with uncertainty of about 1%. Smooth hydrophobic (SmH) surfaces are fabricated following the same process without lithography and etching.

APPENDIX B. UNCERTAINTY ANALYSIS

This appendix describes the details of the uncertainty analysis, which was performed on all important experimental parameters. Values of Weber number and surface temperature that are reported throughout this thesis vary slightly from measured values. This was done for convenience, and the measured values are reported here. First, 95% confidence intervals are obtained to show repeatability of the measurements. The overall uncertainty of each parameter is then discussed. Note that atomization intensity, as calculated by the image processing technique, is a relative value and is dependent on parameters such as background lighting for which accurate uncertainty cannot be predicted. Thus, for atomization intensity, 95% confidence intervals are included but overall uncertainty is not.

B.1 Measured Values and Confidence Intervals

Confidence intervals in this section are calculated as:

$$\overline{X} \pm t_{\nu,95} \frac{S}{\sqrt{n}} \tag{B.1}$$

where $\overline{X}$ is the sample mean, S is the sample standard deviation, n is the number of samples, and $t_{\nu,95}$ is the two-tailed Student's t-distribution value for 95% confidence; $\nu = n - 1$ is degrees of freedom.

For the atomization intensity measurement in a given impingement scenario, 15 to 30 trials are analyzed using the image processing technique. The final value of atomization intensity in a given scenario is taken to be the average of these trials. As discussed in Chapter 2, atomization intensity is calculated as the sum of pixel intensities in the "final frame" (see Figure 2.6). For the various studies considered in this thesis, atomization intensity is normalized. However, in order

to give a complete summary of the relative atomization intensity on each test surface considered, atomization intensity in this section is presented as the raw calculated value.

Six surface microstructure shapes are considered for the research in this thesis (see Figure 2.1): smooth (no microstructure), 8 μm pitch circular posts, 12 μm pitch circular posts, 16 μm pitch circular posts, 40 μm pitch square posts, and 24 μm pitch square holes. Table B.1 gives 95% confidence intervals for the atomization intensity found for each of these microstructures. In each case, microstructure height is 4 μm, Weber number is 85, and surface temperature is chosen to maximize atomization intensity. Surface temperature is 220 °C for the smooth, 300 °C for the 8 μm pitch posts, 180 °C for the 12 μm and 16 μm pitch posts, 160 °C for the square posts, and 140 °C for the square holes.

Spatial resolution, R_s, is measured in μm/pixel for the high-speed images used in this work; this allows droplet diameter and impact velocity for each scenario to be calculated. A sample size of $n = 148$ yields an average value of $R_s = 11.94 \pm 0.01$ μm/pixel. For droplet diameter, D_0, 66 samples were used. This results in an average value of $D_0 = 2.26 \pm 0.01$ mm.

Confidence intervals for droplet impact velocity, V_0, vary slightly depending on velocity magnitude. Table B.2 displays the impact velocities used in this work along with their 95% confidence intervals and the number of samples used to obtain each interval. Confidence for impact velocity is within $\pm 1\%$ for all velocities measured. Weber number is calculated using measured droplet diameter and impact velocity. Table B.3 displays the value reported in the thesis, mea-

Table B.1: 95% confidence interval for atomization intensity. For each microstructure shape, height is 4 μm, Weber number is 85, and surface temperature is chosen to maximize atomization intensity: 220 °C for the smooth, 300 °C for the 8 μm pitch posts, 180 °C for the 12 μm and 16 μm pitch posts, 160 °C for the square posts, and 140 °C for the square holes.

Microstructure	Atomization Intensity	95% Confidence	95% confidence (%)
Smooth	28,750	± 1,079	± 3.8%
8 μm Pitch Circular Post	37,710	± 1,594	± 4.2%
12 μm Pitch Circular Post	511	± 212	± 41.4%
16 μm Pitch Pircular Post	523	± 175	± 33.4%
Square Post	157	± 31	± 19.9%
Square Hole	240	± 24	± 9.9%

Table B.2: Droplet impact velocities used in this work, corresponding 95% confidence intervals, and the number of samples used to obtain each interval.

Measured Velocity (m/s)	95% Confidence (m/s)	Number of Samples
0.84	$\pm$ 0.01	7
1.14	$\pm$ 0.005	13
1.68	$\pm$ 0.005	27
2.17	$\pm$ 0.01	8
2.52	$\pm$ 0.02	4
2.76	$\pm$ 0.01	8

Table B.3: Reported and measured Weber numbers used in this work, corresponding 95% confidence intervals, and the number of samples used to obtain each interval.

Reported Weber Number	Measured Weber Number	95% Confidence	Number of Samples
20	21.9	$\pm$ 0.5	7
40	40.0	$\pm$ 0.3	13
85	87.4	$\pm$ 0.5	27
150	146.3	$\pm$ 1.7	8
200	196.8	$\pm$ 4.5	4
240	237.8	$\pm$ 4.3	8

sured value, confidence interval, and number of samples for each Weber number used in this work. Confidence intervals range from $\pm$0.5% to $\pm$2.3%.

Surface temperature is controlled by a temperature controller with a thermocouple that is placed in the aluminum heating block. Due to resistance between the thermocouple and test surface, the thermocouple readout does not exactly reflect the actual surface temperature. A calibration was performed between these two temperatures using IR measurements on a matte black test surface. Throughout this thesis, the thermocouple readout is used as the reported value for surface temperature. Table B.4 displays the reported value, IR measured value, and a confidence interval for the range of surface temperatures used in this work. Between 10 and 15 samples were used at each temperature, and confidence is always within $\pm$1%.

Table B.4: Reported and measured surface temperatures used in this work and corresponding 95% confidence intervals. Between 10 and 15 samples were taken at each temperature.

Reported Temperature (°C)	Measured Temperature (°C)	95% Confidence
120	118.4	± 0.6
140	137.9	± 0.5
160	157.8	± 0.8
180	177.1	± 1.0
200	197.1	± 1.2
220	216.2	± 1.3
240	235.7	± 1.6
260	256.8	± 2.1
280	277.0	± 2.4
300	296.8	± 2.7
320	316.6	± 2.7

B.2 Uncertainty Analysis

An uncertainty analysis is performed for all relevant measured parameters: spatial resolution, droplet diameter, impact velocity, Weber number, and surface temperature. Many measurements in this work are performed using image processing (such as droplet diameter and impact velocity), as discussed in Section 2.3.2, and are dependent on experimental conditions including background lighting and lens focus. Since measurements are highly repeatable, human error associated with these experimental conditions is neglected in the overall uncertainty analyses. The edge of the droplet in high-speed images is not precisely defined, but fades somewhat into the background. For this reason, thresholding (which is done using the MATLAB function `im2bw(IM,T)`) becomes important for these measurements. In this work it is assumed that thresholding allows the location of the droplet edge to be determined with accuracy of ± 1 pixel.

In the case that multiple uncertainties must be accounted for, such as with errors associated with multiple instruments or random noise, total uncertainty, u_{tot}, can be obtained by:

$$u_{tot} = \sqrt{u_1^2 + u_2^2 + ... + u_n^2} \tag{B.2}$$

where u_i represents uncertainties upon which u_{tot} is dependent. Additionally, many parameters in this work involve calculations using previously obtained measurements (e.g. Weber number is

calculated from droplet diameter and impact velocity). Propagation of uncertainty is performed in these cases as follows:

$$u_f = \sqrt{\left(u_{y_1}\frac{\partial f}{\partial y_1}\right)^2 + \left(u_{y_2}\frac{\partial f}{\partial y_2}\right)^2 + ... + \left(u_{y_n}\frac{\partial f}{\partial y_n}\right)^2} \tag{B.3}$$

Here, u_f is the uncertainty of some parameter, f; u_{y_i} is uncertainty of the variable y_i, upon which f is dependent; and $\frac{\partial f}{\partial y_i}$ is the derivative of f with respect to y_i.

B.2.1 Spatial Resolution

Spatial resolution of the high-speed images is found using the equation $R_s = x/p$, where x is the physical distance between two points and p is the number of pixels between the same points. Image processing is used on an image (with a ruler in the frame for reference) to identify the number of pixels between the chosen points. The distance x is based on the ruler, which has resolution of 1 mm. Error in this distance is neglected. The number of pixels, p, is estimated to have error of $u_p = \pm$ 2 pixels to account for uncertainty in locating the edge of the ruler ticks at each selected point (similar to locating the droplet edge, as discussed above). Spatial resolution is then calculated from Equation B.3 as:

$$u_{R_s} = \sqrt{\left(u_p\frac{\partial R_s}{\partial p}\right)^2} \tag{B.4}$$

where:

$$\frac{\partial R_s}{\partial p} = \frac{-x}{p^2} \tag{B.5}$$

Nominal values for x and p are 11 mm and 925 pixels, respectively. The uncertainty, then, is $\pm$0.03 μm/pixel, or $\pm$0.3%.

B.2.2 Droplet Diameter

Droplet diameter is measured using image processing as discussed in Section 2.3.2. Diameter is calculated as $D_0 = R_s\sqrt{4A_p/\pi}$, where A_p is area of the droplet in pixels. Droplet pixel area is found to be nominally 28,600 square pixels. Area uncertainty is dependent on thresholding

(which has an accuracy of ± 1 pixel) around the entire circumference of the droplet, and comes out to be $u_{A_p} = \pm 600$ pix^2. Diameter uncertainty is calculated from Equation B.3 as:

$$u_{D_0} = \sqrt{\left(u_{R_s}\frac{\partial D_0}{\partial R_s}\right)^2 + \left(u_{A_p}\frac{\partial D_0}{\partial A_p}\right)^2} \tag{B.6}$$

where:

$$\frac{\partial D_0}{\partial R_s} = \sqrt{\frac{4A_p}{\pi}} \tag{B.7}$$

$$\frac{\partial D_0}{\partial A_p} = R_s\sqrt{\frac{1}{\pi A_p}} \tag{B.8}$$

Error in droplet diameter comes out to be ± 0.02 mm or $\pm 1.1\%$.

B.2.3 Droplet Impact Velocity

Droplet impact velocities are calculated as outlined in Section 2.3.2 using the equation $V_0 = R_s\Delta y/\Delta t$, where Δy is vertical distance in pixels between two droplet locations (measured at the top of the droplet) and Δt is the timestep between frames. Because velocity is concerned only with distance between points, the error associated with finding the droplet edge can be neglected as long as the threshold remains constant. However, the image resolution is one pixel, yielding possible error for each vertical location of ± 0.5 pixels, and total error of $u_{\Delta y} = \pm 1$ pixel. Error in the time step is neglected, and the uncertainty of velocity is (from Equation B.3):

$$u_{V_0} = \sqrt{\left(u_{R_s}\frac{\partial V_0}{\partial R_s}\right)^2 + \left(u_{\Delta y}\frac{\partial V_0}{\partial \Delta y}\right)^2} \tag{B.9}$$

where:

$$\frac{\partial V_0}{\partial R_s} = \frac{\Delta y}{\Delta t} \tag{B.10}$$

$$\frac{\partial V_0}{\partial \Delta y} = \frac{R_s}{\Delta t} \tag{B.11}$$

The value of Δy varies with velocity magnitude and ranges from 23 pixels to 76 pixels. Equation B.9 is solved for each impact velocity considered, and results are displayed in Table B.5

Table B.5: Droplet impact velocities used in this work with error values in m/s and percentage of velocity magnitude.

Measured Velocity (m/s)	Uncertainty (m/s)	Uncertainty (%)
0.84	± 0.036	± 4.3
1.14	± 0.036	± 3.2
1.68	± 0.036	± 2.2
2.17	± 0.036	± 1.7
2.52	± 0.037	± 1.4
2.76	± 0.037	± 1.3

B.2.4 Weber Number

Weber number is calculated as $We = \rho V_0^2 D_0/\sigma$, where $\rho = 999$ kg/m^3 and $\sigma = 0.0728$ N/m are standard values for density and surface tension, respectively, of water at room temperature. The error associated with these values is assumed zero. Uncertainty and values for V_0 and D_0 are defined in the previous sections, and Weber number uncertainty is calculated from Equation B.3 as:

$$u_{We} = \sqrt{\left(u_{V_0}\frac{\partial We}{\partial V_0}\right)^2 + \left(u_{D_0}\frac{\partial We}{\partial D_0}\right)^2} \tag{B.12}$$

where:

$$\frac{\partial We}{\partial V_0} = \frac{2\rho V_0 D_0}{\sigma} \tag{B.13}$$

$$\frac{\partial We}{\partial D_0} = \frac{\rho V_0^2}{\sigma} \tag{B.14}$$

This equation is evaluated at each Weber number considered and results are shown in Table B.6.

Table B.6: Weber number values and uncertainties used in this work.

Measured Weber Number	Uncertainty	Uncertainty (%)
21.9	± 1.9	± 8.7
40.0	± 2.6	± 6.5
87.4	± 3.9	± 4.4
146.3	± 5.1	± 3.5
196.8	± 6.1	± 3.1
237.8	± 6.7	± 2.8

B.2.5 Surface Temperature

Surface temperature is controlled by a temperature controller and thermocouple with reported uncertainties of $u_{ctrl} = \pm 0.2\%$ and $u_{TC} = \pm 2.2$ °C, respectively. The thermocouple is placed in the aluminum heating block 0.5 cm below the test surface and about 5.5 cm from its center. Due to resistance in the block and at the interface between the block and test surface, a discrepancy exists between the thermocouple readout and the actual surface temperature. A calibration was performed between these two surfaces using a FLIR IR camera with reported uncertainty of $u_{FLIR} = \pm 2$ °C. Resolution of the measurements is one degree, and zero-order uncertainty is estimated to be $u_0 = \pm 1$ °C.

A test surface was painted matte black so as to have an emissivity of 0.97, and 10 to 15 IR measurements were recorded at each temperature for a range of surface temperatures. Figure B.1 shows the calibration data and a linear curve fit. Error associated with the calibration is calculated as follows:

$$u_{calib} = \pm t_{\nu,95} \sqrt{\frac{1}{\nu} \sum_{i=1}^{N} (y_i - y_{ci})^2} \tag{B.15}$$

where $t_{\nu,95}$ is the two-tailed Student's t-distribution for 95% confidence and ν degrees of freedom. In this case, $\nu = N - (m+1)$ where N is number of calibration points and m is the order of the curve fit. The variable y_i is the data value (IR measurement) and y_{ci} is the corresponding curve fit value. Additionally, random noise error is calculated for each temperature as $u_{noise} = \pm t_{\nu,95} S$. Here, ν is simply one less than the sample size, and S is the sample standard deviation.

Total uncertainty for each measured surface temperature is calculated from Equation B.2 as:

$$u_{T_s} = \sqrt{u_{ctrl}^2 + u_{TC}^2 + u_{FLIR}^2 + u_0^2 + u_{calib}^2 + u_{noise}^2} \tag{B.16}$$

It is important to note that the total uncertainties for each temperature are associated with the IR measurement. The uncertainties of the temperature controller and thermocouple are included in the calculation because these determine how accurately the temperature is maintained (i.e. temperature fluctuations with time). The calibration uncertainty determines how accurately the actual temperature measurement can be determined from the thermocouple readout. The other three uncertainties are directly related to the IR measurements. Results are presented in Table B.7.

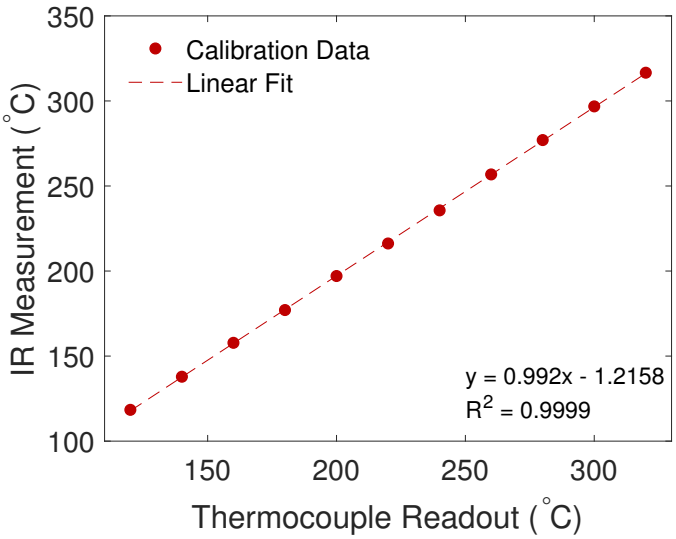

Figure B.1: Calibration data for surface temperature.

Table B.7: Surface temperature values and uncertainties (in °C and percentage of temperature magnitude) used in this work.

Measured Temperature (°C)	Uncertainty (°C)	Uncertainty (%)
118.4	± 4.2	± 3.5
137.9	± 4.0	± 2.9
157.8	± 4.7	± 3.0
177.1	± 5.1	± 2.9
197.1	± 5.7	± 2.9
216.2	± 6.2	± 2.9
235.7	± 7.1	± 3.0
256.8	± 7.6	± 2.9
277.0	± 8.2	± 3.0
296.8	± 9.2	± 3.1
316.6	± 9.2	± 2.9